First Measurement of the Electron Neutrino Charged Current Pion Production Cross Section on Carbon

AND

Optical Calibration Development for Hyper-Kamiokande

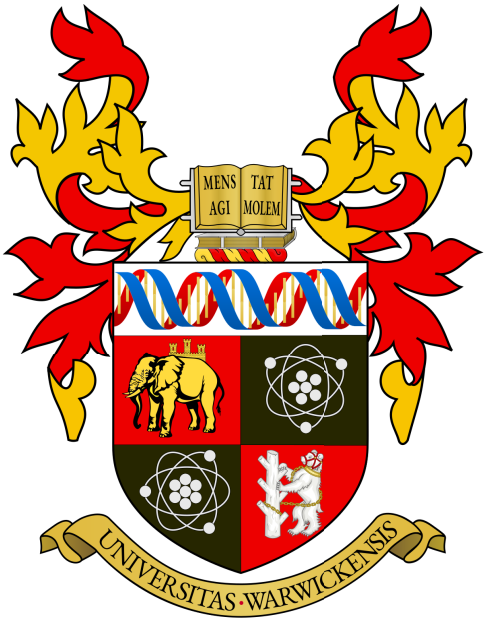

Nicholas A. Latham

University of Warwick
Department of Physics

Submitted to the University of Warwick in partial fulfilment of the requirements for admission to the degree of Doctor of Philosophy in Physics

March 2024

Contents

List of Figures i

List of Tables x

Acknowledgements xiii

Declaration xiv

Abstract xv

List of Acronyms xvi

Thesis Outline xvii

I Neutrino physics 1

1 Introduction to Neutrino Physics 3
1.1 Historical overview . . . 3
1.1.1 Postulation . . . 3
1.1.2 Fermi theory and first detection . . . 4
1.1.3 Anti-neutrinos and neutrino flavour . . . 5
1.1.4 The solar neutrino problem . . . 8
1.1.5 Atmospheric neutrinos . . . 9
1.2 Neutrino oscillations . . . 11
1.2.1 Predictions and early discoveries . . . 11
1.2.2 PMNS formalism . . . 13
1.2.3 Neutrino oscillations in matter . . . 15
1.2.4 Parameter measurements . . . 16
1.2.5 Towards a new precision era . . . 18
1.3 Other frontiers . . . 19
1.3.1 The nature of neutrino mass . . . 19
1.3.2 Supernova and relic neutrinos . . . 20
1.3.3 Sterile neutrinos . . . 20

2 Neutrino Interactions 22
2.1 The Standard Model . . . 22
2.2 A formalism of neutrino-nucleus interactions . . . 24
2.2.1 Nuclear models . . . 24
2.2.2 Cross section models . . . 25
2.2.3 Final state interactions . . . 28
2.3 Types of neutrino-nucleus interactions . . . 28
2.3.1 Charged current quasi elastic scattering . . . 28
2.3.2 Resonant pion production . . . 31
2.3.3 Coherent pion production . . . 32
2.3.4 Deep inelastic scattering . . . 32
2.3.5 Other interactions . . . 34
2.4 Status of neutrino cross section measurements . . . 34

II Measurement of the ν_eCCπ^+ Cross Section on Carbon with T2K 37

3 The T2K Experiment 39
3.1 Physics goals and accomplishments . . . 40
3.2 Neutrino beamline . . . 42
3.3 Near detector complex . . . 43
3.3.1 ND280 . . . 44
3.3.2 INGRID . . . 48
3.3.3 WAGASCI-BabyMIND . . . 49
3.3.4 ND280 upgrade . . . 50
3.4 Super-Kamiokande . . . 51
3.5 T2K phase-II . . . 54

4 Analysis Strategy 55
4.1 Introduction . . . 55
4.2 Definitions . . . 57
4.2.1 Cross section measurement . . . 57
4.2.2 Signal definition . . . 58
4.2.3 Background definitions . . . 59
4.2.4 Samples . . . 60
4.3 Truth studies . . . 61
4.3.1 Sensitivity studies . . . 61
4.3.2 Pion kinematics reconstruction from Michel electrons . . . 62

5 Event Selection 65
5.1 Selection cuts . . . 66
5.1.1 Event quality and track multiplicity . . . 66
5.1.2 Particle identification . . . 67
5.1.3 Upstream photon vetoes . . . 70

5.1.4 TPC sample cuts . . . 70
5.1.5 FGD sample cuts . . . 73
5.1.6 TPC control sample cuts . . . 75
5.1.7 FGD control sample cuts . . . 76
5.2 Selection outputs . . . 76
5.2.1 Signal samples . . . 76
5.2.2 Control samples . . . 82
5.3 Selection performance . . . 84
5.3.1 Selection cuts . . . 84
5.3.2 Track reconstruction . . . 86
5.3.3 Differential efficiencies . . . 88
5.3.4 Control sample validation . . . 89

6 Systematic Uncertainties 92
6.1 Detector systematic uncertainties . . . 92
6.1.1 Standard ND280 detector systematic uncertainties . . . 92
6.1.2 Custom ND280 detector systematic uncertainties . . . 95
6.1.3 Overall uncertainties . . . 99
6.2 Flux systematic uncertainties . . . 101
6.3 Cross section model systematic uncertainties . . . 103

7 Cross Section Extraction 106
7.1 Fitting and cross section extraction . . . 106
7.1.1 Fit method . . . 106
7.1.2 Cross section extraction . . . 109
7.2 Binning . . . 110
7.2.1 Binning optimisation . . . 110
7.2.2 Projections . . . 113
7.3 Fit validation . . . 113
7.3.1 Fit metrics . . . 114
7.3.2 Pseudo data studies . . . 114

8 Results 119

III Optical Calibration Development at Hyper-Kamiokande 124

9 The Hyper-Kamiokande Experiment 126
9.1 Experimental set-up . . . 126
9.1.1 Far detector . . . 127
9.1.2 Intermediate water Cherenkov detector . . . 128
9.2 Physics goals . . . 128
9.2.1 Neutrino oscillation measurements . . . 128
9.2.2 Astrophysical neutrino studies . . . 129

9.2.3 Nucleon decay searches . . . 129

10 Collimators for Optical Calibration 130
10.1 The light-injection system . . . 130
10.2 Design . . . 132
10.2.1 Physical and optical requirements . . . 132
10.2.2 Components and assembly . . . 133
10.3 Test-stand . . . 135
10.3.1 Equipment . . . 135
10.3.2 Scanning . . . 136
10.4 Analysis . . . 138
10.5 Optical performance . . . 139
10.5.1 Expansion and profile . . . 139
10.5.2 Alignment tolerances . . . 140
10.5.3 Beam divergences . . . 141
10.5.4 Wavelength variance . . . 142
10.5.5 Systematic studies . . . 143
10.5.6 Far-field measurements . . . 144
10.6 Conclusions and next steps . . . 146

IV Conclusion 147

Appendices 149

A T2K Analysis Appendices 150
A.1 Software and data . . . 150
A.2 Analysis binning . . . 151
A.2.1 True sample binning . . . 151
A.2.2 Reconstructed sample binning . . . 152
A.2.3 Flux energy binning . . . 154

B Hyper-K Analysis Appendices 155
B.1 Doublet collimator . . . 155

Bibliography 155

List of Figures

1 Joint measurements of the hadron production cross section around the Z^0 resonance from the ALEPH [14], DELPHI [15], L3 [16] and OPAL [17] experiments. The solid lines indicate the Standard Model predictions of the cross section assuming two, three and four weakly-coupling neutrinos of negligible mass. This plot was taken from Ref. [18]. 7

2 The predicted solar neutrino flux as a function of neutrino energy using the standard solar model [19] with the main processes annotated. This plot was taken from Ref. [20]. 9

3 The measured electron and muon neutrino event rate dependence on the distance-energy ratio (L/E_ν) using data from the Super-Kamiokande experiment. The dotted lines represent the event rate predictions assuming the occurrence of two-flavour neutrino oscillations. This plot was taken from Ref. [29]. 11

4 Neutrino oscillation results from the SNO experiment [30]. This shows the ^{8}B ν_e and $\nu_{\mu,\tau}$ fluxes, ϕ_e and $\phi_{\mu\tau}$, indicating the sources and predictions from the standard solar model [19]. These are broken down into measurements of charged current (CC), neutral current (NC) and elastic scattering (ES) processes. This plot is taken from Ref. [32]. 12

5 A graphic depicting all particles and interactions predicted by the Standard Model, alongside various properties including mass, electric charge, colour charge and spin. This custom diagram was inspired from a design in Ref. [58]. 23

6 A Feynman diagram depicting generic neutrino scattering off a nucleon $(\nu\text{-}N)$. The bracketed terms indicate the four-momentum of each particle. 26

7 Feynman diagrams of the charged current quasielastic scattering of a neutrino off a neutron (left) and an anti-neutrino off a proton (right). 29

8 A Feynman diagram showing the inelastic scattering of a neutrino off a neutron with an intermediate $\Delta(1232)$ resonance state. 31

9 A Feynman diagram showing the coherent scattering of a neutrino off a nucleus. 32
10 A Feynman diagram showing the deep inelastic scattering of a neutrino off a nucleus, resulting in fragmentation which generates many final-state particles represented by X. 33
11 The predicted NEUT [59] neutrino-nucleus interaction cross sections as a function of energy for neutrinos (left) and anti-neutrinos (right) with the main interaction modes annotated. These plots are taken from Ref. [63] and the data entries represent many different measurements from a variety of experiments. . 34
12 Measurements of the differential ν_μCC and $\bar{\nu}_\mu$CC cross sections as a function of energy from a variety of experiments including T2K [43], MINOS [40] and MINERvA [78]. This plot is taken from Ref. [79]. 35
13 Measurements of the differential ν_eCC (left) and $\bar{\nu}_e$CC (right) cross sections as a function of electron momentum p and angle θ with comparisons to NEUT [59], GENIE [61] and NUWRO [87]. These plots are taken from Ref. [85]. . . . 36

14 A cross-sectional diagram of the Tōkai-to-Kamioka experiment. The green arrow represents the neutrino beam which is produced at J-PARC and travels 280 m westwards to the near detector complex, followed by the Super-Kamiokande far detector which is a further 295 km to the west. This is taken from Ref. [93]. 39
15 A measurement of the CP-violating phase, δ_{CP}, performed by the T2K experiment. This is presented as a two-dimensional confidence interval between δ_{CP} and the neutrino mixing angle parameters to 3σ, **a** $\sin^2\theta_{13}$ and **b** $\sin^2\theta_{23}$. The plot shows the limits with and without external constraints using data from reactor neutrino experiments. Plot **c** shows the one-dimensional confidence intervals and the best fit value of δ_{CP} is represented by the black line. This plot is taken from Ref. [46]. 41
16 A schematic of the neutrino beamline at J-PARC with the primary beamline, secondary beamline and sub-sections annotated. This figure was taken from Ref. [43]. 42
17 The neutrino flux as a function of energy, E_ν, in forward horn current mode (left) and reverse horn current mode (right) as measured at the off-axis near detector of T2K, ND280. The flux is distinguished by contributions from each neutrino flavour type. These plots are taken from Ref. [85]. 44

18 An exploded schematic of the off-axis near detector of the T2K experiment, ND280. The purple line indicates the approximate neutrino beam direction. This figure was taken and adapted from Ref. [43]. 45
19 A cross-sectional diagram of the neutral pion detector module in ND280. This diagram was taken from Ref. [96]. 46
20 Cut-away diagram of the time projection chambers in ND280. This figure was reproduced from Ref. [98]. 48
21 A graphic of the INGRID on-axis near detector. The orange circle indicates the beam centre with respect to the INGRID modules. This figure was taken and adapted from Ref. [100]. 49
22 A diagram showing the upgraded ND280 components overlayed onto the original ND280 schematic with the pi-zero detector removed. This was reproduced from Ref. [101]. 50
23 A diagram of the Super-Kamiokande experiment. This was taken from Ref. [102]. 52
24 An example of the electron-muon particle identity discriminator variable for electron neutrino-like and muon neutrino-like events as used in Super-Kamiokande. This plot is taken from Ref. [46]. 53

25 A distribution of the reconstructed neutrino energy assuming charged current Δ kinematics ($E^{\Delta}_{\mathrm{rec}}$) for the $1R_e+1$ d.e. sample in forward horn current dataset at Super-Kamiokande. This plot is taken from Ref. [45]. 56
26 The reconstructed lepton momentum distribution for the $1R_e+1$ d.e. sample in recent T2K-Super-Kamiokande joint fit studies. The blue and red error bars show the expected event rates and their uncertainties from the fit results from the beam and ND280 flux measurement task force in Ref. [103]. 56
27 Schematics of the ND280 detector showing examples of typical signal events that would pass into (a) the TPC sample or (b) the FGD sample. The dotted tracks represent the intermediate particles which form the decay chain to the Michel electron ($\pi^+ \to \mu^+ \to e^+$). The legend indicates the particle species corresponding to each example track. 60

28 Distributions of the true pion momentum, p_π, and true neutrino energy assuming charged current Δ kinematics, E^{Δ}_{rec}, for all $\nu_e\text{CC}\pi^+$ signal events without any selection cuts applied. The categories distinguish between pions which stay in FGD1 or pass from FGD1 into TPC2. The regions left of the black dashed lines indicate the phase spaces relevant to the Super-K far detector. These boundaries are $p_\pi < 0.156$ GeV$/c$ and $E^{\Delta}_{\text{rec}} < 1.25$ GeV. 61

29 Schematic of Michel electron (e^+) production from $\nu_e\text{CC}\pi^+$ events superimposed on a subsection of the ND280 geometry. The quantities d and θ are the distance and angle between the Michel electron vertex and the original $\nu_e\text{CC}\pi^+$ vertex respectively. The legend indicates the particle species corresponding to each track. The track lengths of the pion and muon are exaggerated to clearly indicate the origin of d and θ. 63

30 Two-dimensional histograms of the true separation distance between the neutrino vertex and Michel electron vertex d and the true pion momentum p^{true}_π (left), and of the true Michel electron angle $\theta^{\text{true}}_{\text{ME}}$ against the true pion angle θ^{true}_π (right). The z-axis measures the MC event rate per bin. 64

31 Measurements and fits of the mean ionisation as a function of particle momentum in the TPCs for electron, muon, pion and proton tracks starting in FGD1. This shows the trends for negatively charged tracks (left) and positively charged tracks (right). These plots were taken from Ref. [85]. 67

32 Distributions of the electron, pion and muon pull variables of leading tracks which enter the TPCs downstream of FGD1. The lower right distribution shows the muon pull for tracks which enter TPC3, while the other three show the pulls for tracks which only enter TPC2. The arrows indicate the events which pass the selection cut. 69

33 Distributions of the ECal $R_{\text{MIP/EM}}$ values of leading tracks with $p < 800$ MeV$/c$ (left), and the ECal EM energy of leading tracks which enter the ECal and have $p > 800$ MeV$/c$ (right). The arrows indicate the events which pass the selection cut. 69

34 Distributions of the pion pull of pion candidate tracks in the standard event categorisation (left) and the true pion candidate particle categorisation (right). The arrows indicate the accepted events. 71

35 Schematic of the ECal polar angle θ_z on the ND280 geometry. The main electron candidate track (pink) and a track with ECal activity (yellow) are indicated and the dashed black line is parallel with the z-axis of ND280. 71
36 Distributions of the cosine of the ECal polar angle θ_z for events with an electron candidate and an additional track with ECal activity. The arrows indicate events which are passed. 72
37 A distribution of the invariant mass, m_{inv}, of the leading and pion candidate tracks for the TPC signal sample. The arrow indicates the accepted events. . . . 72
38 A distribution of the number of delayed time-bin hits, categorised by the type of particle causing the hits for FGD1. This was not produced using the selection outputs and was instead taken from Ref. [106]. Note the data-MC discrepancy below the cut threshold is not fully understood. The 'unknown' category refers to cases where the truth information was not saved which tends to be the case for low energy neutral particles. 74
39 A distribution of the invariant mass, m_{inv}, of the leading and pair candidate tracks for the FGD signal sample. The arrow indicates the accepted events. . . 75
40 A distribution of the invariant mass, m_{inv}, of the leading and pair candidate tracks for the TPC control sample. The arrow indicates the accepted events. . . 75
41 A distribution of the invariant mass, m_{inv}, of the leading and pair candidate tracks for the FGD control sample. The arrow indicates the accepted events. . . 76
42 Distributions of reconstructed electron and pion momentum and angle, p_e, $\cos\theta_e$, p_π and $\cos\theta_\pi$, for the TPC signal sample. Events are categorised by the event type categorisation. Events with $p_e < 350$ MeV$/c$ are omitted. 78
43 Distributions of true invariant hadronic mass W true momentum transfer Q^2 for the TPC signal sample. Events are categorised by the interaction type categorisation. Events with $p_e < 350$ MeV$/c$ are omitted. 78
44 Distributions of reconstructed electron and pion momentum and angle, p_e, $\cos\theta_e$, p_π and $\cos\theta_\pi$, for the TPC signal sample. Events are categorised by the main track (upper) and pion track (lower) particle species topologies. Events with $p_e < 350$ MeV$/c$ are omitted. 79
45 Distributions of reconstructed electron and pion momentum and angle, p_e, $\cos\theta_e$, p_π and $\cos\theta_\pi$, for the FGD signal sample. Events are categorised by the event type categorisation. Events with $p_e < 350$ MeV$/c$ are omitted. 80

46 Distributions of true invariant hadronic mass W true momentum transfer Q^2 for the FGD signal sample. Events are categorised by the interaction type categorisation. Events with $p_e < 350\,\mathrm{MeV}/c$ are omitted. 80
47 Distributions of reconstructed electron momentum and angle, p_e and $\cos\theta_e$, for the FGD signal sample. Events are categorised by the main track particle species categorisation. Events with $p_e < 350\,\mathrm{MeV}/c$ are omitted. 81
48 Phase space diagrams for the true lepton kinematics (upper) and true pion kinematics (lower) (p_e^{true}, θ_e^{true}, p_π^{true}, $\theta_\pi^{\mathrm{true}}$). Plots on the left only show signal events. Plots on the right only show background events. The z-axis indicates the POT-normalised MC event count per bin. The red boxes show the in-phase space regions. 82
49 Distributions of reconstructed electron and pion momentum and angle, p_e, $\cos\theta_e$, p_π and $\cos\theta_\pi$, for the TPC control sample. Events are categorised by the event type categorisation. 83
50 Distributions of reconstructed electron and pion momentum and angle, p_e, $\cos\theta_e$, p_π and $\cos\theta_\pi$, for the FGD control sample. Events are categorised by the event type categorisation. 84
51 $N-1$ bar charts of the selection cut performance for the TPC signal sample (upper left), FGD signal sample (upper right), TPC control sample (lower left) and FGD control sample (lower right). These indicate the change in purity and efficiency, ρ_i and ε_i, as a result of the i^{th} cut in each sample. Note that the leading track momentum constraint of $350\,\mathrm{MeV}/c$ is not applied. 85
52 Truth-level comparison of the reconstructed electron (upper) and pion (lower) momentum $p_{e,\pi}$ and angular $\cos\theta_{e,\pi}$ distributions for particles which cross the TPCs and leave reconstructable tracks. These plots only show signal MC events. 86
53 Two-dimensional histograms showing the true pion momentum p_π (left) angular $\cos\theta_\pi$ (right) distributions against the equivalent reconstructed variables. These plots are only shown for signal events which enter the FGD sample. 87
54 The pion momentum resolution $(p_{\mathrm{true}} - p_{\mathrm{reco}})/p_{\mathrm{true}}$ as calculated from Michel electron FGD hits, as a two-dimensional, signal-only histogram as a function of true pion momentum (left) and as a one-dimensional histogram with background events included (right). 87

55 The selection efficiency as a function of true lepton and pion kinematics, p_e, $\cos\theta_e$, p_π and $\cos\theta_\pi$, for the TPC, FGD and combined signal samples with all selection cuts applied. The green distribution show the true signal events which pass all selection cuts. 88
56 Two-dimensional distributions of the selection efficiency as projected onto true electron kinematics (left) and true pion kinematics (right). The z-axis indicates the efficiency values for each two-dimensional bin. 89
57 Shape comparisons of the control sample and signal sample in-FGD photon events for the reconstructed electron kinematics, p_e and $\cos\theta_e$ (upper), as well as for the true pion momentum p_π and true momentum transfer squared Q^2 (lower). All histograms are normalised to unity and error bars indicate the statistical uncertainties. 90
58 Comparison of the electron momentum with events categorised by interaction types for in-FGD photons only for the combined signal samples (left) and the combined control samples (right). 91
59 Comparison of the electron momentum with events categorised by interaction types for in-FGD photons only for the combined signal samples (left) and the combined control samples (right). 91

60 The relative errors overlayed on the signal samples for the P0D veto (tl), TPC veto (tr), upstream ECal veto (bl) and ECal polar angle veto (br) pile-up systematic uncertainties. 96
61 Distribution of the reconstructed distance between the leading and paired track for the electron-positron pair control sample. The black line indicates where the distance cut is imposed in the selection. 97
62 The relative error for the FGD vertex association systematic uncertainty projected onto electron momentum. 98
63 The relative error for the FGD pion Michel electron resolution systematic uncertainty projected onto FGD pion momentum. 98
64 The relative error due to the total detector systematic uncertainty as a function of electron kinematics and pion kinematics. Grey histograms show events of all types which pass the selection cuts organised by sample. The upper four plots show the signal samples and the lower four pots show the control samples. . . 100

65 The fractional error as a function of neutrino energy on the ν_μ (left) and ν_e (right) flux from different sources. The solid black line indicates the total uncertainty. These plots are taken from Ref. [119]. 101
66 The systematic uncertainties on the neutrino beam fluxes, distinguished by contributions from ν_μ, $\bar{\nu}_\mu$, ν_e and $\bar{\nu}_e$ measurements. The grey histogram shows the true neutrino energy for all events which pass the selection. 102
67 An example of a spline response function which is used to store information about an event weight as a function of arbitrary cross section parameter values. 105

68 The true binning scheme for the INPS region imposed on the true electron phase space for the lower p_π bin (left) and the upper p_π bin (right). The red regions indicate the bin edges in electron kinematics and the number is the true signal event rate. 111
69 The efficiency for all truth space bins. The template parameter indices correspond to the true bin indices listed in table XVI. 112
70 Distributions of the post-fit (left) and cross section (right) χ^2 values for 1005 fits with statistical and systematic uncertainty fluctuations enabled. The blue histogram shows the pseudo data distribution, the black line shows the χ^2 fit to this histogram, and the red lines show the theoretical χ^2 distribution for the annotated number of degrees of freedom. 116
71 The cross section results for all closure studies. The upper four plots show the cross section values. The lower four plots show the fractional bias between the true and measured cross sections. 117
72 The cross section results for all stress tests and physics-motivated studies. The upper four plots show the cross section values. The lower four plots show the fractional bias between the true and measured cross sections. 118

73 Signal sample histograms of the neutrino event rate as a function of reconstructed neutrino energy assuming CCΔ kinematics. Note that these histograms show the pre-fit MC event rates. 119
74 The nominal and post-fit number of reconstructed events in the three-dimensional binning scheme for each sample from the data fit. The binning indices used for these plots are listed by sample in appendix A.2. 120
75 The template and nuisance parameter values and uncertainties for the data fit. The lower plots show the fractional difference between the pre-fit and post-fit parameters. 121

76 The one-dimensional and total flux-integrated cross section results for the data fit comapred to the NEUT and GENIE predictions. Note the second p_e bin extends to 30 GeV but is restricted to 10 GeV in the plot for clarity. 122

77 A schematic diagram of the Hyper-Kamiokande far detector. This graphic is taken from Ref. [49]. 127

78 A plot of the beam centre reconstruction residuals, showing the difference between the true and reconstructed beam centre positions for different opening half-angle values. This plot was reproduced from Ref. [130]. 133

79 An exploded CAD schematic of the collimator design with main components labelled. 134

80 A CAD schematic of the design of an assembled collimator with main components labelled. 135

81 The collimator test-stand with main devices and components labelled. The apparatus is enclosed within a dark box which is closed during operation. . . . 136

82 Cross-sectional images of the collimator beam at different z-positions for a typical scan. 138

83 Example plots of the beam divergence (left) and horizontal profile (right) of a typcial collimator scan. 140

84 Plots showing the alignment tolerances along the x- and z-directions, where Δx and Δz represent small shifts of the fibre-lens separation in these directions. The x- and z-directions are perpendicular and parallel to the beam axis respectively. 141

85 A plot of the beam divergence values obtained as a function of fibre-lens separation. 142

86 Plots of the beam expansions (left) and horizontal beam profiles (right) for the assembled collimator using different input wavelengths. 143

87 Cross-sectional images of the collimator beam at different z-positions for a preliminary far-field study. 145

88 Beam divergence values for the far-field study. 145

List of Tables

I A table summarising the most recent best-fit neutrino oscillation parameter measurements from T2K [43], NOvA [47], MINOS [40] and Chooz [41]. These results are reproduced from Ref. [48]. 18

II The latest neutrino oscillation parameter results from the T2K experiment for both normal and inverted mass orderings. These results are reproduced from Ref. [45]. 40

III A table of the shared event selection cuts common between all samples. The cut number indicates the order in which these are applied. The purpose and implementation of each selection cut is described in sections 5.1.1-5.1.3. . . . 66

IV A table of the sample-specific selection cuts. The cut number indicates the order in which these are applied. The purpose and implementation of each selection cut is described in sections 5.1.4-5.1.7. 66

V The number of events passing the 40 mm pair separation cut and the efficiencies for data and MC. The values and errors for the efficiency are calculated using the Clopper-Pearson extraction method in `root` [118]. 97

VI List of the total relative error values for each source of systematic uncertainty due to detector effects split by sample. 99

VII List of the total relative error values for each source of systematic uncertainty due to detector effects split by event type. 101

VIII The overall uncertainties on the flux components of the neutrino beam as measured at ND280. 102

IX A table of all cross section model parameters used for this analysis and their prior uncertainty values. The physical meanings of these parameters are discussed on the next page under the bullet point corresponding to the label in the physics column. Generally, each parameter corresponds to different types of events within a particular interaction mode such as CCQE, DIS, RES and COH, or additional processes such as FSI or multiple pion production (Mπ). . 103

X List of pseudo data studies conducted as part of fit validation. The description column contains a brief explanation of the pseudo data. The p-values for the fit and cross section result are also listed. The upper part covers the closure and coverage tests, and the lower part covers the stress tests. Note that the p-values for studies involving statistical fluctuations are for one random seed only. . . . 115

XI The systematic and statistical uncertainty contributions to the overall cross section error. 123

XII A table showing the number of collimators intended to be produced for each of the water Cherenkov detectors for Hyper-K. 131

XIII A table showing the measured beam divergence values for each wavelength. . . 143

XIV A table listing all of the systematic studies conducted as part of the internal review process. 144

XV The amounts of data and MC used by this analysis split by ND280 FHC run period and the status of the P0D. The quantification of data and MC is divided by the POT. 150

XVI Binning scheme for true electron and pion kinematics. Note the momentum columns have units MeV/c. 151

XVII Binning scheme for true electron and pion kinematics for the TPC sample. Note the momentum columns have units MeV/c. 152

XVIII Binning scheme for true electron and pion kinematics for the FGD sample. Note the momentum columns have units MeV$/c$. 152

XIX Binning scheme for true electron and pion kinematics for the TPC control sample. Note the momentum columns have units MeV$/c$. 153

XX Binning scheme for true electron and pion kinematics for the FGD control sample. Note the momentum columns have units MeV$/c$. 153

XXI The ν_μ energy binning scheme used for evaluating the flux systematic uncertainties. 154

XXII The ν_e energy binning scheme used for evaluating the flux systematic uncertainties. 154
XXIII The $\bar{\nu}_\mu$ energy binning scheme used for evaluating the flux systematic uncertainties. 154
XXIV The $\bar{\nu}_e$ energy binning scheme used for evaluating the flux systematic uncertainties. 154

XXV A table showing the main optical components for the collimating optics, the relevant vendor and component IDs. 155

ACKNOWLEDGEMENTS

First and foremost, I wish to thank my supervisors, Steve Boyd and Gary Barker, who have always been sources of wisdom and informed many of my decisions in a consistently approachable way. Much of my progress was only possible thanks to Dave Hadley, the consistent guidance and help navigating the collaboration process has undoubtedly helped me reach the stage of finalising and publishing my cross section analysis. The advancement of my work was also greatly helped thanks to my T2K colleagues. In particular, Sam Jenkins, Sophie King, Andrew Cudd, as well as the other cross section conveners Dan Cherdack and Margherita Buizza Avanzini. My cross section work has only reached this stage so swiftly thanks to many months of hard work from Sophie, Sam and Andrew on their own analyses which they have kindly and enthusiastically shared. I want to thank my other colleagues at Warwick, including Xianguo Lu, Ankush Mitra and Keith Jewkes.

I also want to thank Katharina Lachner for her friendship as a Warwick and T2K colleague. Not only for teaching me how to ski for the first time in Hakuba, but also for consistently ensuring we visited Uoyasu during our stays in Tōkai. I also wish to thank Menai Lamers James for her friendship and support throughout the course of my PhD. I would also like to thank my other T2K colleagues and friends I spent my time in Japan with, including Henry Wallace, Adam Speers, Ewan Miller and Paul Morrison. The months spent in Japan exploring Yamagata, Kyoto, Osaka, Nara and Nikko were truly unforgettable.

A brief mention must go Luke Lorimer, who taught me mathematics during secondary school. His teaching style and enthusiasm are what motivated me to study further mathematics and eventually embark on a physics degree. I would not be anywhere near this position without his efforts. Finally, I would also like to thank my friends, my parents, my sister and grandfather. Thank you as well, Dariia, for being an amazing part of my life.

DECLARATION

This thesis is submitted to the University of Warwick in support of my application for the degree of Doctor of Philosophy. It has been composed by myself and has not been submitted in any previous application for any degree. The work presented, including data generated and data analysis, was carried out by the author except in the cases outlined below:

- Section 4.3.2 – the pion kinematics reconstruction from Michel electrons was proposed by Xianguo Lu and developed by Sam Jenkins as detailed in Ref. [104].
- Chapter 5 – several of the selection cuts were originally designed by Sophie King, Georgios Christodoulou and Sammy Valder as part of or an adaptation of another selection detailed in Ref. [85]. Many of the remaining selection cuts and the selection software were developed by other T2K collaborators.
- Chapter 6 – the standard ND280 detector, flux and cross section systematic uncertainties were implemented by T2K collaborators.
- Section 7.1 – the fitting software was adapted from a package originally made by Andrew Cudd as described in Refs. [123, 125].
- Section 10 – the collimator design, test-stand and software were worked on and developed in collaboration with Steve Boyd, Ankush Mitra, Keith Jewkes, Billy Vinning, Martin Spangenberg and other Warwick colleagues.

ABSTRACT

Precise measurements of neutrino-nucleus interaction cross sections are becoming increasingly necessary as neutrino oscillation experimentation approaches a new precision era with the construction of Hyper-Kamiokande and DUNE. The off-axis near detector of the long-baseline neutrino experiment, T2K, currently produces some of the most accurate cross section measurements on a wide variety of nucleon targets. Recent results from the T2K far detectors have focused efforts towards investigating interactions involving pion production from electron neutrinos. This thesis presents the world's first measurement of this process on a carbon target using data from ND280. The total flux-integrated cross section is measured as $[5.04 \pm (0.94 \text{ stat.}) \pm (0.73 \text{ syst.})] \times 10^{-39}$ cm^2 nucleon^{-1}, which is lower than the predictions from the `NEUT` and `GENIE` event generators. The remaining part of this thesis describes the development of calibration devices for the Hyper-Kamiokande far detectors. The deployment of light-injection modules will facilitate continuous monitoring of the detector response and medium properties, both of which will serve essential calibration purposes as the experiment is readied for data-taking in the next few years.

List of Acronyms

BSM Beyond Standard Model

CC Charged current

CCQE Charged current quasi-elastic

CL Confidence level

COH Coherent

CP Charge-parity

DIS Deep inelastic scattering

ECal Electromagnetic calorimeters

EM Electromagnetic

FGD Fine-grained detector

FHC Forward horn current

FV Fiducial volume

HATPC High-angle TPC

ID Inner detector

INPS In-phase space

MC Monte-Carlo

NC Neutral current

OD Outer detector

OOFGD Out-of FGD

OOFGDFV Out-of FGD FV

OOPS Out-of phase space

P0D Pi-zero detector

PID Particle identification

PMT Photomultiplier tube

POT Protons on target

RES Resonance

RHC Reverse horn current

SM Standard Model

SSM Standard solar model

ToF Time of flight

TPC Time projection chamber

THESIS OUTLINE

This thesis is organised into three main parts. Part I presents the historical context behind neutrino physics and the formalisms used to describe neutrino-nucleus interactions and flavour oscillations. The T2K experiment and the main neutrino cross section analysis are described in part II. Part III is dedicated to the Hyper-Kamiokande experiment and the development of light-injection modules intended for deployment in the far detectors. A brief summary and outlook concludes the thesis in part IV.

Part I

NEUTRINO PHYSICS

INTRODUCTION TO PART I

Part I of this thesis describes the broad context of the main analysis by presenting a short review of neutrino history and the phenomenology relevant to this thesis. Chapter 1 presents an overview of the historical experiments that played key roles in the development of neutrino physics. This is largely organised in chronological order to emphasise how the theory was developed in line with new experimental discoveries. A latter emphasis is placed on neutrino oscillations which is one of the most extensively studied aspects of neutrino phenomenology today. Chapter 2 gives a summary of the theoretical framework describing the fundamental behaviour of elementary particles. The formalisms behind neutrino-matter interactions are then described with examples of the most common types of neutrino-nucleon scattering. A brief summary of historical and recent cross section measurements is also provided.

CHAPTER 1

INTRODUCTION TO NEUTRINO PHYSICS

1.1 Historical overview

1.1.1 Postulation

A new particle which would soon be called the neutrino was first postulated in 1930 by Pauli in order to explain how energy, momentum and spin are conserved during β-decays [1],

$$ {}^{A}_{Z}N \rightarrow {}^{A}_{Z+1}N' + e^{-} + \nu_e, \tag{1} $$

where A is the mass number and Z is the atomic number of the nucleus N. This interaction was originally believed to be a two-body decay in which an electron is produced at a specific energy corresponding to the transmutation of the nucleus from N to N'. Distributions of the β-decay electron energy spectrum were measured to be continuous rather than resembling the expected discrete peak observed from similar measurements of α- and γ-decays. Additionally, spectroscopic studies of nuclei such as ^{14}N demonstrated that many β sources had integer values for their spin quantum numbers [2]. Electrons were known to be spin-1/2 particles, so an explanation for the apparent loss of spin quantum number during the β-decay process was necessitated to conserve angular momentum. One proposed solution to these problems was the production of a neutrally charged spin-1/2 particle with a mass much smaller than the electron which interacts remarkably infrequently with matter. This particle was eventually named the *neutrino* ("little neutral one"). The hypothesis was that the available energy would be shared between the electron and the neutrino during the β-decay process, giving rise to the continuous

distributions seen in experimental results. This proposal represents the first discovery in the field of neutrino physics and was an integral contribution which led to the development of electroweak theory and later the Standard Model of particle physics.

1.1.2 Fermi theory and first detection

The theory of β-decays was developed by Fermi and Perrin by 1933 in order to underpin the mechanism behind this phenomenon at a fundamental level [3, 4]. They proposed that a neutrino is created simultaneously with the electron in processes such as

$$p \rightarrow n + e^{+} + \nu_e \quad \text{and} \quad n \rightarrow p + e^{-} + \bar{\nu}_e. \tag{2}$$

The Fermi theory was an early precursor to the weak interaction and was remarkably accurate at predicting some neutrino properties at low energies. The β-decay mechanism was postulated to be a four-fermion contact interaction with no intermediate mediating boson. The Fermi theory developed many of the first predictions associated with neutrino-nucleus interactions. An early implication of this theory was that a neutrino with energy 2 MeV would have an interaction cross section with nucleons of $\mathcal{O}\left(10^{-44}\right)$ cm^2. Experimentalists were therefore aware of the difficulties associated with neutrino detection and the requirements of a large target mass and intense neutrino flux.

In 1951, Cowan and Reines collaborated to directly detect neutrinos for the first time as the primary goal of "Project Poltergeist", also known as the Cowan–Reines experiment [5]. The test they devised strived to use a highly radioactive source to produce a large flux of anti-neutrinos which would then cause the inverse β-decay of nuclei in a target medium,

$$\bar{\nu}_e + p \rightarrow e^{+} + n. \tag{3}$$

This would result in large amounts of positron production, immediately followed by the production pairs of coincident γ rays due to electron-positron annihilation. To verify that these photons came from the expected interactions, additional γ ray production around 10 μs later was expected to occur as a result of neutron absorption by mixing $CdCl_2$ within the target mass,

$$n + {}^{108}\mathrm{Cd} \rightarrow {}^{109}\mathrm{Cd} + \gamma. \tag{4}$$

Detection of these signatures would directly measure the inverse β-decay process for the first time and validate Fermi's work. This idea was realised at the Savannah River nuclear reactor

where two large water tanks were surrounded by 1400 L of liquid scintillator. Photomultiplier tubes were designed and placed such that they would be sensitive to the double γ and delayed γ production signature. It was originally suggested that the Los Almos nuclear testing facility could be used with a nuclear explosion as the neutrino source, but the impracticality of repeating such an experiment led to Cowan and Reines using the Savannah River reactor. The experiment successfully observed the expected signal in 1956, representing the first detection of an anti-neutrino [6]. At the time of discovery, knowledge of neutrino anti-particles and flavour were not established and the particle detected was assumed to be a neutrino without any further identifying properties. The pair was awarded the 1995 Nobel Prize in Physics for the discovery of the neutrino.

1.1.3 Anti-neutrinos and neutrino flavour

By the 1960s, the electron and muon and their respective anti-particles were relatively well understood from experimentation whilst the electroweak theory was developed [7, 8, 9]. These efforts led to further questions about the neutrino, such as whether it would be distinguishable from its anti-particle and if the same types of neutrinos were produced in different decay modes.

Research conducted by Davis at the Savannah River and Brookhaven reactors attempted to detect the anti-neutrino capture interaction

$$\bar{\nu}_e + {}^{37}\mathrm{Cl} \rightarrow {}^{37}\mathrm{Ar} + e^- \tag{5}$$

for the first time [10]. Confirmation of this process would provide early indications that the neutrino and anti-neutrino behave in the same way. Davis constructed a 3900 L tank of carbon tetrachloride which would result in argon production occurring as implied in the above process. Argon would then be removed by sweeping the tank with helium and subsequently counted to estimate the number of anti-neutrino captures. However, Davis found that he could not detect this process from an anti-neutrino source, but was able to detect the conjugate interaction

$$\nu_e + {}^{37}\mathrm{Cl} \rightarrow {}^{37}\mathrm{Ar} + e^-, \tag{6}$$

which demonstrated that the neutrino and anti-neutrino interact differently with matter.

In 1962, Lederman, Schwartz, and Steinberger used a 15 GeV proton beam at Brookhaven to conduct one of the first accelerator neutrino experiments [11]. The proton beam was directed onto a beryllium target; proton-nucleon collisions in the target caused the production of charged

pions, which would then decay by either of the processes

$$\pi^+ \rightarrow \mu^+ + \nu_\mu \quad \text{or} \quad \pi^+ \rightarrow e^+ + \nu_e. \tag{7}$$

The neutrinos produced would then be captured by nucleons, subsequently producing particular leptons corresponding to the initial neutrino flavour,

$$\begin{aligned} \nu(\bar{\nu}) + n(p) &\rightarrow p(n) + e^{\pm}, \\ \nu(\bar{\nu}) + n(p) &\rightarrow p(n) + \mu^{\pm}. \end{aligned} \tag{8}$$

The target was surrounded by 13.5 m of steel and concrete shielding to reduce the large and numerous backgrounds. The recorded lepton tracks were studied to discriminate between muons and electrons. After several months of operation, experiment found that 34 single muon events were detected, but only six showers due to single electron production were observed. This provided evidence that there were different types of neutrinos and these interacted differently with matter, or at least that the neutrinos produced in the π^+ decay were different from those produced in the earlier β-decays. This was because the former of these processes produced muon neutrinos (ν_μ) which cannot produce electrons in neutrino-nucleon interactions, providing the first hints of lepton number conservation. The discovery of the muon neutrino and led to the trio being awarded the 1988 Nobel Prize in Physics. Flavour-conserving neutral current neutrino interactions were also discovered using this apparatus at Brookhaven.

In the late 1990s, the DONUT[1] experiment was commissioned to identify a third species of neutrinos, the tau neutrino (ν_τ), which was predicted by the electroweak theory. This similarly involved the production of neutrinos from a high-energy proton beam from the Tevatron which operated at 0.8 TeV at the time of discovery. The proton beam was directed at a tungsten target to produce $D_s\,(c\bar{s})$ mesons, which are capable of decaying to tau neutrinos by

$$D_s \rightarrow \tau^+ + \nu_\tau. \tag{9}$$

The neutrino beam was guided through steel shielding to veto other types of particles. The τ is identifiable from a 'kink' where a single charged lepton track will abruptly change direction, indicating a $\tau^+ \rightarrow e^+ + \bar{\nu}_\tau + \nu_e$ decay. The production of an electron would lead to subsequent electron showering which is picked up by the scintillating fibre tracker. This signature was detected and the ν_τ was discovered for the first time in 2000 [12].

[1] Direct Observation of the ν_τ, Fermilab (Chicago)

More recently, the development of the electroweak theory has facilitated precise means of determining the number of neutrinos which couple to the Z^0 boson. Measurements of the hadron production cross section around the Z^0 resonance have been performed which has a well-defined shape corresponding to the number of neutrinos the Z^0 couples to. Measurements around the resonance peak can be used to calculate the number of neutrinos, which can be compared to the theoretical prediction assuming any number of neutrino generations assuming negligible mass. Results for this measurement were initially obtained by SLD[2] [13] and later ALEPH[3] [14], followed by several other experiments with increasing precision. Plots showing a joint fit using these results are presented in Fig. 1.

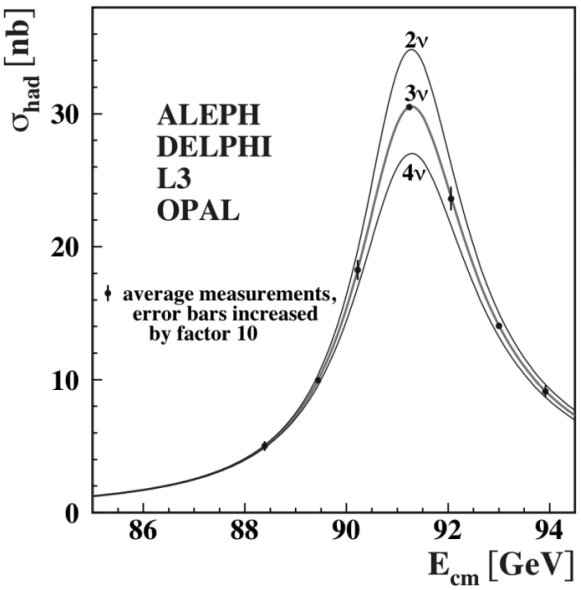

Figure 1. Joint measurements of the hadron production cross section around the Z^0 resonance from the ALEPH [14], DELPHI [15], L3 [16] and OPAL [17] experiments. The solid lines indicate the Standard Model predictions of the cross section assuming two, three and four weakly-coupling neutrinos of negligible mass. This plot was taken from Ref. [18].

As shown, there is a clear preference for the three neutrino fit from combined results from these four datasets. The theoretical framework and experimental evidence strongly supports the existence of three minimally-coupling neutrinos.

[2]SLAC large detector, SLAC (Stanford)
[3]Apparatus for LEP PHysics, CERN (Geneva)

1.1.4 The solar neutrino problem

Throughout the mid-1960s, neutrino experimentation was largely focused on neutrinos from natural astrophysical sources. Neutrino production in stars occurs through nuclear fusion; the proton-proton (pp) chains and the carbon-nitrogen-oxygen (CNO) cycle represent consecutive combinations of different fusion reactions which result in solar neutrino production. The dominant neutrino production modes are the fusion of ^{2}H $\rightarrow^3$ H and ^{3}He $+^4$ He $\rightarrow^7$ Li or ^{7}Be. The neutrinos produced in these fusion reactions are referred to as pp, pep and ^{7}Be neutrinos respectively. However, the vast majority of these production modes tend to create low energy ($E_\nu < 1$ MeV) neutrinos which are not easily detectable. Solar neutrino experiments therefore rely on neutrino production from ^{7}Be $\rightarrow^8$ B fusion reactions,

$$\begin{aligned} p \,+\, {}^7\mathrm{Be} \,&\rightarrow\, {}^8\mathrm{Be} \,+\, \gamma, \\ {}^8\mathrm{B} \,&\rightarrow\, {}^4\mathrm{He} \,+\, {}^4\mathrm{He} \,+\, e^+ \,+\, \nu_e. \end{aligned} \tag{10}$$

Neutrinos produced through this chain are referred to as ^{8}B neutrinos; a total energy of 18.2 MeV is produced in this process. The ^{8}B neutrinos carry around 80% of this energy, which is at least one order of magnitude greater than the more frequent pp chains. This process comprises only around one in every 10,000 fusion reactions in the sun. While photons produced inside the core of the sun can take years to reach the surface, neutrinos travel close to the speed of light and can reach the Earth in approximately eight minutes due to their infrequent interaction rates with solar matter. The neutrino flux as measured at the Earth was predicted by Bahcall using what is commonly referred to as the standard solar model (SSM) [19]. The flux predictions from different pp chains are shown in Fig. 2.

The Homestake experiment at Brookhaven, proposed by Davis and Bahcall, attempted to measure the neutrino flux from the sun for the first time [21]. This experiment consisted of a large tank of perchloroethylene situated 1.5 km underground to shield from cosmic rays. This aimed to detect the neutrino capture process $\nu_e \,+\, {}^{37}\mathrm{Cl} \,\rightarrow\, {}^{37}\mathrm{Ar} \,+\, e^-$ on a large target and therefore measure the neutrino event rate from the sun, providing a direct comparison with the predictions of the SSM. Surprisingly at the time, Homestake measured the solar neutrino flux to be approximately one third of what was expected from the SSM [22]. Over time, this result was supported by a number of other experiments including Kamiokande, which measured the solar neutrino flux to be approximately 47% of the expected value [23]. Many other experiments also produced statistically significant results indicating a deficit in the neutrino flux compared to expectations from the SSM. A complete summary of the historical solar neutrino discrepancies

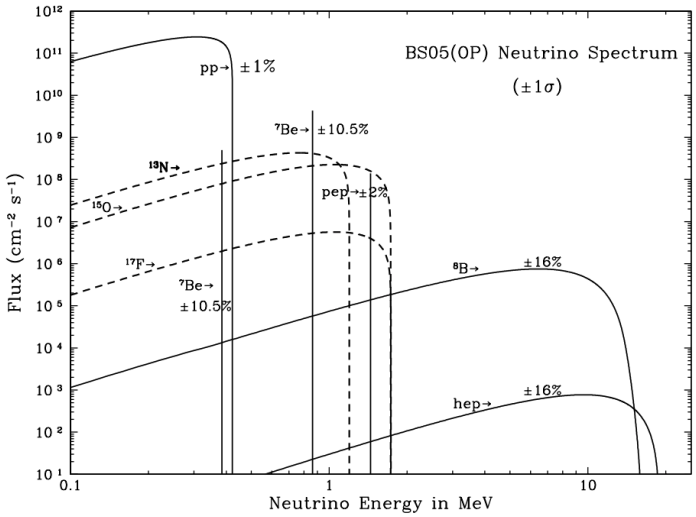

Figure 2. The predicted solar neutrino flux as a function of neutrino energy using the standard solar model [19] with the main processes annotated. This plot was taken from Ref. [20].

can be found in [24].

The cause of the anomaly would eventually be realised, which was that these experiments were only sensitive to one type of neutrino, and the remaining two-thirds had changed flavours to another type of neutrino which was not detectable by the experiments. This represents the first historical discovery of *neutrino oscillations*, which remains one of the most extensively studied aspects of neutrino phenomenology in the 21$^{\text{st}}$ century.

1.1.5 Atmospheric neutrinos

An additional natural source of neutrinos is from cosmic rays interacting with gases in the upper atmosphere. Atmospheric neutrinos were predicted to be the dominant backgrounds in future neutrino experiments such as searches for nucleon decays. So, extensive efforts were dedicated to understanding neutrinos from atmospheric sources. The atmospheric neutrino flux primarily originates from charged pion decays, such as

$$\begin{aligned} \pi^+ &\to \mu^+ + \nu_\mu \quad \text{and} \quad \mu^+ \to e^+ + \bar{\nu}_e + \nu_\mu, \quad \text{or} \\ \pi^- &\to \mu^- + \bar{\nu}_\mu \quad \text{and} \quad \mu^- \to e^- + \nu_e + \bar{\nu}_\mu. \end{aligned} \tag{11}$$

Many other atmospheric interactions also produce neutrinos, such as $K^\pm$ decays. Most atmospheric neutrino experiments tend to be located underground to shield from the co-produced leptons and hadrons which act as the main backgrounds in atmospheric studies.

The Kamiokande[4] experiment was the first of several generations of Japan-based experiments which utilised water Cherenkov technology [25]. Kamiokande was a large cylindrical tank of 3058 t of pure water surrounded by 1000 photomultiplier tubes. The original goal of this experiment was to detect proton decay, but it also had the capability of measuring both the flux and direction of solar and atmospheric neutrinos. The basis for this technology was that the charged leptons produced during neutrino-nucleus interactions in the water leave conical photon signatures known as Cherenkov radiation when exceeding the local speed of light. This phenomenon is often compared to sonic booms when objects exceed the sound barrier in the atmosphere. The appearance of the Cherenkov rings is distinct between electrons and muons, allowing for effective identification of the original neutrino interaction. The first results for atmospheric neutrino studies from Kamiokande were in obtained 1988 [26]. While the electron neutrino results agreed well with expectations, the number of muon neutrinos detected was $59 \pm 7\%$ of the expected value. Surprisingly, some other experiments using different technologies measured no equivalent deficit, while others did.

The presence of discrepancies in some experiments but not others suggested that the issues may have been associated with systematic errors, given that the discrepancies appeared to correlate with particular detector technologies. The Soudan-2[5] experiment was a 960 t iron tracking calorimeter which also demonstrated evidence of a similar muon neutrino deficit to that found at Kamiokande [27], implying that there was indeed a real phenomenon occurring which was associated with the event rate deficit. This deficit would be termed the *atmospheric neutrino anomaly*. A summary of the atmospheric anomalies as measured in various experiments at the time is discussed in Ref. [28].

The next major development on the atmospheric neutrino anomaly was recognised in 1998 from data collected by the upgraded next-generation water Cherenkov detector, Super-Kamiokande [29]. Super-Kamiokande contained 55 kt of water surrounded by over 11,000 photomultiplier tubes, vastly increasing the fiducial volume and sensitivity compared with its predecessor. The improved performance of Super-Kamiokande allowed neutrino event rates to be counted as a function of energy within the sub-GeV range. Given that Super-Kamiokande (36.2° N, 137.2° E) was capable of measuring neutrino directions, it was noticed that the extent of the muon neutrino deficit appeared to depend on the zenith angle. The zenith angle is a function of the distance the neutrino travels, and it was therefore noticed that the deficit size was associated with the distance that the neutrino travelled after production. A plot showing

[4] Kamioka Nucleon Decay Experiment, Mizoumi (Japan)
[5] Soudan Mine, Minnesota

the key result from Super-Kamiokande is shown in Fig. 3.

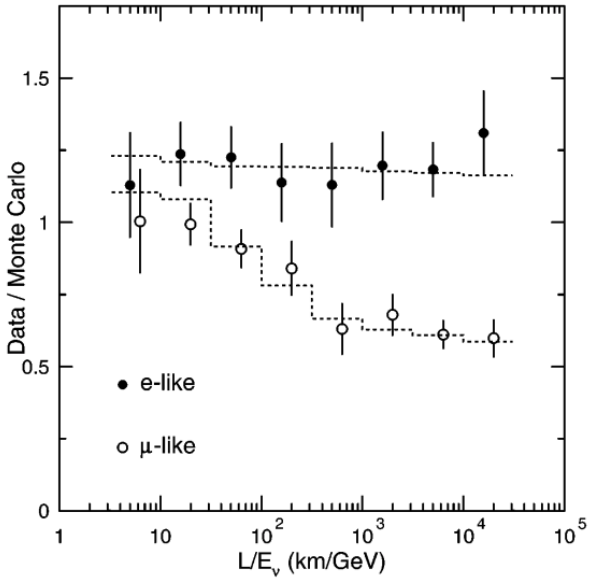

Figure 3. The measured electron and muon neutrino event rate dependence on the distance-energy ratio (L/E_ν) using data from the Super-Kamiokande experiment. The dotted lines represent the event rate predictions assuming the occurrence of two-flavour neutrino oscillations. This plot was taken from Ref. [29].

The event rate dependence on L/E_ν is now known to be a key property of neutrino oscillations, but at the time this result represented the first measurement of neutrino flavour changes. This also offered insight as to why different atmospheric experiments appeared to show disagreeing results. Each experiment measured atmospheric neutrinos at distinct locations and therefore unique distances from the original neutrino production in the atmosphere, but until then, only Super-Kamiokande was sensitive to the neutrino direction.

1.2 Neutrino oscillations

1.2.1 Predictions and early discoveries

By the early 2000s, it was clear that flavour oscillations of neutrinos were real and measurable. In addition to Super-Kamiokande [29], the SNO[6] experiment also began to make measurements of solar neutrinos and was able to provide clear evidence of neutrino oscillations in 2001 [30, 31]. SNO was a heavy water experiment situated 2 km underground which was able to

[6]Sudbury Neutrino Observatory, Sudbury (Canada)

distinguish between charged-current and neutral-current interactions depending on how the neutrino interacts with deuterium. The main results from SNO are presented in Fig. 4, which provided evidence of the ν_e flux partly oscillating to $\nu_{\mu,\tau}$.

As shown in Fig. 4, SNO was able to measure charged-current neutrino interactions which were exclusively from ν_e in this set-up. SNO was also able to measure neutral-current and elastic scattering interactions which can occur from all neutrino flavours in this particular experiment. The neutral-current band which is sensitive to all neutrino flavours agrees well with the expected SSM flux, ϕ_{SSM}, indicating that the sum of all neutrino fluxes was in line with expectations. The disagreeing shapes of the charged-current and neutral-current bands indicate that some of the flavour of some initial ^{8}B electron neutrinos had changed flavour.

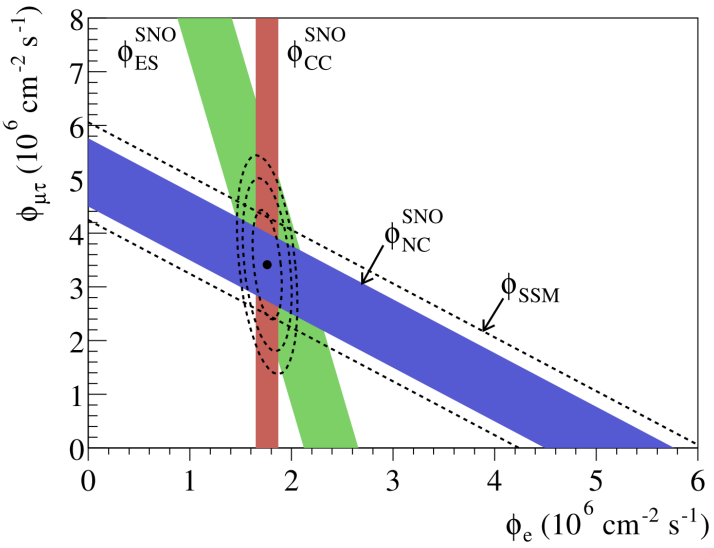

Figure 4. Neutrino oscillation results from the SNO experiment [30]. This shows the ^{8}B ν_e and $\nu_{\mu,\tau}$ fluxes, ϕ_e and $\phi_{\mu\tau}$, indicating the sources and predictions from the standard solar model [19]. These are broken down into measurements of charged current (CC), neutral current (NC) and elastic scattering (ES) processes. This plot is taken from Ref. [32].

This was the first time other neutrino flavours appearing as part of an oscillation experiment were detected. SNO was able to demonstrate not only that there was a deficit in the ν_e flux, but that the emergent $\nu_{\mu,\tau}$ fluxes were in-line with the SSM prediction. A.B. MacDonald and T. Kajita shared the 2015 Nobel Prize in Physics for the separate experimental discoveries of neutrino oscillations using SNO and Super-Kamiokande.

1.2.2 PMNS formalism

The formalism of flavour oscillations in the neutrino sector was already well-established at this point by Pontecorvo, Maki, Nakagawa and Sakata. These four first introduced the concept in 1962 through what is now referred to as the PMNS formalism [33, 34]. This formalism describes the weak flavour eigenstate ν_α of a neutrino from generation α as a linear combination of mass eigenstates ν_i,

$$|\nu_\alpha\rangle = \sum_i^3 U_{\alpha i} |\nu_i\rangle\,, \quad \text{with} \quad \begin{cases} \alpha \in e, \mu, \tau \\ i \in 1, 2, 3 \end{cases} \tag{12}$$

The mixing between flavour and mass eigenstates is encapsulated by the PMNS matrix $\mathbf{U}$. This is a unitary $\left(\mathbf{U}^\dagger = \mathbf{U}^{-1}\right)$ 3×3 matrix which links the flavour and mass eigenstates

$$\mathbf{U} = \begin{pmatrix} U_{e1} & U_{e2} & U_{e3} \\ U_{\mu 1} & U_{\mu 2} & U_{\mu 3} \\ U_{\tau 1} & U_{\tau 2} & U_{\tau 3} \end{pmatrix}. \tag{13}$$

This bears some similarities with the Cabibbo-Kobayashi-Maskawa (CKM) matrix which analogously describes flavour-changing phenomena in the quark sector [35]. The PMNS matrix is often expressed as three sub-matrices parametrised in terms of observable quantities related to the characteristics of neutrino oscillations,

$$\mathbf{U} = \begin{pmatrix} 1 & 0 & 0 \\ 0 & c_{23} & s_{23} \\ 0 & -s_{23} & c_{23} \end{pmatrix} \begin{pmatrix} c_{13} & 0 & s_{13} e^{-i\delta_{\mathrm{CP}}} \\ 0 & 1 & 0 \\ -s_{13} e^{i\delta_{\mathrm{CP}}} & 0 & c_{13} s \end{pmatrix} \begin{pmatrix} c_{12} & s_{12} & 0 \\ -s_{12} & c_{12} & 0 \\ 0 & 0 & 1 \end{pmatrix}. \tag{14}$$

In this expression, $c_{ij} = \cos\theta_{ij}$ and $s_{ij} = \sin\theta_{ij}$ where i and j are two distinct mass eigenstates. The θ_{ij} terms are the mixing angles which relate to the amplitude and therefore probability of neutrino oscillations between particular flavours. If $\theta_{ij} = \pi/4$, the mixing is maximal and all neutrinos of initial flavour α will, at some point, exist as flavour β. If $\theta_{ij} = 0$, then the flavour and mass eigenstates are identical and no flavour mixing occurs. The δ_{CP} term is the complex phase which quantifies the amount of charge-parity (CP) violation in neutrino oscillations; if $\delta_{\mathrm{CP}} \neq n\pi$ $(n = 0, 1, 2...)$, this implies CP violation occurs during neutrino oscillations and this is maximal if $\delta_{\mathrm{CP}} = \pm\pi/2$.

Remaining with the non-parametrised form of the PMNS matrix, after a duration t, the

neutrino flavour eigenstate as described in Eq. (12) will change from α to β with probability

$$\begin{aligned} P\left(\nu_\alpha \to \nu_\beta\right) &= |\left\langle \nu_\beta | \nu_\alpha(t) \right\rangle|^2, \\ &= \left| \sum_{i,j} U^*_{\alpha i} U_{\beta j} \left\langle \nu_j | \nu_i(t) \right\rangle \right|^2 . \end{aligned} \tag{15}$$

A plane-wave function can be used to describe the temporal evolution of the mass eigenstate of the neutrino as a function of its energy E_i,

$$|\nu_i(t)\rangle = e^{-iE_i t} |\nu_i(0)\rangle, \quad \text{with} \quad E_i = \sqrt{p_i^2 + m_i^2}, \tag{16}$$

where p_i and m_i are the neutrino momentum and mass respectively. In most cases, neutrinos are highly relativistic particles ($E \gg m$) and are assumed to have $E_i \simeq p_i$, which means an approximation can be made

$$E_i \simeq p + \frac{m_i^2}{2E_i}. \tag{17}$$

Given also that $L = t$, as it is assumed that $c = 1$, Eq. (15) becomes

$$P\left(\nu_\alpha \to \nu_\beta\right) = \sum_{i,j} U_{\alpha i} U^*_{\beta i} U^*_{\alpha j} U_{\beta j} \exp\left(-i \frac{\Delta m^2_{ij} L}{2E}\right), \tag{18}$$

where mass squared differences $\Delta m^2_{ij} \equiv m_i^2 - m_j^2$ quantify the relative mass of each neutrino and indicate whether the masses follow normal ordering ($m_{\nu_1} < m_{\nu_2} < m_{\nu_3}$) or inverted ordering ($m_{\nu_3} < m_{\nu_1} < m_{\nu_2}$). These terms also directly relate to the frequency of neutrino oscillations. For flavour mixing to occur, the mass squared differences must be non-zero and non-degenerate. Computing both summations gives the probability as an expression in terms of real and imaginary components,

$$\begin{aligned} P\left(\nu_\alpha \to \nu_\beta\right) = \delta_{\alpha\beta} &- 4 \sum_{i>j} \mathrm{Re}\left(U^*_{\alpha i} U_{\beta i} U_{\alpha j} U^*_{\beta j}\right) \sin^2\left(\frac{\Delta m^2_{ij} L}{4E}\right) \\ &- 2 \sum_{i>j} \mathrm{Im}\left(U^*_{\alpha i} U_{\beta i} U_{\alpha j} U^*_{\beta j}\right) \sin\left(\frac{\Delta m^2_{ij} L}{2E}\right). \end{aligned} \tag{19}$$

In some cases where the mass difference between two of the flavours is assumed to be very small, a two-flavour approximation is used. The PMNS matrix reduces to a simpler form

involving one mixing angle,

$$\mathbf{U} = \begin{pmatrix} \cos\theta_{12} & \sin\theta_{12} \\ -\sin\theta_{12} & \cos\theta_{12} \end{pmatrix}. \tag{20}$$

The expression for the probability of a neutrino oscillation changes to

$$\begin{aligned} P\left(\nu_\alpha \to \nu_\beta\right) = |U_{\alpha1}|^2|U_{\beta1}|^2 + |U_{\alpha2}|^2|U_{\beta2}|^2 + U_{\alpha1}U^*_{\beta1}U^*_{\alpha2}U_{\beta2}\exp\left(i\frac{L\Delta m^2_{12}}{2E}\right) \\ + U^*_{\alpha1}U_{\beta1}U_{\alpha2}U^*_{\beta2}\exp\left(i\frac{L\Delta m^2_{12}}{2E}\right) \end{aligned} \tag{21}$$

This then leads to the two-flavour oscillation probability as a function of just two unknown parameters, θ_{12} and Δm^2_{12},

$$P\left(\nu_\alpha \to \nu_\beta\right) = \sin^2\left(2\theta_{12}\right)\sin^2\left(\frac{\Delta m^2_{12}L}{4E}\right). \tag{22}$$

From this, it can be seen that the first probability maximum occurs when

$$L/E = \frac{4\pi}{|\Delta m^2_{12}|}. \tag{23}$$

Neutrino experiments which are capable of probing oscillation behaviour tend to require lengths of $\mathcal{O}(10^3)$ m and energies of $\mathcal{O}(10^{3\text{-}6})$ eV. So, a further approximation based on these units can be made,

$$\frac{\Delta m^2_{12}L}{4E} \simeq 1.267\frac{\Delta m^2_{12}}{\mathrm{eV}^2}\frac{L/E}{\mathrm{m/MeV}}. \tag{24}$$

Notably, the transition probability depends on L/E, the value of which can be controlled by experimentalists. This also represents the region most sensitive to neutrino oscillations and long-baseline neutrino experiments are designed with a beam power and near-far detector separation such that this region is probed. As an example, the T2K experiment (discussed further in part II) uses a neutrino beam with a peak energy of 0.6 GeV which is close to the probability maximum for a baseline of length 295 km.

1.2.3 Neutrino oscillations in matter

Neutrinos passing through a material are capable of interacting with the sub-atomic particles to such an extent that the flavour oscillation probabilities are affected. All neutrino flavours can

experience neutral current elastic scattering with matter nucleons,

$$\nu_\alpha + N \rightarrow \nu_\alpha + N. \tag{25}$$

However, since bulk matter does not contain muons or tau leptons, electron neutrinos exclusively have an additional interaction mode which other neutrino species do not. This is charged current elastic scattering,

$$\nu_e + e^- \rightarrow \nu_e + e^-. \tag{26}$$

An effective Hamiltonian, which combines the standard vacuum term ($\hat{H}_0$) and the additional electron neutrino-matter interactions ($\hat{V}$), can be expressed as

$$\hat{H}_{\text{eff}} = \hat{H}_0 + \hat{V}, \quad \text{where} \quad \hat{V} = \pm 2\sqrt{2} G_F E N_e, \tag{27}$$

where G_F is the Fermi constant, E is the neutrino energy and N_e is the electron number density. The effective mixing angle after considering matter effects, θ'_{12}, can be written as

$$\tan 2\theta'_{12} = \frac{\sin 2\theta_{12}}{\cos 2\theta_{12} - k}, \quad \text{where} \quad k = \pm 2\sqrt{2} G_F N_e E / \Delta m^2_{12}, \tag{28}$$

where the sign of k is positive for neutrinos and negative for anti-neutrinos. Notably, a resonance occurs when $\cos 2\theta_{12} = k$ and the oscillation behaviour depends on the sign of Δm_{12}. When $\theta_{12} = \pi/4$, Eq. (28) is maximal. This scenario is known as the Mikheyev-Smirnov-Wolfenstein (MSW) effect [36]. The sign of k also depends on whether neutrinos or anti-neutrinos are involved. This means experiments with significant matter effects, such as those measuring neutrinos passing through the Earth, are capable of probing this resonance and are capable of determining the neutrino mass ordering.

1.2.4 Parameter measurements

The discovery of neutrino oscillations represented a significant milestone in particle physics, many innovative experiments have made and continue to make important discoveries associated with this phenomenon by precisely measuring the aforementioned oscillation parameters, θ_{ij}, $|\Delta m^2_{ij}|$, sign(Δm^2_{ij}) and δ_{CP}. The combination of parameters which can be constrained depends on whether the experiment is studying the appearance or disappearance of a specific neutrino flavour. Appearance experiments measure the emergence of new flavours from an initially

pure neutrino beam to determine the appearance probability, $P(\nu_\alpha \to \nu_\beta)$. Disappearance experiments tend to use a high-intensity source of a particular type of neutrino and determine the survival probability, $P(\nu_\alpha \to \nu_\alpha)$, by measuring the presence of this flavour at a different location after oscillations have occurred. Oscillations of $\bar{\nu}_e \to \bar{\nu}_{\mu\tau}$ are typically used in reactor experiments to study $\bar{\nu}_e$ disappearance and perform measurements of θ_{13}. Accelerator experiments tend to look for ν_e appearance from $\nu_\mu \to \nu_e$ oscillations, also enabling sensitivity to θ_{13}. The disappearance of ν_μ can also be used by accelerator experiments to perform measurements of θ_{23} and Δm^2_{23}. The remaining parameters, θ_{12} and Δm^2_{12}, can be constrained from measurements of the solar neutrino flux.

One of the first experiments to precisely measure neutrino oscillation parameters was the KamLAND[7] experiment. This was a liquid scintillator experiment using a mixture of dodecane and pseudocumene contained within an 18 m diameter sphere constructed from stainless steel. KamLAND was designed to detect the $\bar{\nu}_e$ flux from three separate nuclear reactors in central Japan, exploiting the understanding that the $\bar{\nu}_e$ fluxes will have oscillated to different extents after travelling distinct distances to the detector. This experiment was also capable of measuring the anti-neutrino energy which allowed for precise measurements of the oscillation survival probability to be performed. Within half a year, KamLAND recorded the first evidence of $\bar{\nu}_e$ disappearance [37]. KamLAND then produced some of the first high-precision measurements of neutrino oscillations in 2008 and later [38, 39].

Since the results from KamLAND, many experiments have instead focused on studying a neutrino beam over long distances; these are known as long-baseline neutrino oscillation experiments. The MINOS[8] experiment [40] was the first of these; it relied on measuring the composition of a neutrino beam produced at NUMI[9] at a near and far detector separated by a distance of 735 km. Since MINOS, many novel reactor and long-baseline neutrino experiments have been constructed and have provided increasingly precise results. The most accurate measurements come from the reactor experiment Chooz[10] [41, 42], as well as long-baseline experiments such as T2K[11] [43, 44, 45, 46] and NOvA[12] [47]. A summary of the best-fit values for each parameter is shown in table I. The focus of this thesis is on the work done at T2K and a detailed overview of T2K experiment, its recent results and outlook are presented in part II

[7] Kamioka Liquid Scintillator Antineutrino Detector, Kamioka (Japan)
[8] Main injector neutrino oscillation search, Minnesota
[9] Neutrinos at Main Injector, Fermilab (Chicago)
[10] Chooz (France)
[11] Tōkai-to-Kamioka, Tōkai (Japan)
[12] NuMI Off-Axis ν_e Appearance, Fermilab (Chicago)

of this thesis.

Parameter	Normal ordering	Inverted ordering	Experiments
θ_{12} [°]	$33.45^{+0.012}_{-0.012}$	$33.45^{+0.78}_{-0.75}$	T2K, NOvA
θ_{23} [°]	$42.1^{+1.1}_{-0.9}$	$49.0^{+0.9}_{-1.3}$	T2K, NOvA
θ_{13} [°]	$8.62^{+0.12}_{-0.12}$	$8.61^{+0.14}_{-0.12}$	T2K, NOvA, Chooz
Δm^2_{12} [10^{-5}eV^2]	$7.42^{+0.21}_{-0.20}$	$7.42^{+0.21}_{-0.20}$	T2K, NOvA
Δm^2_{13} [10^{-5}eV^2]	$2.510^{+0.027}_{-0.027}$	-	T2K, NOvA
Δm^2_{23} [10^{-5}eV^2]	-	$-2.490^{+0.026}_{-0.028}$	MINOS
δ_{CP} [°]	230^{+36}_{-25}	278^{+22}_{-30}	T2K, NOvA

Table I. A table summarising the most recent best-fit neutrino oscillation parameter measurements from T2K [43], NOvA [47], MINOS [40] and Chooz [41]. These results are reproduced from Ref. [48].

1.2.5 Towards a new precision era

There are several new long-baseline and reactor neutrino experiments under construction which aim to constrain these parameters even further. Examples include Hyper-Kamiokande [49], DUNE[13] [50] and JUNO[14] [51]. An overview of Hyper-Kamiokande and its prospects are discussed in part III of this thesis.

There are many open questions associated with neutrino oscillations which are likely to be addressed by next generation experiments. The value of δ_{CP} will be measured with improved precision, indicating whether it favours maximal or minimal CP violation to a greater statistical significance, which would have profound implications on our understanding of the matter-anti-matter asymmetry of the universe. The sign of $\Delta m^2_{\ell 3}$, where ℓ depends on the ordering hierarchy, is also currently unknown. An explanation as to why θ_{13} is so much smaller than θ_{12} and θ_{23} also does not presently exist, nor does a reason for the PMNS and CKM matrices appearing very differently in terms of the magnitudes of their elements.

To achieve the most accurate measurements of these parameters, better constraints on the main systematic uncertainties are needed. A more recent focus towards neutrino-nucleus interactions has been necessitated by the increasingly precise results produced in long-baseline

[13] Deep Underground Neutrino Experiment, Fermilab (Chicago)
[14] Jiangmen Underground Neutrino Observatory, Guangdong (China)

experiments. In such experiments, the expected neutrino oscillation event rate is modelled by the expression

$$R(\vec{x}) \simeq \Phi(E_\nu) \otimes \sigma(E_\nu, \vec{x}) \otimes \varepsilon(\vec{x}) \otimes \rho(\vec{x}) \otimes P\left(\nu_\alpha \to \nu_\beta\right), \tag{29}$$

in which Φ is the neutrino beam flux, σ is the neutrino interaction cross section, ε is the detector efficiency, ρ is the purity and $P\left(\nu_\alpha \to \nu_\beta\right)$ is the oscillation occurrence probability of a neutrino from species α to β, all of which depend on either the neutrino energy E_ν or input kinematic variables $\vec{x}$ or both. Neutrino-nucleus cross sections are generally of $\mathcal{O}\left(10^{-42}\,\mathrm{cm}^2\right)$ and are very difficult to accurately measure and model. As a consequence, the cross sections are typically the leading sources of systematic uncertainty when measuring oscillation parameters. A lot of recent work in neutrino experimentation has focused on precisely measuring cross sections for a variety of interactions and targets; this is discussed extensively in chapter 2.

1.3 Other frontiers

1.3.1 The nature of neutrino mass

The Standard Model predicts neutrinos to be massless, but the occurrence of flavour oscillations implies that they should possess non-zero mass. This raises the question of how neutrinos obtain mass and whether they are Dirac or Majorana particles. An expected consequence of neutrinos being Majorana particles is that they should undergo neutrino-less double β-decay ($0\nu\beta\beta$), in which two neutrons each convert to protons and produce a pair of electrons, resulting in no final-state neutrinos being produced

$${}^{A}_{Z}N \;\to\; {}^{A}_{Z+2}N' \;+\; 2e^{-}. \tag{30}$$

Many novel experiments are being designed to measure this interaction. For example, the KamLAND experiment previously used to study neutrino oscillations has been upgraded to KamLAND-Zen which aims to record a $0\nu\beta\beta$ signature from a ^{136}Xe nucleus [52]. The half life of this decay is expected to be constrained by this and other experiments, which corresponds to placing upper limits on the absolute neutrino masses. A measurement of this decay would also provide evidence of total lepton number conservation violation.

If neutrinos are Majorana particles, then they are identical to their anti-particles. This would raise further questions as to how neutrinos acquire their mass. The *Seesaw mechanism* is

one of many beyond Standard Model theories which attempt to explain how neutrinos acquire mass and why their masses are so small compared to other leptons [53].

1.3.2 Supernova and relic neutrinos

Next generation neutrino observatories are expected to be sensitive to neutrinos from supernova explosions, as well as the diffuse supernova background, which represents the overall neutrino flux from all past supernovas. Measurements of the energy, time-dependence and anisotropy of the neutrino flux from supernovae could provide further insight into how neutrinos are produced in such events. There are also many competing models which describe supernova events and the neutrino flux would be able to help discriminate between these models [54].

Relic neutrinos are neutrinos which were produced very shortly after the Big Bang during neutrino-lepton decoupling. These, if measurable, would provide an analogous probe to the cosmic microwave background but substantially sooner after the Big Bang. The implications of this type of measurement and mapping would be profound and could offer further insight into outstanding questions in cosmology. It is possible that next-generation experiments may be able to detect relic neutrinos for the first time.

1.3.3 Sterile neutrinos

While many different measurements suggest that there are three weakly-interacting neutrinos, it is possible that further generations may exist which do not couple to the Z^0. This may be explained by the existence of right-handed chiral neutrinos. In turn, this could be related to dark matter, which is a term used to explain the why the majority of matter which interacts gravitationally appears to be otherwise invisible and non-interacting with any other particles through the electroweak or strong forces. Many other dark matter candidate particles have been proposed and it is possible that future neutrino experiments may be able to rule out some of these candidates [55].

The LSND[15] [56] and MiniBooNE[16] [57] experiments have both reported event excesses at low energy for ν_e and $\bar{\nu}_e$ events. While not currently statistically significant, one hypothesis relating to these excesses is that they may indicate a fourth, sterile neutrino taking part in the oscillation process. This would not couple to the Z^0 but could play an intermediate role in

[15] Liquid Scintillator Neutrino Detector, Los Almos (New Mexico)
[16] Mini Booster Neutrino Experiment, Fermilab (Chicago)

neutrino oscillations. These excesses are currently unresolved and are the subject of ongoing research at LSND, MiniBooNE and other experiments.

CHAPTER 2

NEUTRINO INTERACTIONS

As outlined in chapter 1, neutrinos are of especially strong interest in particle physics research. This chapter will give an overview of the Standard Model of particle physics and how neutrinos fit into the picture in section 2.1. Section 2.2 is dedicated to a generalised description of neutrino-nucleus interactions in terms of the cross section, nuclear and final state interaction models typically used for predicting neutrino-nucleus scattering events. Section 2.3 describes the most common types of neutrino-nucleus interactions relevant to the work in this thesis. A brief discussion of the status of neutrino cross section measurements is presented in section 2.4.

2.1 The Standard Model

The Standard Model (SM) of particle physics is a quantum field theory which describes the properties and behaviour of matter at an elementary level. The SM defines two main categories of fundamental particles: *fermions* which comprise all bulk matter and their heavier generations and *bosons* which mediate the interactions between particles. As shown in Fig. 5, these fermions and bosons are distinguished by having a spin quantum number of 1/2 or one respectively. The exception to this trend is the spin-0 Higgs boson which causes charged fermions and bosons to acquire mass through spontaneous symmetry breaking. Fermions are further distinguished into *leptons* and *quarks*, the latter of which uniquely carry colour charge and constitute *hadrons*. Each lepton and quark has a corresponding anti-particle with the same mass and opposite quantum numbers such as charge.

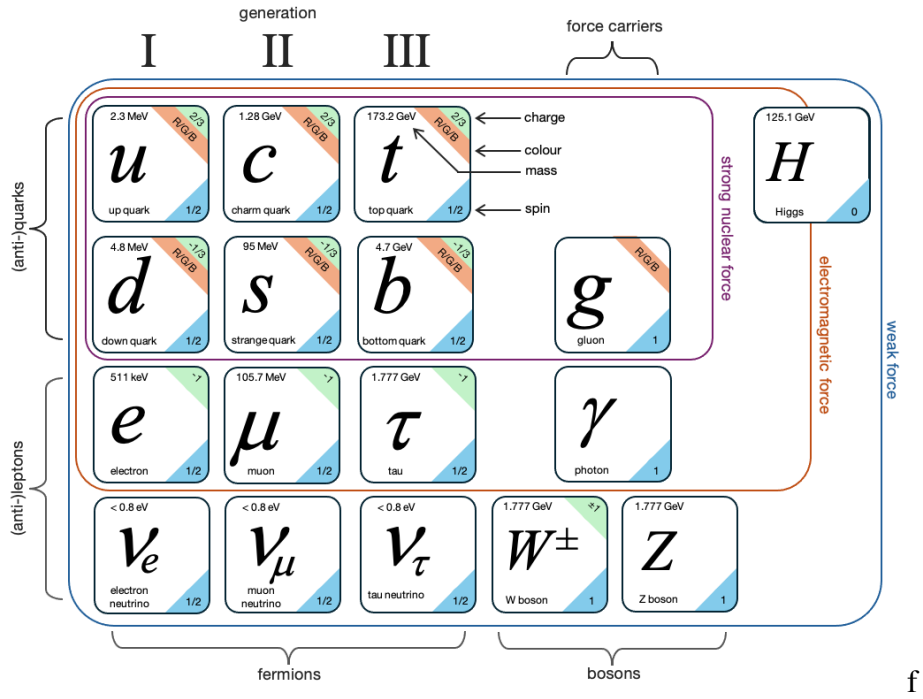

Figure 5. A graphic depicting all particles and interactions predicted by the Standard Model, alongside various properties including mass, electric charge, colour charge and spin. This custom diagram was inspired from a design in Ref. [58].

Fermions are capable of interacting weakly through the exchange of the $W^{\pm}$ and Z^0 bosons, as well as electromagnetically by exchanging photons (γ). Quarks uniquely interact through the exchange of gluons (g) as part of the strong interaction, but also experience the weak and electromagnetic interactions.

While the SM has been validated in many ways by experimental results, it is an incomplete description and likely a low-energy approximation of an undiscovered unified description of nature. For example, much of the detectable universe appears to be comprised of non-interacting 'dark' matter, the nature of which is not explained by the SM. The existence of the universe implies asymmetry in charge-parity which is not accounted for to a large enough extent in the SM. Neutrinos are predicted to be massless in the SM, despite exhibiting the behaviours of massive particles. Gravitational interactions are also not described in the SM. The focus of this dissertation is on neutrinos which, while having many aspects accurately described by the SM, remain the focus of ongoing research due to beyond SM properties and their potential role in the evolution of the early universe. Neutrinos represent a sub-group of leptons which are characterised by having low mass, neutral electric charge and only experiencing the weak interaction.

2.2 A formalism of neutrino-nucleus interactions

The way neutrinos interact with matter is the subject of significant ongoing research. A complete description of neutrino-nucleus interactions necessitates several considerations:

(i) A cross section model to describe how neutrinos interact with nucleons.

(ii) A nuclear model of nucleon distributions and behaviour within nuclei.

(iii) Appropriate treatment of particles as they emerge from a nucleus.

For the analysis presented in part II of this thesis, the NEUT Monte-Carlo (MC) generator is used [59, 60]. For some aspects of the analysis, the GENIE generator is also used for cross-checks and validation purposes [61]. These event generators are commonly employed for many different types of neutrino analyses in T2K and more widely among other neutrino experiments. The variables defined as part of this formalism retain their meaning through the remainder of this thesis. Complete derivations and further discussion of the main results in this chapter can be found in Refs. [62] and [63]

2.2.1 Nuclear models

The nuclear environments associated with large nuclei can be difficult to accurately model. Nuclear models, often referred to as *spectral function models*, are used to describe the initial states of nucleus-bound nucleons in terms of probabilistic momentum and position distributions. These models also encapsulate information about the nuclear potential which is associated with nucleons interacting within the nuclear medium.

For the simplest neutrino-nucleus interactions involving single nucleon targets, the impulse approximation is used [64]. The impulse model assumes that inbound particles have momenta such that they are capable of resolving individual nucleons within the nucleus and effectively only experience interactions from a single nucleon. This model also treats the final-state nucleons as non-interacting with the rest of the nucleons after production. Although these assumptions give rise to relatively straightforward calculations and predictions, the assumptions are decreasingly valid for larger multi-nucleon targets, given that nucleons should not be able to exist in identical states as a consequence of the Pauli exclusion principle. This model therefore works best for light-target scattering experiments involving small target nuclei such as ^{2}H.

The relativistic Fermi gas (RFG) model is a spectral function model which treats all nucleons within a nucleus of nucleon number A as non-interacting with momenta distributed

up to the Fermi momentum, p_F [65]. All nucleons are subject to the same nuclear potential. The key prediction is a probability factor which describes the likelihood of finding a nucleon with momentum $\vec{p}$ and energy E as

$$P_{\mathrm{RFG}}(|\vec{p}|,E) = \frac{6\pi^2 A}{p_F^2}\Theta(p_F - |\vec{p}|)\delta(E_p - E_b + E). \tag{31}$$

In this expression, E_p and E_b are the energy of a proton and the nucleus binding energy respectively and δ is a delta function. While this is a useful model, there is a hard cut-off on the particle momenta due to the presence of a Heaviside function Θ. More sophisticated spectral function models involve adaptations of the RFG model. One simple extension is the local Fermi gas (LFG) model, which treats the nuclear potential as having radial dependence in accordance with a density function [66],

$$p_F(r) = \left[3\pi^2\rho(r)\right]^{1/3}, \tag{32}$$

in which $\rho(r)$ is the nucleon density at radius r. While this addresses the discontinuities in the probability distributions associated with Pauli blocking in the RFG model, nucleons are still considered to be non-interacting which leads to some modelling inaccuracies. Variations of the RFG model are still used in conjunction with more sophisticated models in event generators.

The spectral function (SF) model incorporates intra-nucleon interactions for up to three-nucleon processes [67]. This utilises the shell model of nucleons and considers perturbations due to short-range nucleon-nucleon correlations. While this is generally more accurate than the variations of the Fermi gas model, there are several more models under development which aim to build on the SF model as part of refinements to event generators in the future. In practice, event generators such as NEUT and GENIE use a combination of all four models with some additional modifications. These generators are subject to continuous development within the neutrino interactions community.

2.2.2 Cross section models

The neutrino-nucleus interaction cross section σ effectively represents the likelihood and likely result of neutrino-nucleus interactions; it quantifies the size of the region for which an incoming neutrino would experience a particular weak interaction based on the arrangement of nucleons bound within a nucleus. Cross section predictions are used in conjunction with measurements of free parameters to build quantitative descriptions of neutrino interactions with matter.

The formalism for deriving neutrino cross sections uses predictions from the electroweak theory [7, 8, 9]. In these derivations, it is assumed that $\hbar = c = 1$. Full derivations of many neutrino-nucleon cross section results can be found in Refs. [62] and [63]. Note also that Greek indices (μ, ν) represent the space-time indices and summation is implicit.

A generic Feynman diagram for a neutrino-nucleon interaction is shown in Fig. 6. A neutrino of four-momentum $k^\mu(E_\nu, \vec{k})$ scatters off a nucleon N with initial four-momentum $p^\mu(E_N, \vec{p})$. The scattering process results in the production of a lepton ℓ with $k^{\mu\prime}(E_\ell, \vec{k}')$ and the nucleon is scattered to a new state N' with $p^{\mu\prime}(E_{N'}, \vec{p}')$. The outgoing lepton ℓ may represent either a neutrino or charged lepton depending on the interaction.

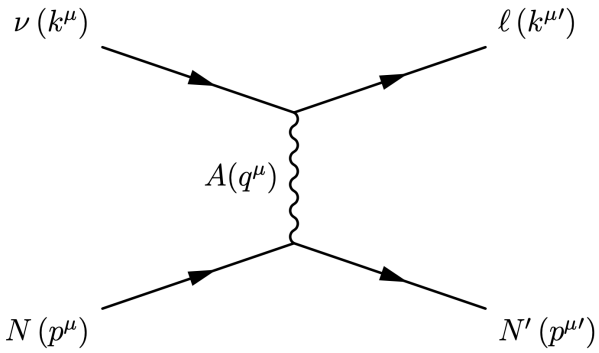

Figure 6. A Feynman diagram depicting generic neutrino scattering off a nucleon (ν-N). The bracketed terms indicate the four-momentum of each particle.

During this process, $q^\mu(\omega, \vec{q})$ is transferred between the neutrino and the nucleon through an arbitrary vector gauge boson A. The energy transfer from the neutrino to the nucleon is written as

$$\omega \equiv E_\nu - E_\ell, \tag{33}$$

and the equivalent transfer of four-momentum is

$$Q^2 \equiv -q^2, \quad \text{where} \quad q = (k - k') = (p - p'). \tag{34}$$

The quantity Q^2 is a function of the angle θ between the neutrino and final-state lepton

$$Q^2 = 2(E_\nu E_\ell - p' E_\nu \cos\theta) - m_\ell^2, \quad \text{where} \quad \cos\theta = \frac{\vec{k}\cdot\vec{k}'}{|\vec{k}||\vec{k}'|}, \tag{35}$$

and m_ℓ is the final-state lepton mass. The relative frequencies of particular neutrino interactions generally correlate with the values of Q^2. The total invariant mass of the hadronic components

is defined as

$$\begin{aligned} W^2 &\equiv (q+p)^2, \\ &= M_N^2 + 2pq + q^2, \\ &= M_N - 2 - 2M_N\omega - Q^2, \end{aligned} \tag{36}$$

where M_N is the mass of the nucleon. The Mandelstam variables, s and u, can be substituted to simplify the results of this formalism

$$s \equiv (k+p)^2 = (k'+p')^2, \quad u \equiv (p'-k)^2 = (k'-p)^2, \tag{37}$$

where s represents the centre of mass energy squared.

The general Lorentz invariant matrix element $\mathscr{M}$ corresponding to the Feynman diagram in Fig. 6 can be broken down into charged current (CC) and neutral current (NC) processes, the former of which produces charged leptons. The vector gauge boson A is the $W^{\pm}$ and Z^0 for CC and NC processes respectively. Calculations for specific processes require the invariant matrix element to be evaluated. This is a function of the leptonic and hadronic currents, l^{μ} and J^{μ}, as well as several free parameters of the electroweak theory including the Cabibbo angle θ_C and Fermi constant G_F. In general, for CC and NC processes,

$$|\mathscr{M}^{\mathrm{CC}}|^2 = \frac{G_F^2}{2}\cos^2\theta_C L^{\mu\nu}J_{\mu\nu}, \quad |\mathscr{M}^{\mathrm{NC}}|^2 = \frac{G_F^2}{2}L^{\mu\nu}J_{\mu\nu}, \tag{38}$$

where $L^{\mu\nu}$ and $J_{\mu\nu}$ are the leptonic and hadronic tensors which can be derived from their respective current terms. The quantities $L^{\mu\nu}$ and $J_{\mu\nu}$ evaluate distinctly for different processes. The form of $\mathscr{M}$ can then be evaluated using the Feynman rules to calculate the interaction cross sections for specific interactions. The generic neutrino-nucleon cross section element can be written as

$$\begin{aligned} d\sigma^{\mathrm{CC}} &= d^3p\, dE\, d^3k'\, P(E_b,\vec{p})\frac{G_F^2\cos^2\theta_C}{8\pi E_\nu E_\ell E_{N'} E_N} L_{\mu\nu}J^{\mu\nu}\delta(\omega - M_{N'} - E_b - E_{N'}), \\ d\sigma^{\mathrm{NC}} &= d^3p\, dE\, d^3k'\, P(E_b,\vec{p})\frac{G_F^2}{8\pi E_\nu E_\ell E_{N'} E_N} L_{\mu\nu}J^{\mu\nu}\delta(\omega - M_{N'} - E_b - E_{N'}), \end{aligned} \tag{39}$$

where $P(E_b,\vec{p})$ is a spectral function which depends on the the binding energy of the nucleus, E_b [68].

2.2.3 Final state interactions

Particles produced in nuclei are likely to interact with the nuclear medium as they exit. The effects within the nucleus are not directly measurable, and so the neutrino interactions, as well as the combination of nucleon-nucleon interactions, can only be inferred by particles which exit the nuclear medium. The combination of particles which are ejected from the nucleus and are usually measurable in detectors are referred to as the *final-state particles*. Accurate neutrino-matter interaction descriptions require careful treatment of the likely processes contributing to the set final-state particles which emerge from the nucleus.

Most neutrino event generators use a particular cascade model to account for final-state interactions [69, 70, 71]. These treat particles produced at the interaction vertex independently by evaluating the local nuclear density along discrete steps until the particle is ejected or absorbed. Pions and nucleons are treated separately within the nuclear medium. The nuclear density profile is typically taken as a Woods-Saxon distribution [72] and the relative probability of a final-state interaction is calculated based on this distribution, as well as the particle energy. Common interactions which affect final-state protons and pions include absorption, charge exchange, elastic and inelastic scattering, as well as additional pion production. The probability of each of these occurring is tuned using external constraints from measurements.

Given that only the final-state particles are measurable, neutrino interactions are classified by *topology* which indicates the initial neutrino flavour, whether the interaction is a CC or NC process, and what the combination of final-state particles is, such as ν_μCC0π or ν_eCC1π. Events of a particular topology are usually comprised of a combination of the different interactions mentioned in section 2.3; multiple types of interactions will produce the same set of final-state particles.

2.3 Types of neutrino-nucleus interactions

2.3.1 Charged current quasi elastic scattering

Charged current quasielastic (CCQE) scattering is the dominant type of neutrino-nucleon interaction for energies up to 1 GeV, and it remains prominent until around 10 GeV. CCQE scattering is also one of the main processes relevant to neutrino oscillation experiments; it is usually the underlying interaction which results in the production of detectable leptons, offering a means to indirectly infer the species of the interacting neutrino. During a CCQE scattering

event, a (anti-)neutrino scatters off a nucleon causing it to change from a neutron (proton) to a proton (neutron), simultaneously producing a charged lepton,

$$\begin{aligned} \nu_\ell + n &\rightarrow \ell^- + p, \\ \bar{\nu}_\ell + p &\rightarrow \ell^+ + n. \end{aligned} \tag{40}$$

Feynman diagrams of the CCQE scattering processes for neutrinos and anti-neutrinos are shown in Fig. 7.

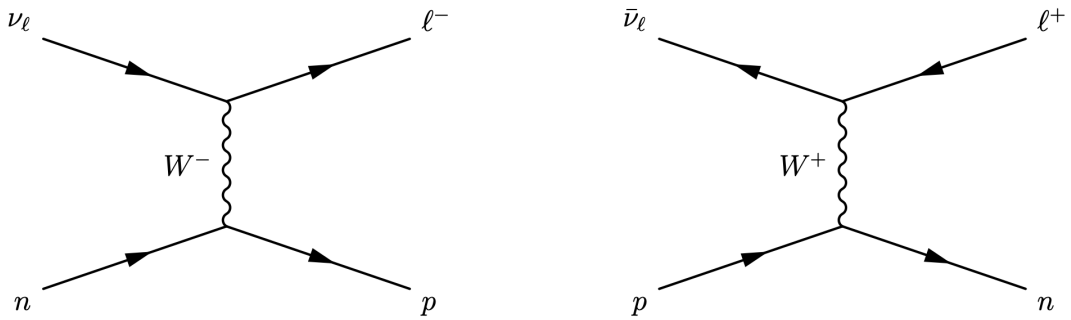

Figure 7. Feynman diagrams of the charged current quasielastic scattering of a neutrino off a neutron (left) and an anti-neutrino off a proton (right).

The cross section for CCQE scattering can be derived following the Llewellyn-Smith formalism [73]. The electroweak interaction Lagrangian is reduced to only consider CC interactions. The invariant matrix element $\mathscr{M}$ is proportional to the differential cross section with respect to Q^2. Evaluating $\mathscr{M}$ using the Feynman rules gives an expression for the differential cross section corresponding to the CCQE process

$$\frac{d\sigma}{dQ^2} = \frac{G_F M_N^2 \cos^2\theta_C}{8\pi E_\nu^2} \left[A \pm B\frac{(s-u)}{M_N^2} + C\frac{(s-u)^2}{M_N^4} \right], \tag{41}$$

where s and u are Mandelstam variables defined earlier, $s-u = 4M_N E_\nu - Q^2$ and E_ν is the

neutrino energy. The terms A, B and C are functions of Q^2

$$\begin{aligned} A(Q^2) &= \frac{m_\ell^2 + Q^2}{M_N^2}\left[(1+\eta)\,F_A^2 + (1-\eta)\left(\eta F_2^2 - F_1^2\right) + 4\eta F_1 F_2\right. \\ &\quad \left. - \frac{m_l^2}{4M_N^2}\left(\left(F_1+F_2\right)^2 + \left(F_A + 2F_P\right)^2\right) - \frac{1}{4}\left(\eta+1\right)F_P^2\right], \\ B(Q^2) &= 4\eta F_A\left[F_1 + F_2\right], \\ C(Q^2) &= \frac{1}{4}\left[F_A^2 + F_1^2 + \eta F_2^2\right], \end{aligned} \tag{42}$$

where the parametrisation $\eta = Q^2/4M_N$ has been used, m_ℓ is the mass of the lepton. The terms F_1, F_2, F_A and F_P are the charged current nucleon form factors which also depend on Q^2 [62]. The terms $F_{1,2}$ are the isovector form factors related by

$$F_{12} = F_{12}^p + F_{12}^n. \tag{43}$$

The isovector axial form factor F_A is assumed to have a dipole functional form

$$F_A(Q^2) = \frac{g_A}{\left(1 + Q^2/M_A^2\right)^2}, \tag{44}$$

where g_A is measured from β-decay experiments. The term M_A is the axial dipole mass which is measurable from quasi elastic (anti-)neutrino scattering studies; it scales with the size of the cross section for all CCQE interactions. The value of M_A has been studied extensively over the past 50 years; it has a weighted average value of 1.026 ± 0.021 GeV or 1.069 ± 0.016 GeV from neutrino and electron production experiments respectively [62]. Although this particular parametrisation has been effective, more precise recent measurements suggest there may be better parametrisations such as a z-expansion method [74]. The term F_P is the pseudoscalar form factor,

$$F_P(Q^2) = \frac{2M_N^2 F_A}{m_\pi^2 + Q^2}, \tag{45}$$

in which m_π is the pion mass. There is also a neutral current variation of this interaction which is neutral current elastic (NCE) scattering in which the initial- and final-state particles are identical and a Z^0 is exchanged,

$$\begin{aligned} \nu_\ell + n &\rightarrow \nu_\ell + n, \quad \bar{\nu}_\ell + n \rightarrow \bar{\nu}_\ell + n, \\ \nu_\ell + p &\rightarrow \nu_\ell + p, \quad \bar{\nu}_\ell + p \rightarrow \bar{\nu}_\ell + p. \end{aligned} \tag{46}$$

CCQE and NCE interactions tend to be the most common at low values of Q^2 and are generally concentrated within $Q^2 < 1$ GeV^2. Above $\sim$0.5-1 GeV^2, the other interaction modes tend to dominate in presence.

2.3.2 Resonant pion production

Resonant pion production is another common interaction mode which results in the temporary excitation of a nucleon resonance R^* which subsequently decays to a pion,

$$\nu_\ell + N \rightarrow \ell^\mp + R^*, \quad R^* \rightarrow \pi^\pm + N'. \tag{47}$$

where $N, N' = n, p$. The possible charged current resonant (CC-RES) interactions are

$$\begin{aligned} &\nu_\ell + p \rightarrow \ell^- + p + \pi^+, \quad \bar{\nu}_\ell + p \rightarrow \ell^+ + p + \pi^-, \\ &\nu_\ell + n \rightarrow \ell^- + p + \pi^0, \quad \bar{\nu}_\ell + p \rightarrow \ell^+ + n + \pi^0, \\ &\nu_\ell + n \rightarrow \ell^- + n + \pi^+, \quad \bar{\nu}_\ell + n \rightarrow \ell^+ + n + \pi^-. \end{aligned} \tag{48}$$

Resonant interactions tend to be significant at energies between 1 and 100 GeV and are the most common neutrino interaction modes at around 5 GeV. The dominant CC-RES processes involve the $\Delta(1232)$ baryon as the resonance state. An example of a CC-RES interaction involving positive pion production from a $\Delta(1232)$ resonance produced from neutrino-neutron scattering is shown as a Feynman diagram in Fig. 8.

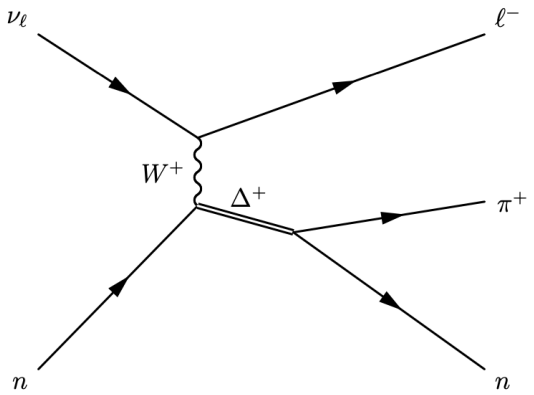

Figure 8. A Feynman diagram showing the inelastic scattering of a neutrino off a neutron with an intermediate $\Delta(1232)$ resonance state.

Higher resonances can also occur, often resulting in the production of other types of hadrons or multiple pions. There are also four neutral current resonant (NC-RES) processes

which do not result in charged lepton production but do give rise to charged and neutral pions. Both types of resonance processes are modelled by the Rein-Sehgal [75] and Berger-Sehgal models [76]. Resonance interactions tend to be sub-dominant for all Q^2 values and are generally most prominent below $Q^2 \simeq 0.5$ GeV^2.

2.3.3 Coherent pion production

A rarer interaction which results in pion production is charged current coherent (CC-COH) neutrino-nucleus scattering. During a CC-COH process, a neutrino transfers a small amount of momentum to a nucleus A which remains otherwise unchanged. A single pion is also produced,

$$\begin{aligned} \nu_\ell + A &\rightarrow \pi^+ + A + \ell^-, \\ \bar{\nu}_\ell + A &\rightarrow \pi^- + A + \ell^+. \end{aligned} \tag{49}$$

An example of a CC-COH process is shown as a Feynman diagram in Fig. 9.

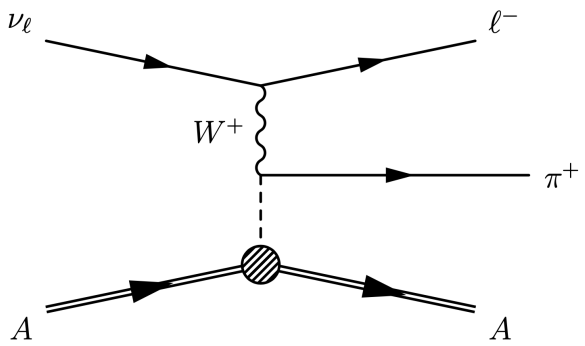

Figure 9. A Feynman diagram showing the coherent scattering of a neutrino off a nucleus.

In coherent interactions, the nucleus does not fragment into nucleons. These therefore only tend to occur when the momentum transfer Q^2 is low ($Q^2 \lesssim 0.1$ GeV^2). Coherent interactions are also modelled using the Rein-Sehgal [75] and Berger-Sehgal coherent models [76].

2.3.4 Deep inelastic scattering

Deep inelastic scattering (DIS) is where a neutrino interacts with a nucleus, causing it to fragment and produce many different hadrons represented by an arbitrary combination of final-

state particles, X. DIS interactions have both CC and NC variations,

$$\begin{aligned} \nu_\ell + N &\rightarrow \ell^- + X, \quad \bar{\nu}_\ell + N \rightarrow \ell^+ + X, \\ \nu_\ell + N &\rightarrow \nu_\ell + X, \quad \bar{\nu}_\ell + N \rightarrow \bar{\nu}_\ell + X. \end{aligned} \tag{50}$$

This type of interaction occurs at higher energies and is dominant above 10 GeV. The high-energy neutrinos are capable of resolving individual nucleons and therefore interacting with them more independently which leads to the fragmentation and hadron production effects. The set of final-state particles often includes one or multiple pions. The Bjorken scaling variables x_{Bj} and y_{Bj} are of particular relevance for DIS interactions,

$$\begin{aligned} x_{\text{Bj}} &\equiv \frac{Q^2}{2p\cdot q} = \frac{Q^2}{2M_N\omega} \quad \text{(lab frame)}, \\ y_{\text{Bj}} &\equiv \frac{p\cdot q}{p\cdot k} = \frac{\omega}{E_\nu} \quad \text{(lab frame)}. \end{aligned} \tag{51}$$

The quantity x_{Bj} represents the fraction of the initial-state nucleon momentum carried by the quark which interacts with the neutrino during a DIS event. The quark will carry $x_{\text{Bj}}p^\mu$, leaving $(1-x_{\text{Bj}})p^\mu$ within the hadronic system available for hadron production. Similarly, y_{Bj} represents the fraction of energy transferred from the neutrino to the hadronic system. An example of a DIS interaction is shown as a Feynman diagram in Fig. 10.

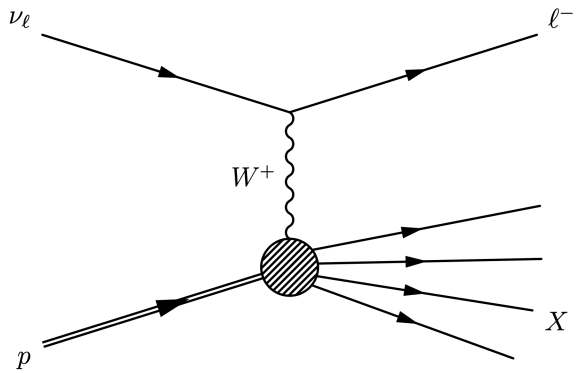

Figure 10. A Feynman diagram showing the deep inelastic scattering of a neutrino off a nucleus, resulting in fragmentation which generates many final-state particles represented by X.

DIS interactions start to become dominant at around $Q^2 \simeq 0.5$ GeV^2 and continue to remain so at higher values of Q^2. They also remain prominent below 0.5 GeV^2 but are less frequent than CCQE and RES interactions.

2.3.5 Other interactions

There are also several other interaction modes which are less relevant to the work described in this thesis. For example, the 2p2h (two-particle two-hole) interaction is defined as when multi-nucleon knock-out leads to the production of two nucleons. These tend to appear similar to CCQE interactions but the involvement of multiple nucleons means the energy transfer is more complicated and misidentification can lead to biases associated with the energy and momentum reconstruction. Accurate modelling of these interactions is therefore essential for neutrino oscillation analyses; experimental results from 2p2h measurements also suggest that the theoretical modelling is poor without extensive modifications. A more detailed discussion of 2p2h studies can be found in Ref. [77].

2.4 Status of neutrino cross section measurements

Many cross section measurements of particular topologies on a variety of nucleon targets have been performed over the last few decades. It is not possible to measure the specific interaction types, but the neutrino energy tends to correlate with Q^2 and therefore the relative presence of each interaction. Plots showing the theoretical cross sections as predicted using the NEUT event generator [59], broken down into the most common reactions, are presented in Fig 11. These show the predicted breakdowns of neutrino cross sections as a function of neutrino energy overlayed with some historical measurements.

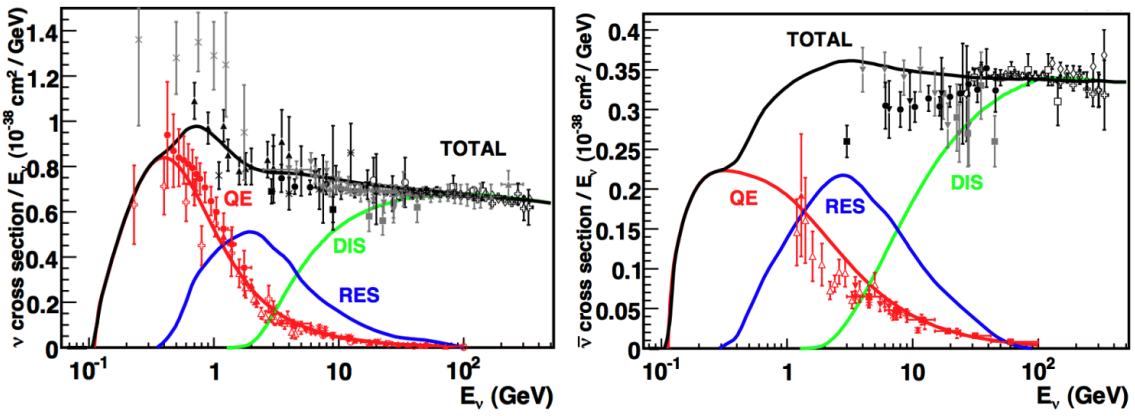

Figure 11. The predicted NEUT [59] neutrino-nucleus interaction cross sections as a function of energy for neutrinos (left) and anti-neutrinos (right) with the main interaction modes annotated. These plots are taken from Ref. [63] and the data entries represent many different measurements from a variety of experiments.

Since these results, more precise measurements of neutrino-nucleus cross sections have been performed using experiments such as T2K [43] and MINERvA [78]. A collection of results for the inclusive CC cross section is presented in Fig. 12. These plots show that there is a linear trend for the cross section as a function of energy in the region dominated by DIS interactions, while the lower energy CCQE region breaks away from this dependence. Measurements as a function of energy tend to be less common as higher precisions are reached. This is because many modern experiments tend to favour producing cross section results as a function of model-independent observables such as particle kinematics. These results are usually reported as an energy-averaged result with a flux prediction also provided.

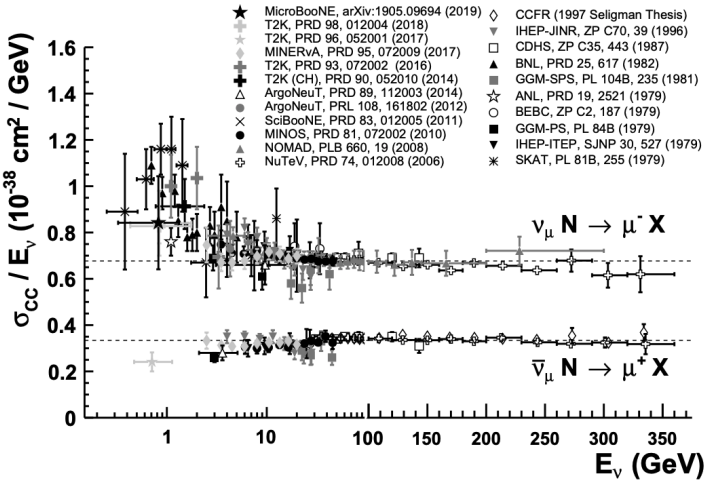

Figure 12. Measurements of the differential ν_μCC and $\bar{\nu}_\mu$CC cross sections as a function of energy from a variety of experiments including T2K [43], MINOS [40] and MINERvA [78]. This plot is taken from Ref. [79].

As well as the inclusive results, experiments including T2K and MINERvA have also produced differential cross section measurements for specific final-state topologies. These include the ν_μCC0π cross section on carbon and oxygen [80], a joint ν_μCC0π and ν_μCC0π measurement on water and hydrocarbon [81], as well as single-pion production cross sections [82]. Other experiments such as MINERvA and MicroBooNE have also produced similar results for variations of the ν_μCC cross sections on small and heavy targets [83, 84].

More recently, the T2K experiment has been able to measure the inclusive ν_eCC and $\bar{\nu}_e$ CC cross sections [85]. The flux-integrated differential cross section results are projected to electron momentum and angular distributions in Fig. 13. This represents a substantial improvement and inclusion of an anti-neutrino sample compared to the first ν_eCC inclusive

measurement at T2K [86].

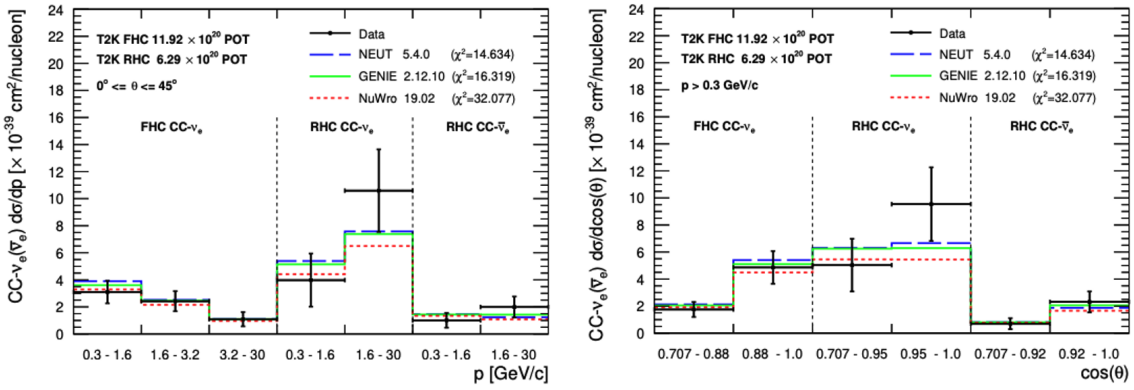

Figure 13. Measurements of the differential ν_eCC (left) and $\bar{\nu}_e$CC (right) cross sections as a function of electron momentum p and angle θ with comparisons to NEUT [59], GENIE [61] and NUWRO [87]. These plots are taken from Ref. [85].

In the last few years, work at T2K has resulted in many more novel results being produced. A recent example is a ν_μCC1π^+ analysis which uses transverse kinematic imbalance variables [88]. Another recent analysis performs the first measurement of the ν_μCC0π cross section using information from multiple detectors at different off-axis angles with respect to the neutrino beam [89]. A measurement of the CC-COH pion production cross section involving an anti-neutrino sample has also recently been performed [90].

T2K also has several upcoming measurements which are going through internal review processes, including the main work described in part II which is the first ν_eCCπ^+ measurement on carbon. As well as this, several new cross section results are expected to be produced such as ν_μNC1π without final-state protons [91], as well as a measurement of the ν_μCC0π cross section on H_2O and CH targets at a new water-based off-axis near detector [92].

Part II

MEASUREMENT OF THE ν_eCCπ^+ CROSS SECTION ON CARBON WITH T2K

INTRODUCTION TO PART II

Part II of this thesis presents the main analysis, which is the measurement of the ν_eCCπ^+ cross section on carbon using data from the Tōkai-to-Kamioka experiment. Chapter 3 introduces the experiment, summarises its physics goals and detector designs, as well providing an outline of phase-II of T2K which is scheduled until the operation of Hyper-Kamiokande commences. An overview of the analysis, focusing on key definitions and technical details, is given in chapter 4. Chapter 5 describes the process for selecting events for the signal and control samples using selection cuts; it also shows the main outputs which are used for cross section extraction such as the event rates for each sample and the selection efficiency. The systematic uncertainties associated with the detection and reconstruction methods in ND280, the neutrino beam flux and cross section model are presented in chapter 6. The process of organising the event selection outputs into inputs for the cross section fitter is described in chapter 7. Validation of the fitting process and cross section extraction using pseudo data studies are also summarised here. The data fit results are presented in chapter 8.

CHAPTER 3

THE T2K EXPERIMENT

The Tōkai-to-Kamioka (T2K) experiment [43] is a long-baseline neutrino oscillation experiment with the primary goal of measuring the PMNS matrix parameters by studying neutrino oscillations. T2K consists of three principal sites: the neutrino beamline which is produced at the Japan Proton Accelerator Research Complex (J-PARC), the near detector complex which is situated 280 m downstream of the neutrino source, and the Super-Kamiokande water Cherenkov tank at the far site in Kamioka 295 km to the west of J-PARC. A diagram of the T2K experiment is shown in Fig. 14.

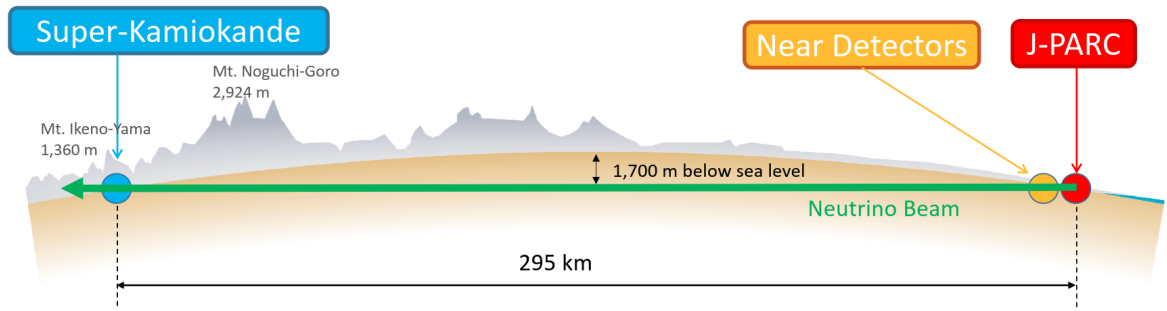

Figure 14. A cross-sectional diagram of the Tōkai-to-Kamioka experiment. The green arrow represents the neutrino beam which is produced at J-PARC and travels 280 m westwards to the near detector complex, followed by the Super-Kamiokande far detector which is a further 295 km to the west. This is taken from Ref. [93].

Measurements of neutrino oscillation parameters are performed at T2K by measuring the muon (anti-)neutrino disappearance and electron (anti-)neutrino appearance by comparing

event rates at the near and far detectors. The initial beam is purposefully comprised entirely of muon (anti-)neutrinos, and as they propagate towards the far detector, a proportion of these will appear as electron (anti-)neutrinos. The near detectors are used to constrain the main sources of systematic uncertainty on the oscillation parameter measurements, such as the uncertainties on the flux and neutrino-nucleus interaction cross sections. Neutrino oscillation events are recorded at the far site by studying the Cherenkov rings produced in the Super-Kamiokande water tank.

3.1 Physics goals and accomplishments

The original design goals of T2K were to measure several of the neutrino oscillation parameters with approximately 20 times the precision achieved in previous experiments such as Chooz [41, 42]. T2K set out to measure the values of the neutrino mass difference parameter Δm^2_{23} and mixing parameter $\sin^2\theta_{23}$ to within 10^{-4} eV^2 and 0.01 respectively. A measurement of θ_{13} was also proposed, which would demonstrate electron neutrino appearance from muon neutrinos for the first time. Constraints on δ_{CP} were also envisioned to infer whether CP violation can occur during neutrino oscillations. Additionally, T2K has the goal of precisely measuring neutrino cross sections for a variety of different target materials using the near detector complex, which was essential for achieving the necessary precisions on oscillation parameters.

After 12 years of operation and data analysis, T2K has been able to place precise constraints on the values of these parameters, exceeding the precisions originally proposed. The latest values and uncertainties of the oscillation parameters measured by T2K are shown in table II.

Parameter	**Normal ordering**	**Inverted ordering**
δ_{CP} [rad.]	$-1.97^{+0.97}_{-0.62}$	$-1.44^{+0.56}_{-0.59}$
$\sin^2\theta_{23}$	$0.561^{+0.019}_{-0.038}$	$0.563^{+0.017}_{-0.032}$
Δm^2_{32} [10^{-3}eV^2]	$2.494^{+0.041}_{-0.058}$	-
Δm^2_{31} [10^{-3}eV^2]	-	$2.463^{+0.042}_{-0.056}$

Table II. The latest neutrino oscillation parameter results from the T2K experiment for both normal and inverted mass orderings. These results are reproduced from Ref. [45].

In 2020, results from T2K suggested that the CP-violating phase, δ_{CP}, is closer to the

maximal possible value compared to the CP-conserving values of $\delta_{CP} = 0$ and $\delta_{CP} = \pi$ [46]. The range of likely values of δ_{CP} was excluded to 3σ (99.7% CL) to between -3.48 and 0.13 marginalised across both normal and inverted mass orderings. This excludes 46% of the parameter space to the same CL, suggesting the likely value of δ_{CP} may favour maximal amounts of CP violation. This measurement is displayed graphically in Fig. 15.

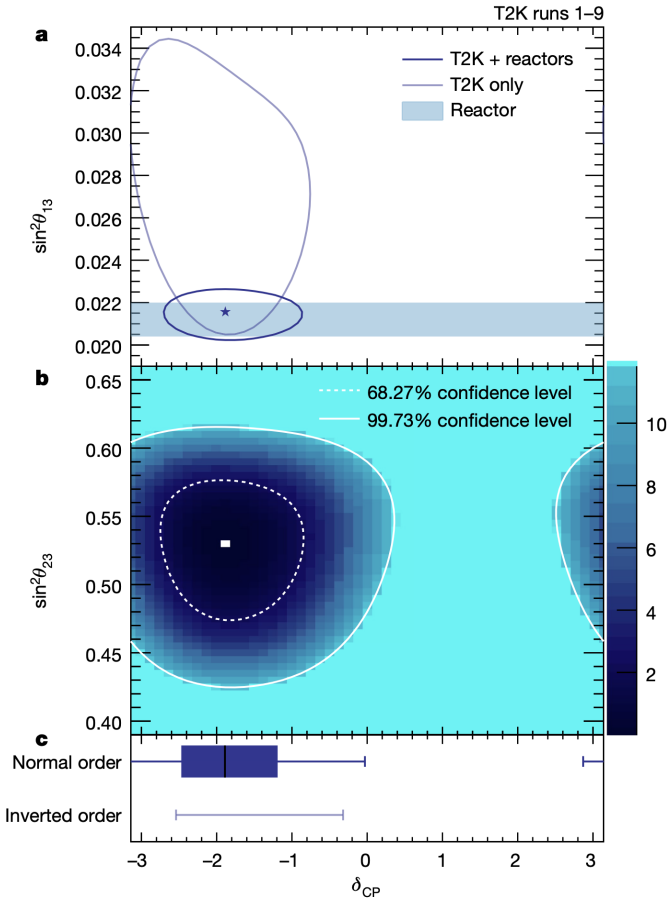

Figure 15. A measurement of the CP-violating phase, δ_{CP}, performed by the T2K experiment. This is presented as a two-dimensional confidence interval between δ_{CP} and the neutrino mixing angle parameters to 3σ, **a** $\sin^2\theta_{13}$ and **b** $\sin^2\theta_{23}$. The plot shows the limits with and without external constraints using data from reactor neutrino experiments. Plot **c** shows the one-dimensional confidence intervals and the best fit value of δ_{CP} is represented by the black line. This plot is taken from Ref. [46].

In addition to the neutrino oscillation parameters, T2K has also pioneered on neutrino cross section studies with precise measurements or with new, previously unstudied cross sections. Recent examples of these measurements using the T2K near detectors were discussed at the end of part I.

3.2 Neutrino beamline

The neutrino beam used in the T2K experiment is produced at the J-PARC[1] facility in Tōkai, Ibaraki. A 30 GeV proton beam is steered towards a graphite target; protons colliding with the target nucleons produce hadrons which are then focused into a decay volume [94]. The muon (anti-)neutrinos are generated from the decays of charged pions

$$\pi^{\pm} \rightarrow \mu^{\pm} + \overset{(-)}{\nu}_{\mu}. \tag{52}$$

The neutrino beamline is directed 2.5° below the axis line connecting Super-Kamiokande and J-PARC, allowing for a high-intensity beam to be produced at the energy corresponding to the first oscillation maximum at 0.6 GeV. The off-axis arrangement also narrows the width of the peak corresponding to this maximum, reducing background events that would be more prominent in a wider-band beam due to greater coverage of higher energy regions. A schematic of the neutrino beamline is shown in Fig. 16.

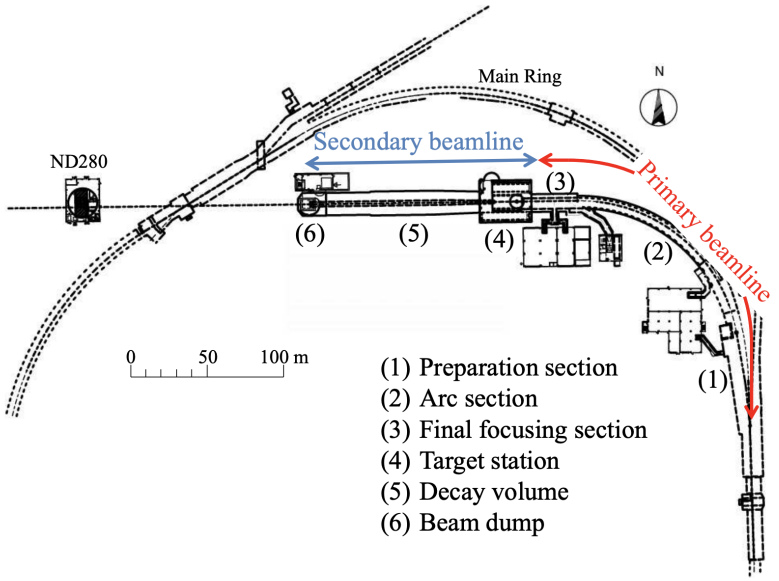

Figure 16. A schematic of the neutrino beamline at J-PARC with the primary beamline, secondary beamline and sub-sections annotated. This figure was taken from Ref. [43].

The neutrino beamline is comprised of primary and secondary parts, each of which consists of several sub-sections. The primary beamline contains the preparation, arc and final

[1] Japan Proton Accelerator Research Complex, Tōkai, Japan

focusing sections. In the preparation section, the proton beam is tuned for stable neutrino generation with minimal beam loss. Tuning is achieved using 11 normal conducting magnets which allow the beam to be accepted by the subsequent arc section. The arc section has a curvature radius of 104 m and ensures the beamline is directed downwards by 80.7° towards the far detector site in Kamioka. The final focusing section uses ten normal conducting magnets to focus the beam further with an additional downward angle of 3.637°.

The secondary beamline has the main purpose of producing neutrinos from the proton beam. The main sections of the secondary beamline are the target station, decay volume and beam dump. The target station collimates the proton beam using a baffle to protect the magnetic focusing horns from damage. This station consists of a graphite rod with length 91.4 cm and diameter 2.6 cm which corresponds to approximately 1.9 interaction lengths. Low density graphite $(1.8\ \mathrm{g/cm^3})$ is used to prevent the target core from melting during beam operation. The target core is sealed within a 0.3 mm thickness titanium casing. The electric charge of the pion and therefore the neutrino helicity is selected by adjusting the electromagnetic horn current polarity between forward horn current (FHC) and reverse horn current (RHC) modes [95]. The first magnetic horns collect pions produced at the target, while two other magnetic horns focus the pions towards the decay volume. A peak 320 kA current is used when running, which generates a magnetic field with a strength of 2.1 T.

The decay volume is a 96 m long steel tunnel with cross sectional areas of 2.5 $\mathrm{m^2}$ and 15.0 $\mathrm{m^2}$ at the upstream and downstream ends respectively. The decay volume is also shielded by a 6 m thick layer of concrete which is cooled to below 100° C using water. The beam dump is located at the downstream end of the decay volume; it is comprised of 75 t of graphite contained within a helium vessel and has a volume of $3.174 \times 1.94 \times 4.69\ \mathrm{m^3}$. Additional iron plates are placed within and around the beam dump. Together, these ensure that passing muons have momenta of at least 5 GeV/c.

A muon monitor is used to measure the beam intensity and direction for every bunch of passing muons. This is situated behind the beam dump and measures the direction of the neutrino beam to within 0.25 mrad, as well as the intensity to a precision of 3%.

3.3 Near detector complex

The near detector complex has the purpose of constraining the main systematic uncertainties on the number of predicted neutrino oscillation signal events, as well as measuring neutrino cross

sections and characterising the initial beam flux. There are three main near detectors: ND280, INGRID and WAGASCI, all of which are located at slightly different angles with respect to the neutrino beam and therefore have different peak neutrino energy values.

At the near detector complex, the neutrino beam is almost entirely comprised of muon neutrinos. Given that the site is 280 m from the start of the neutrino beamline, there are very small, but non-negligible contributions to the electron neutrino fluxes during both operating modes. The neutrino flux at the most off-axis near detector, ND280, is shown in Fig. 17.

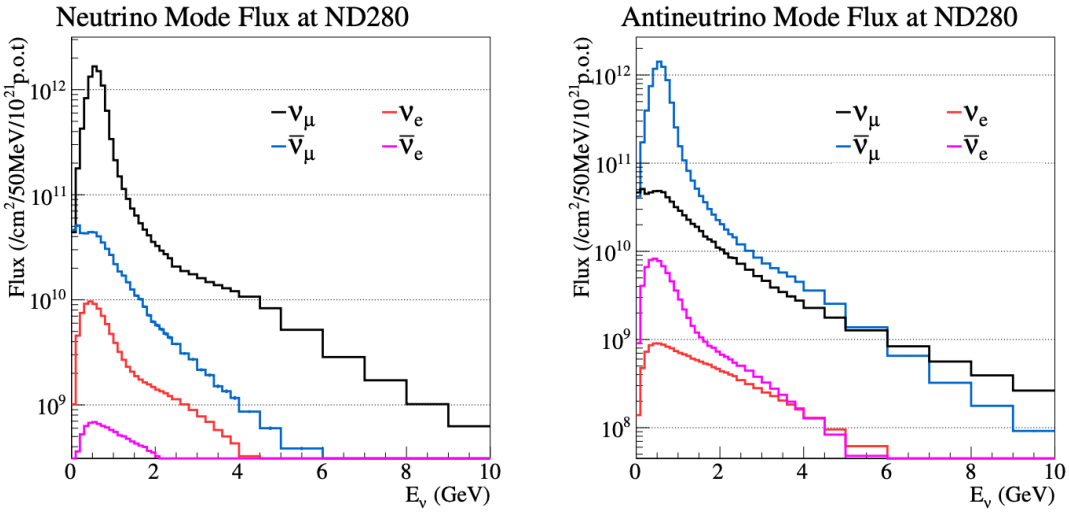

Figure 17. The neutrino flux as a function of energy, E_ν, in forward horn current mode (left) and reverse horn current mode (right) as measured at the off-axis near detector of T2K, ND280. The flux is distinguished by contributions from each neutrino flavour type. These plots are taken from Ref. [85].

3.3.1 ND280

ND280 is a tracking detector located 280 m down-stream of the neutrino beam source. It sits on top of the two other near detectors at the largest off-axis angle of 2.5°. This detector is comprised of several different types of sub-detector modules arranged with respect to the neutrino beam direction. The down-stream section of the detector consists of two fine-grained detectors (FGDs) and three time projection chambers (TPCs), all of which are enclosed by separate electromagnetic calorimeters (ECals). All ND280 sub-detector modules are surrounded by a 0.2 T UA1/NOMAD magnet which closes during operation. An exploded schematic of the arrangement of the sub-detector modules is shown in ND280 in Fig. 18.

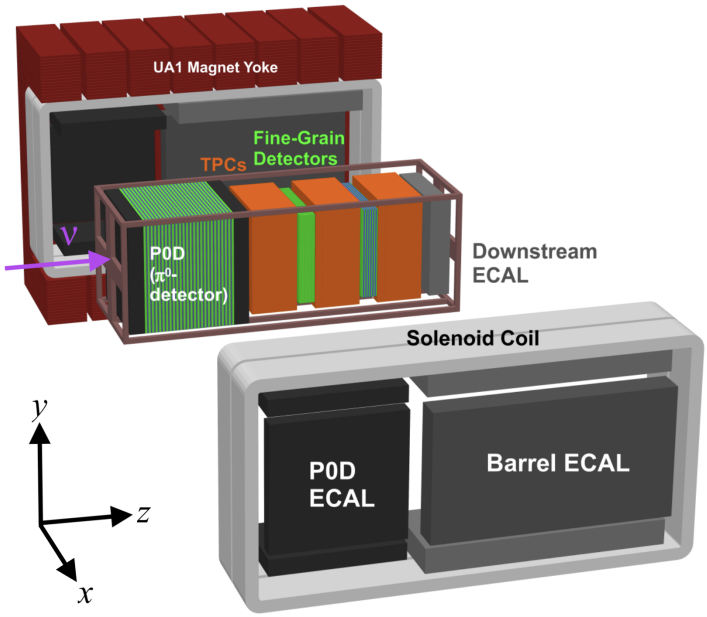

Figure 18. An exploded schematic of the off-axis near detector of the T2K experiment, ND280. The purple line indicates the approximate neutrino beam direction. This figure was taken and adapted from Ref. [43].

Pi-zero detector:

The most up-stream sub-detector module is the pi-zero detector (P0D) [96]. The P0D consists of 40 modules, each of which contains two arrays of triangular scintillator bars arranged perpendicularly to form a plane orthogonal to the z-axis of ND280. There are 134 horizontal bars and 126 vertical bars contained in each module. Each bar has a single coaxial hole with a wavelength-shifting fibre threaded through. The modules also contain a thin brass sheet, as well as a bag which can be filled with water, enabling particular interaction rates on water to be studied by subtracting the event rates as measured when the bags are empty from the rates measured when the bags are filled with water. The P0D is also surrounded by the upstream and central ECals which contain the same wavelength-shifting fibres, but the primary target masses are lead sheets instead of water bags. A schematic showing the structure of each P0D module is displayed in Fig. 19. The primary role of the P0D is to measure the neutral current π^0 production rate,

$$\nu_\mu + N \rightarrow \nu_\mu + N + \pi^0 + X, \tag{53}$$

on a water target. Interactions of this type are the dominant background to the ν_e appearance which is one of the main channels measured at T2K. The P0D has also been used to constrain the intrinsic ν_e component of the beam flux which is an irreducible background to the ν_e

appearance measurement.

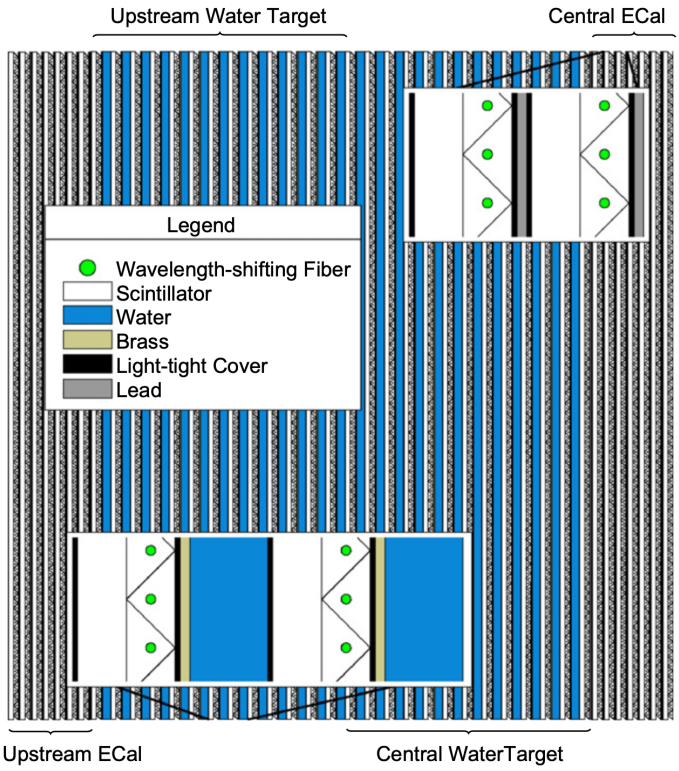

Figure 19. A cross-sectional diagram of the neutral pion detector module in ND280. This diagram was taken from Ref. [96].

Fine-grained detectors:

Two fine-grained detectors (FGDs) act as the primary target masses for neutrino interactions in ND280. The dimensions of the FGDs are designed such that the final-state leptons and light hadrons produced in CCQE interactions are likely to pass into the downstream TPCs for particle identification (PID) to be performed while retaining a sufficiently large target mass [97]. The FGD dimensions also mean that short-range particles, such as protons, generally remain contained within the sub-detector fiducial volume. The FGDs consist of modules containing perpendicular layers of polystyrene scintillator bars with square face cross sectional areas of 92.16 mm^2. Each module has 192 bars aligned in both the horizontal and vertical directions. The modules have side lengths of 186.4 cm in the x- and y-directions and a thickness of 2.02 cm. The FGDs are named as FGD1 or FGD2, with the latter of these being the most downstream along the ND280 z-axis. FGD1 has 15 of these plastic scintillator modules, while FGD2 only has seven. Instead, FGD2 has six water target modules which are hollowed polycarbonate

tubes filled with water. The different compositions in FGD1 and 2 allows for cross section interactions to be separately measured on distinct target nuclei or molecules.

Time projection chambers:

The TPCs are used to precisely reconstruct the trajectories of charged particles [98]. The momentum of a traversing particle is measured from the curvature of tracks; PID is performed by studying the rate of energy deposition per unit distance. Each TPC is comprised of two boxes of gas, the smaller of which is contained within the larger box. The larger, outermost box is filled with carbon dioxide (CO_2) gas which acts as an electrical insulator and prevents atmospheric oxygen from contaminating the inner box. The inner boxes are filled with a gas mixture comprised of argon (Ar), tetrafluoromethane (CF_4) and isobutane (iCH_4H_{10}) in a ratio of 95:3:2. Charged particles traversing through this gas mixture tend to leave ionisation tracks and produce drift electrons. The mid-point of each TPC is separated by a cathode plate which is aligned parallel to the z-axis of ND280. The electric field from the cathode has a strength of 280 V cm^{-1}; this causes ionisation electrons to drift towards the readout plane on one side of the TPC. Each readout plane consists of 12 gaseous-based MicroMegas (micro-mesh gaseous structure) detector modules, which are used to record the arrival time and electric charge of ionisation electrons. The drift and readout process allows for measurements of the electric charge and momentum of the traversing particles to be performed. A schematic of the TPC structure is shown in Fig. 20.

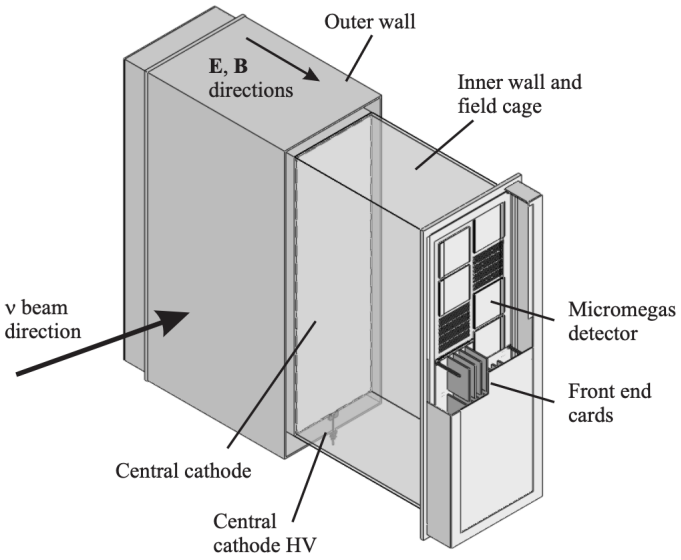

Figure 20. Cut-away diagram of the time projection chambers in ND280. This figure was reproduced from Ref. [98].

Electromagnetic calorimeters:

There are also several electromagnetic calorimeter modules at different locations in the detector [99]. The P0D is surrounded by the P0D ECal along the directions parallel to the z-axis of ND280. The P0D also has up-stream and down-stream ECals which cover the sides of the P0D in the planes orthogonal to the neutrino beam. The TPC-FGD layers are also entirely surrounded by the barrel ECal, and the down-stream ECal is located after TPC3. The ECals measure neutral particles and facilitate supplementary PID by performing track and shower separation.

3.3.2 INGRID

The interactive neutrino grid (INGRID) detector is aligned such that the neutrino beam passes through its centre; its centre is therefore on-axis with respect to the neutrino beam. INGRID measures the neutrino beam direction and intensity using an arrangement of iron scintillator modules. There are 16 identical modules in total which are aligned such they form a cross extending 10 m along the x- and y-axes with respect to the neutrino beam, which is approximately double the neutrino beam width at this location. Two of the modules are slightly offset in the y-direction to measure the asymmetry of the neutrino beam. The arrangement of INGRID modules is shown in Fig. 21.

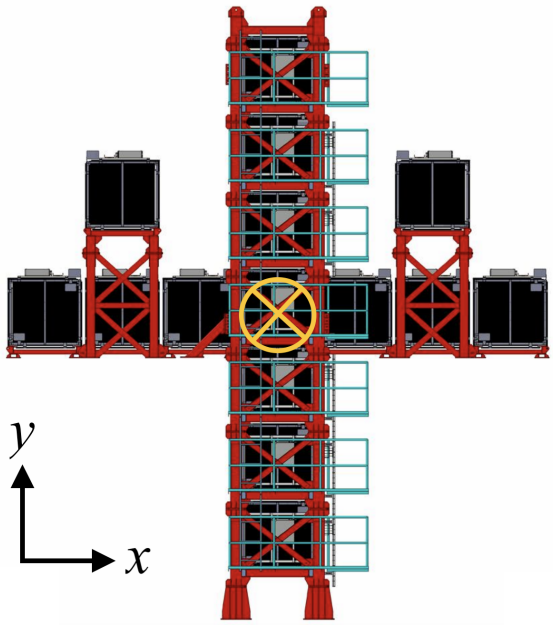

Figure 21. A graphic of the INGRID on-axis near detector. The orange circle indicates the beam centre with respect to the INGRID modules. This figure was taken and adapted from Ref. [100].

Each INGRID module is comprised of layers of iron target plates and eleven scintillator trackers. Six scintillator veto planes surround the entire module. The modules *xy* planes have area 124×124 cm^2 and the iron bars have a thickness of 6.5 cm, with total target mass of 7.1 t. The tracking planes are comprised of 22 scintillator bars with dimensions $1.0 \times 5.0 \times 120.3$ cm^3.

Furthermore, there is a dedicated proton module in the centre of INGRID which is designed to efficiently detect protons and muons produced by the neutrino beam in INGRID. This has the purpose of performing a data-MC comparison of the CCQE interaction channel. The structure of the proton module is similar to that of the other INGRID modules, except the scintillator bar dimensions are closer together, improving the tracking performance.

3.3.3 WAGASCI-BabyMIND

Some of the leading sources of systematic uncertainty are associated with the differences in target composition and angular acceptance between Super-K and ND280. A third set of near detectors which sit 1.5° off-axis are used to account for these differences. The water grid and scintillator (WAGASCI) and baby magnetised iron neutrino detector (BabyMIND) serve this purpose by acting as water and iron targets for studying neutrino interactions at a slightly less

off-axis angle. More recently, these detectors have also been used to perform neutrino cross sections on different target materials compared with those used in ND280.

3.3.4 ND280 upgrade

As of December 2023, the P0D detector has been removed and replaced with a new group of sub-detector modules. These changes in hardware constitute the ND280 upgrade [101]. The upgraded detector serves to improve the angular acceptance of ND280, as well as extending the lower threshold for hadronic energy reconstruction. It should be noted that no data from the upgraded ND280 is used in the analysis work described in this thesis, but the upgrade will eventually constitute the main off-axis near detector for Hyper-Kamiokande when constructed. The upgrade of ND280 involves the integration of several new modules as shown in Fig. 22.

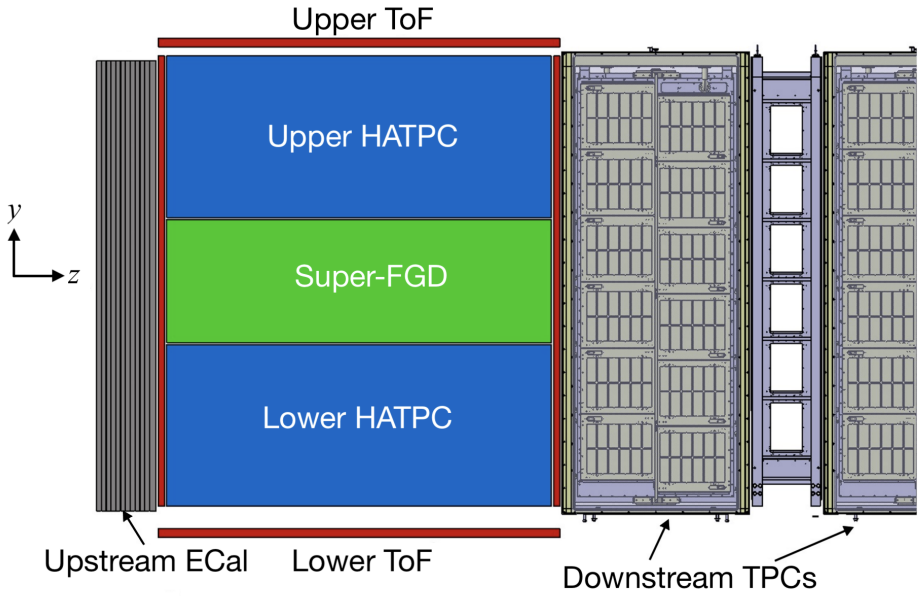

Figure 22. A diagram showing the upgraded ND280 components overlayed onto the original ND280 schematic with the pi-zero detector removed. This was reproduced from Ref. [101].

The new modules are generally constructed from similar technologies compared with the downstream modules with some upgrades. These are:

Super fine-grained detector:
A new fine-grained detector, the super-FGD, is comprised of two million $1 \times 1 \times 1$ cm^3 plastic scintillating cubes and sits at the centre of the y-axis of the original P0D position. The detector volume is $1920 \times 560 \times 1840$ mm^3 and it has a target mass of 2.2 t. Three orthogonal

wavelength shifting fibres pass through each cube and connect to micropixel avalanche MPPC photodiodes. Unlike the downstream FGDs, the super-FGD fiducial volume is fully active and is able to reconstruct final-state particle energies to within 10 MeV. The super-FGD will also facilitate PID for proton-muon and electron-photon discrimination, as well as full reconstruction of final-state particle kinematics by detecting neutrons.

High-angle time projection chamber:
The super-FGD is surrounded on the vertical axis by two high-angle time projection chambers (HATPCs). The largest plane face of each HATPC is aligned with the xz plane of ND280 which allows for the detection of charged particles which traverse into the backward phase space. The HATPC design is generally similar to the downstream TPCs. Each HATPC has a detector volume of $2.0 \times 0.8 \times 1.8$ m^3 and is also filled with the same mixture of Ar:CF_4:iCH_4H_{10} in a ratio of 95:3:2. The positioning of the HATPCs is expected to improve the efficiency for detecting particles across the high and backward angular ranges with respect to the ND280 z-axis.

Time of flight detectors:
Time of flight detectors (ToFs) are installed on the outer edges of the plane faces of the cubic structure formed by the HATPCs and super-FGD. The six ToFs planes are comprised of 20 plastic scintillating bars spanning an area of 2.2×2.4 m^2. The scintillating bars are connected to large-area silicon photo-multipliers which detect photons from traversing particles. The purpose of the ToFs is to veto particles which enter the super-FGD but do not originate from its fiducial volume.

The improvement of the detection performance of ND280 with the upgraded upstream modules has been studied extensively. Simulations suggest that the selection efficiency for muons will reach between 75% and 90% depending on the angular region. The proton detection efficiency is also expected to reach similar values with a lower detection threshold of $\sim$300 MeV.

3.4 Super-Kamiokande

The far detector of T2K is the Super-Kamiokande observatory. This is a large, underground water Cherenkov tank 295 km west of J-PARC. The tank is 41.4 m tall and 39.3 m in diameter, capable of holding 50 kT of water. This is the world's largest Cherenkov tank to date and it sits 1 km underneath Mount Ikenoyama to reduce the number of events from atmospheric sources.

A diagram of the Super-Kamiokande experiment is shown in Fig. 23.

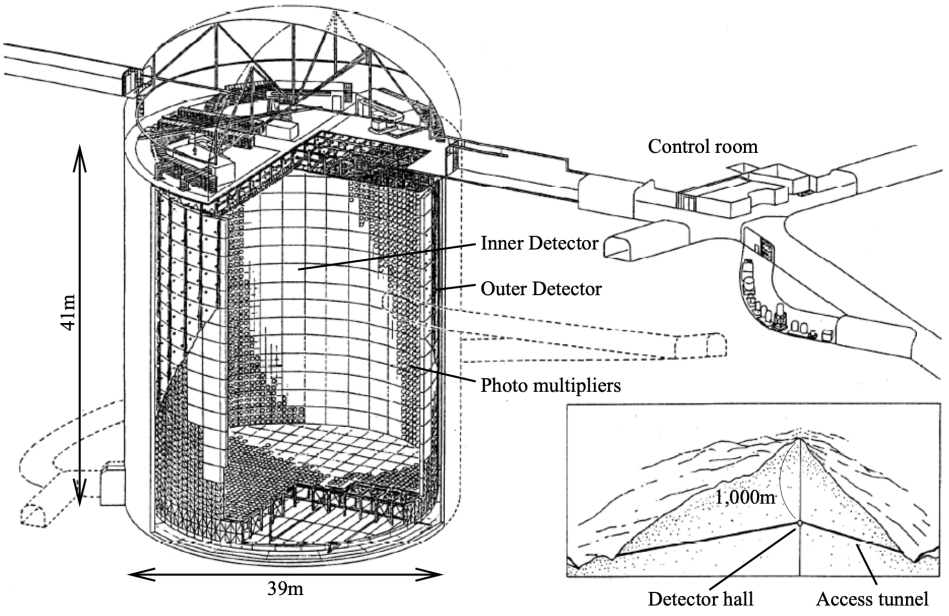

Figure 23. A diagram of the Super-Kamiokande experiment. This was taken from Ref. [102].

Super-Kamiokande is capable of measuring the $\nu_e(\bar{\nu}_e)$ appearance through detecting the Cherenkov rings produced by fast-moving electrons in water. It also measures the relative presence of $\nu_\mu(\bar{\nu}_\mu)$ through the same detection method. If a charged lepton exceeds the local speed of light of a particular medium, it will emit Cherenkov radiation in a conical pattern. The flat face of the conical Cherenkov radiation emission patterns are known as Cherenkov rings. The opening angle of a Cherenkov ring θ is related to the particle speed as a fraction of the speed of light, β, and the refractive index of pure water n,

$$\cos\theta = \frac{1}{\beta n}. \tag{54}$$

Here, $n \simeq 1.34$ and $\beta \simeq 1$, so the Cherenkov opening angle is usually around 42°.

Cherenkov rings are detected using approximately 13,000 photomultiplier tubes (PMTs) which sit on each section of the inner surface of the Cherenkov tank. The appearance of the Cherenkov rings allows for PID to be performed; a comparison of two example Cherenkov rings corresponding to a muon and an electron produced at Super-K is shown in Fig. 24. Electrons tend to produce diffuse Cherenkov rings due to more frequent scattering and showering at the relevant energies to Super-Kamiokande, whereas muons produce rings with much sharper

edges. Particle discrimination is very effective in Super-Kamiokande, with misidentification rates of electrons and muons below 1%.

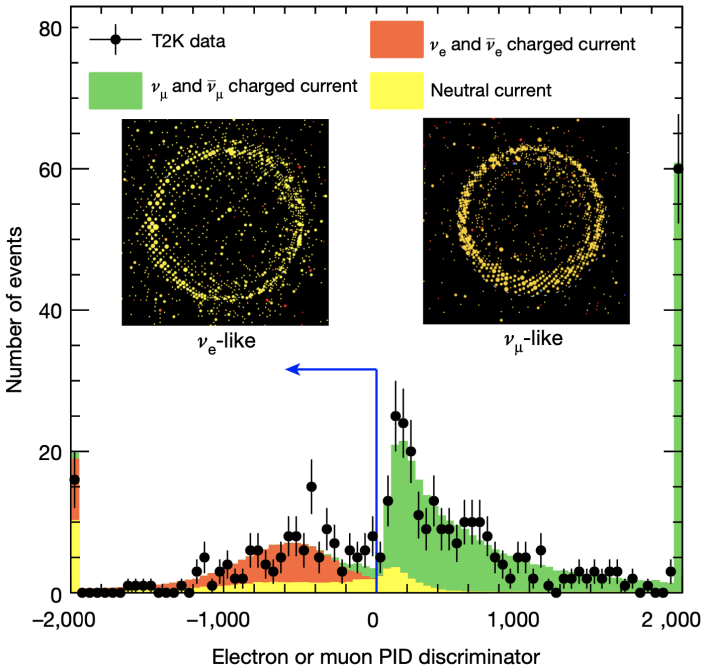

Figure 24. An example of the electron-muon particle identity discriminator variable for electron neutrino-like and muon neutrino-like events as used in Super-Kamiokande. This plot is taken from Ref. [46].

The neutrino interaction vertex position is determined from the timing of the PMTs recording the Cherenkov ring, and particle momentum is calculated from the total charge deposition. Just under 2000 of the PMTs are mounted on the outer detector (OD) which is separated from the inner detector (ID) by a stainless steel cylindrical structure. The OD PMTs are used to identify events to veto which originate from outside of the Cherenkov tank fiducial volume.

Historically, Super-Kamiokande has been filled with pure water, but recently it has been loaded with gadolinium at a 0.011% concentration, as gadolinium has a large neutron capture cross section. Loading Super-Kamiokande with gadolinium is expected to improve the signal and background discrimination capability of the detector for identifying events involving neutron production.

3.5 T2K phase-II

The T2K experiment is continuing to collect data with the upgraded near detector as part of the T2K-II phase. This is expected to bridge the gap between the present date and when Hyper-Kamiokande is operational, at which point the experiment will become Tōkai-to-Hyper-Kamiokande (T2HK).

The operating power of the T2K beam has been increased from 500 kW to 750 kW, and will eventually be raised to 1.3 MW. As of March 2024, the beam is currently functioning with a record power of 760 kW and the first neutrino events have been observed in the upgraded near detector. The top HATPC and ToF detectors are yet to be installed, but this is expected to occur by June 2024 in time for the next data-taking period. By 2030, it is projected that the upgraded ND280 will accumulate around 25×10^{21} POT while reaching a beam power of 1-1.3 MW.

The work described in subsequent chapters only uses FHC data collected by ND280 between 2010 and 2017 and therefore no data from the upgraded near detector.

CHAPTER 4

ANALYSIS STRATEGY

4.1 Introduction

The main purpose of this analysis is to measure the cross section of electron neutrino charged current pion production (ν_eCCπ^+) on a carbon target. Although a sub-dominant process, this interaction contributes to the ν_e appearance at T2K and other long-baseline neutrino experiments such as NOvA [47]. It will also remain prominent at next-generation experiments such as Hyper-Kamiokande and DUNE [49, 50]. Despite this, a cross section measurement for this particular interaction has not been performed until now.

The ν_eCCπ^+ channel is of ongoing interest within T2K as there are statistically significant data-MC discrepancies corresponding to this process in recent far detector samples [45]. Oscillation analyses at T2K measure the number of events with a single electron-like (R_e) and a delayed electron-like (d.e.) Cherenkov ring which constitute the $1R_e + 1$ d.e. sample, corresponding to ν_eCCπ^+ interactions at the far detector. The $1R_e + 1$ d.e. sample exhibits an event rate excess where 7.8 events are expected but 15 are observed as shown in Fig. 25. The p-value for this discrepancy is 1%, which could indicate an issue with the interaction models that cannot be explained by statistical fluctuations, although the latest results suggest this discrepancy may be narrowing [44]. More recent studies aimed at performing a joint fit using T2K and Super-K datasets, shown in Fig. 26, also indicate a similar excess [103].

The aim of this analysis is to perform the best possible measurement using data from ND280 to calculate the total and differential cross sections in FGD1. The results may offer some insight into whether such a discrepancy also exists at ND280, although the phase space

and backgrounds vary significantly between the near and far detectors. The analysis uses a total of 1.16×10^{21} POT, which is the total amount of FHC data collected between 2010 and 2013, as well as 2016 and 2017 during T2K runs 2, 3, 4 and 8.

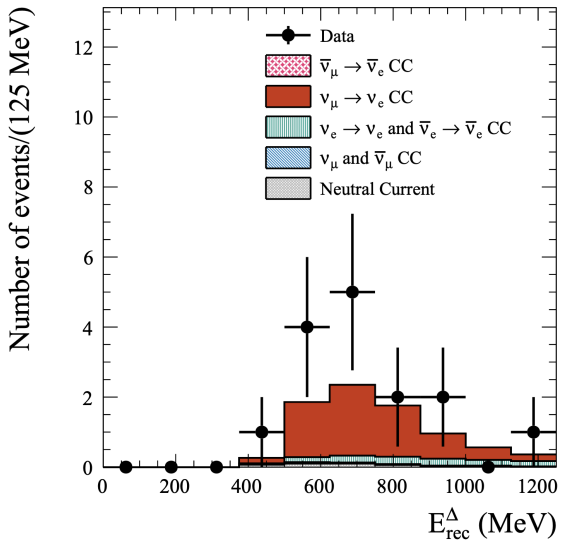

Figure 25. A distribution of the reconstructed neutrino energy assuming charged current Δ kinematics (E^{Δ}_{rec}) for the $1R_e + 1$ d.e. sample in forward horn current dataset at Super-Kamiokande. This plot is taken from Ref. [45].

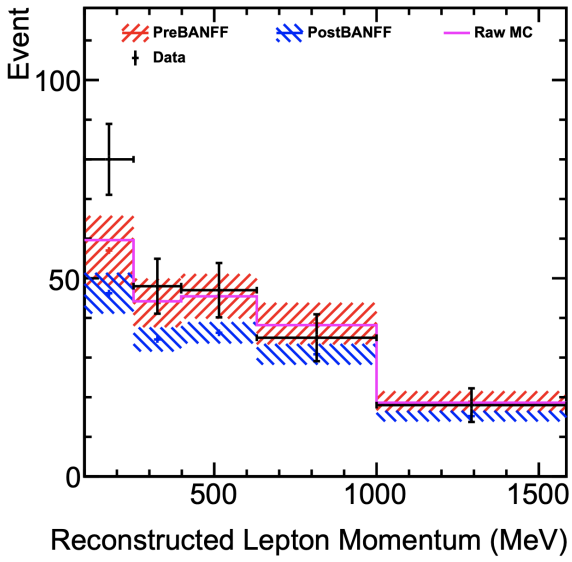

Figure 26. The reconstructed lepton momentum distribution for the $1R_e + 1$ d.e. sample in recent T2K-Super-Kamiokande joint fit studies. The blue and red error bars show the expected event rates and their uncertainties from the fit results from the beam and ND280 flux measurement task force in Ref. [103].

4.2 Definitions

4.2.1 Cross section measurement

The main results reported for this analysis are the unfolded single differential cross section as a function of electron momentum, pion momentum and electron angle,

$$\frac{d\sigma}{dp_e}, \quad \frac{d\sigma}{dp_\pi} \quad \text{and} \quad \frac{d\sigma}{d\cos\theta_e}, \tag{55}$$

as well as the total flux-integrated cross section, σ. The differential cross section $d\sigma$ with respect to any of the three input observables x in true kinematics bin i is calculated using

$$\left(\frac{d\sigma}{dx}\right)_i = \frac{\hat{N}_i^{\text{sig}}}{\varepsilon_i \Phi N_T} \frac{1}{\Delta x_i}. \tag{56}$$

In this expression, the i^{th} bin has a selection efficiency ε_i, a number of signal events $\hat{N}_i^{\text{sig}}$ and a width Δx_i. The remaining terms, N_T and Φ, are the number of target nucleons in the fiducial volume and integrated flux respectively.

To obtain these cross section results, the three-dimensional cross section is calculated as a function of truth space kinematics bins as described later in section 7. The cross section is not projected along the pion angular distribution because the low event rates in the original four-dimensional binning led to unresolvable instabilities associated with the minimisation process. The relatively flat selection efficiency along $\cos\theta_\pi$ (shown later in Fig. 55) and reconstruction limitations led to this variable being selected for omission.

The values for $\hat{N}^{\text{sig}}$ in each true kinematics bin are obtained through the event selection procedure described in section 5. The best-fit values for Φ and ε are also calculated during the fitting process outlined in section 7. The value for N_T in FGD1 is calculated from the mass and composition of this sub-module; this gives $N_T = (5.54 \pm 0.04) \times 10^{29}$ nucleons from a total target mass of 919.5 kg [85].

4.2.2 Signal definition

The interaction being studied in this analysis is any charged current process caused by an electron neutrino which results in the production of at least one positively charged pion,

$$\nu_e + \mathrm{CH} \rightarrow e^- + \pi^+ + X. \tag{57}$$

The combination of additional final-state hadrons, X, is arbitrary and may or may not include any number of additional positively charged pions. The interaction must occur within the FGD1 sub-detector, which contains a number of different nucleon targets and can be approximated as a hydrocarbon (CH) target; no restrictions are imposed on the type of target nucleon.

The signal definition is comprised of two statements:

I. Any charged current process which produces an electron as the primary outgoing lepton.

II. At least one positively charged pion is also produced from the same vertex.

The main neutrino interaction vertex position in FGD1 must be within the fiducial volume (FV): $|\vec{x}| < 874.51$ mm, $|\vec{y} - 55| < 874.51$ mm, $136.875 < |\vec{z}| < 446.995$ mm. These positional constraints are imposed such that the outermost five scintillator bars in FGD1 on either side along the x- and y-directions are omitted. This restriction reduces a large amount of out-of FGD (OOFGD) events which tend to be mis-reconstructed on the edge of FGD1.

The cross section measurements are only reported in the following regions of the true particle kinematics phase space:

$$0.35 < p_e < 30\ \mathrm{GeV}/c, \quad 0.7 < \cos\theta_e < 1.0, \quad p_\pi < 1.5\ \mathrm{GeV}/c. \tag{58}$$

The phase space constrains have several purposes. Most importantly, they omit the background-dominated regions and ensures the selection efficiency is reasonably high and consistent across each bin. The out-of phase space (OOPS) regions are passed through the fitting and cross section extraction processes but the bins corresponding to these omitted regions are not used for calculating the differential and total cross sections.

The values of the electron kinematic constraints were optimised by studying the efficiency and purity of the selected events projected onto phase space plots of the true electron momentum and angle. The upper limit on the pion momentum was implemented to remove events where the pion PID performance worsens for discriminating between pions and protons

which occurs more prominently above 1.5 GeV/c. The optimisation of the phase space constraints is performed using the kinematics phase space plots shown sections 5.2.1 and 5.3.3.

4.2.3 Background definitions

The background events which are most likely to pass the event selection process are also defined. A significant proportion of ν_e interactions do not result in pion production; any which produce exactly zero pions of any charge are defined as ν_eCC0π. The remaining ν_e interactions which do not fall into ν_eCCπ^+ or ν_eCC0π are defined as ν_eCC-other.

Photons tend to undergo pair production within the detector modules, creating electron-positron pairs where the electron is capable of passing the main electron track PID. Any photon interaction with a pair production vertex located within the FGD1 FV is defined as the photon background. Photon interactions are further distinguished by the origin of the photon parent particle. Photons which originate from ν_μ charged and neutral current π^0 production in the FGD1 FV are defined as ν_μCC-γ and NC-γ respectively. The remaining photon interactions are categorised based on whether the interaction vertex occurs in FGD1 but outside of the FV defined in section 4.2.2, or outside of FGD1; these are OOFGDFV-γ and OOFGD-γ respectively. Any remaining pair production events not covered by these four categories are labelled as other γ.

Muons are also capable of being misidentified as electrons due to the limitations of the sub-detectors. Events which have a muon misidentified as the leading lepton track are defined as the μ background. All events originating outside of FGD1 with a mis-reconstructed vertex in FGD1 are defined as part of the other background. Any further events not covered by the definitions so far are also defined as other background events.

These event categories constitute the main event type categorisation used in plots in successive sections. Several other event categorisations are also used which distinguish ν_e and ν_μ events into the interaction type, such as CCQE, RES and DIS. A further categorisation is also used which distinguishes photon events by the number of neutral pions produced and whether the photon originates from a CC or NC interaction; this is particularly useful for comparing the photon events which enter the signal and control samples.

4.2.4 Samples

Two signal-enriched samples are used in this analysis. These are distinguished by the method for detecting the pion produced at the $\nu_e \mathrm{CC}\pi^+$ vertex:

(a) TPC sample - the pion enters the TPCs downstream from FGD1; detection is performed by analysing energy deposition trends in the TPC and ECal sub-detectors.

(b) FGD sample - the pion remains in FGD1 and decays to a muon and then a Michel electron; detection involves tagging these electrons using FGD time bin hits.

Examples of tracks left by events which satisfy the signal definition for each sample are superimposed on the ND280 geometry in Fig. 27.

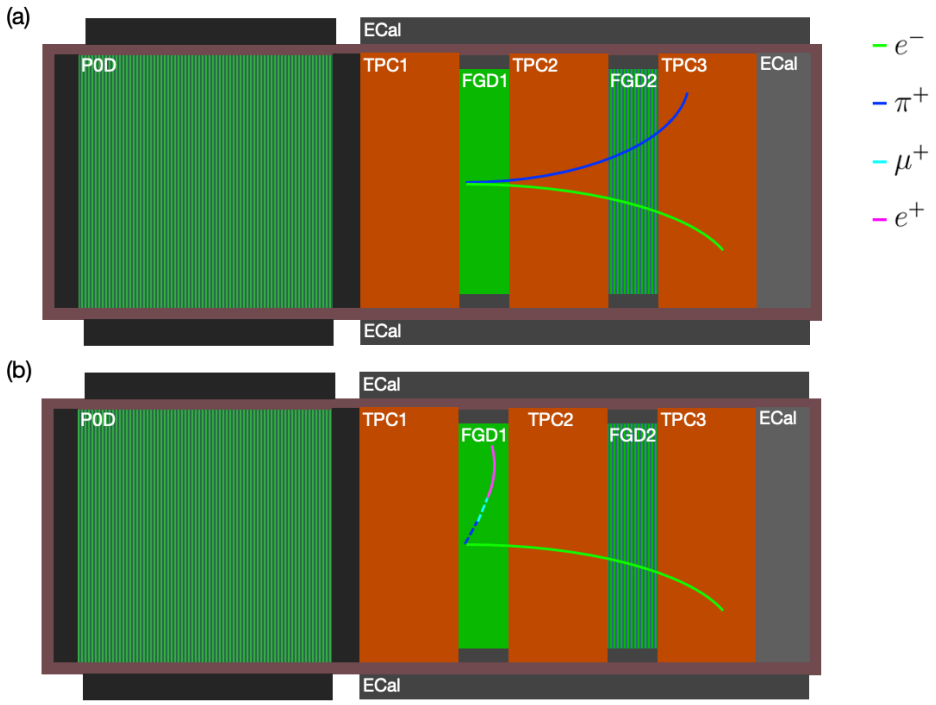

Figure 27. Schematics of the ND280 detector showing examples of typical signal events that would pass into (a) the TPC sample or (b) the FGD sample. The dotted tracks represent the intermediate particles which form the decay chain to the Michel electron ($\pi^+ \to \mu^+ \to e^+$). The legend indicates the particle species corresponding to each example track.

Two control samples are also used to constrain the main photon backgrounds which appear in the signal-enriched samples. These photons primarily originate from $\nu_\mu \mathrm{CC}\pi^0$ and $\mathrm{NC}\pi^0$ interactions where the neutral pion decays by $\pi^0 \to \gamma\gamma$. These photons can then undergo pair

production and create electron-positron pairs. The generated positrons and final-state nucleons are capable of passing the pion PID, while the electrons are likely to pass the main track electron PID. The control samples for this analysis aim to select photon events which are likely to be accidentally identified by the main pion PID methods.

A third type of signal sample involving pions which remain in FGD1 but do not decay to Michel electrons was also considered. However, this was not implemented after a prototype sample suggested that only five events over the entire available MC would enter this sample before any background-reducing cuts were implemented.

4.3 Truth studies

4.3.1 Sensitivity studies

As part of an initial sensitivity study, an event categorisation was created to distinguish between $\nu_e \mathrm{CC}\pi^+$ events based on whether the pion traverses from FGD1 into TPC2, or remains in FGD1. This was to estimate an upper limit on the number of signal events each signal-enriched sample could observe, as well as to determine the true pion momentum and neutrino energy distributions of signal events for each sample. These variables are shown for true signal events with no selection cuts applied in Fig. 28.

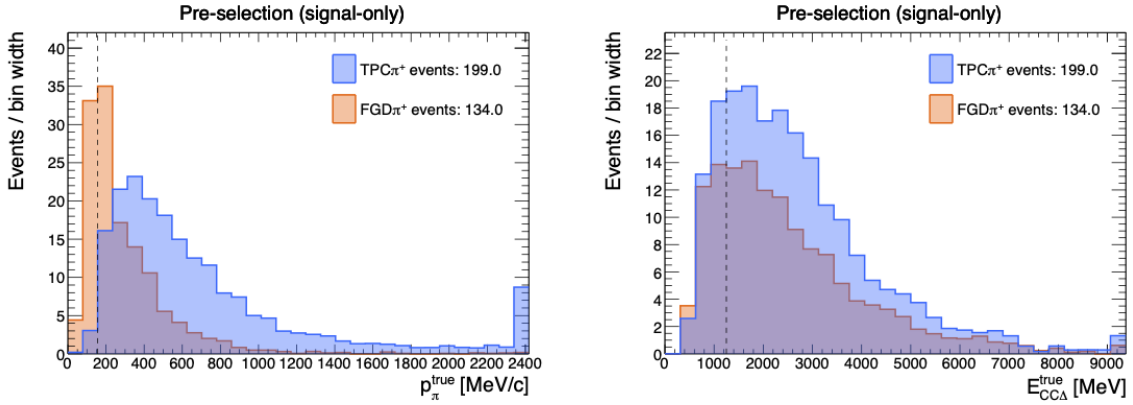

Figure 28. Distributions of the true pion momentum, p_π, and true neutrino energy assuming charged current Δ kinematics, $E^{\Delta}_{\mathrm{rec}}$, for all $\nu_e \mathrm{CC}\pi^+$ signal events without any selection cuts applied. The categories distinguish between pions which stay in FGD1 or pass from FGD1 into TPC2. The regions left of the black dashed lines indicate the phase spaces relevant to the Super-K far detector. These boundaries are $p_\pi < 0.156$ GeV$/c$ and $E^{\Delta}_{\mathrm{rec}} < 1.25$ GeV.

These distributions show that pions from true signal events enter the downstream TPCs and

remain in FGD1 at a ratio of approximately 3 : 2. There are a total of 199 and 134 events which would qualify for the TPC and FGD samples respectively assuming perfect reconstruction and detection. Moreover, pions which remain in FGD1 contribute significantly more to the Super-K true pion momentum phase space than those which enter the TPCs. Only 3.2 signal events with $p_\pi < 0.156\ \mathrm{GeV}/c$ have pions which traverse into the downstream TPCs, while 37.5 under the same momentum constraint have pions which remain in FGD1. The inclusion of FGD-contained signal events is therefore essential to make a comparison with the Super-K event rate. Approximately 30 events from each category contribute to below the energy threshold of Super-K. Given the comparable overall number of events and the relative contributions of the FGD-contained events to each true distribution, the two signal samples as listed in section 4.2.4 were defined as the main samples for this analysis.

The main difference between the two signal-enriched samples is the method of pion detection. The FGD and TPC sub-detectors have significant design variations which employ distinct methods for pion PID and kinematic variable reconstruction. Both signal samples use the same method for electron PID as electrons are required to enter TPC1 with a minimum number of hits.

4.3.2 Pion kinematics reconstruction from Michel electrons

Pions which remain in FGD1 tend to have very short, unreconstructable tracks; the same track reconstruction techniques as performed for pions which enter the TPCs are not possible for FGD-contained pions. Additionally, these pions tend to decay to Michel electrons (e^+) through the following consecutive interactions:

$$\begin{aligned} \pi^+ &\rightarrow \mu^+ + \nu_\mu, \\ \mu^+ &\rightarrow e^+ + \nu_e + \bar{\nu}_\mu. \end{aligned} \tag{59}$$

The momentum and angle of the pion are approximated using the position of the Michel electron production vertex as measured in FGD1. This technique was first developed for a cross section analysis of ν_μCC1π^+ interactions in FGDs 1 and 2 [104]. The reconstruction of particularly low momentum pions is essential for a far detector comparison; this also greatly enhances cross section sensitivity for this region of the pion kinematics phase space which has not been extensively studied so far. A diagram showing Michel electron production from ν_eCCπ^+ events in FGD1 is shown in Fig. 29 and the key tracks and quantities related to this reconstruction method are indicated.

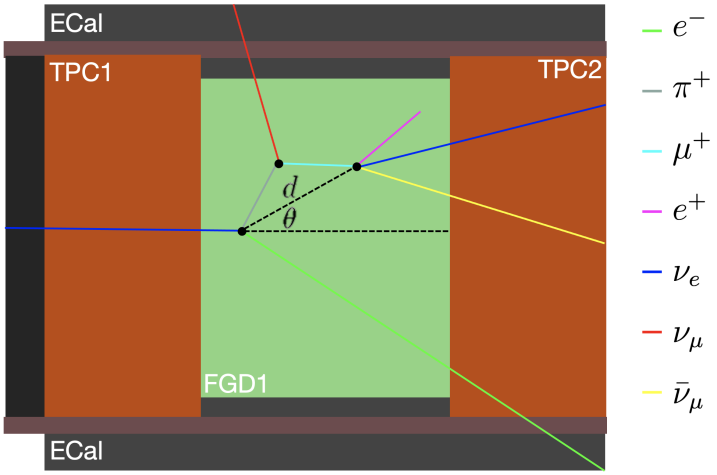

Figure 29. Schematic of Michel electron (e^+) production from ν_eCCπ^+ events superimposed on a subsection of the ND280 geometry. The quantities d and θ are the distance and angle between the Michel electron vertex and the original ν_eCCπ^+ vertex respectively. The legend indicates the particle species corresponding to each track. The track lengths of the pion and muon are exaggerated to clearly indicate the origin of d and θ.

The quantity d is the distance between the ν_eCCπ^+ and $\mu^+ \to e^+ + \nu_e + \bar{\nu}_\mu$ interaction vertices. The angle θ is the angle between the parent ν_e direction, which is approximated as the neutrino beam direction, and the Michel electron direction. In this approximation, the pion angle is assumed to be equivalent to the Michel electron angle and the pion momentum is correlated to the Michel electron distance using a parametrisation. The momentum and angular variables are therefore approximated by the functions

$$p_\pi = c_0 \times d^{c_1} + c_2, \qquad \theta_\pi = \theta_{\mathrm{ME}}. \tag{60}$$

where the constants have values $c_0 = 19.11 \pm 0.8$ [MeV/mm], $c_1 = 0.4154 \pm 0.0063$ and $c_2 = 14.47 \pm 2.02$ MeV which are extracted from fitting this function to MC and data. The values extracted agree with those originally measured for FGD1 as part of the ν_μCCπ^+ analysis [104]. Truth-level comparisons of the pion momentum and angle with the Michel electron distance and angle are shown in Fig. 30.

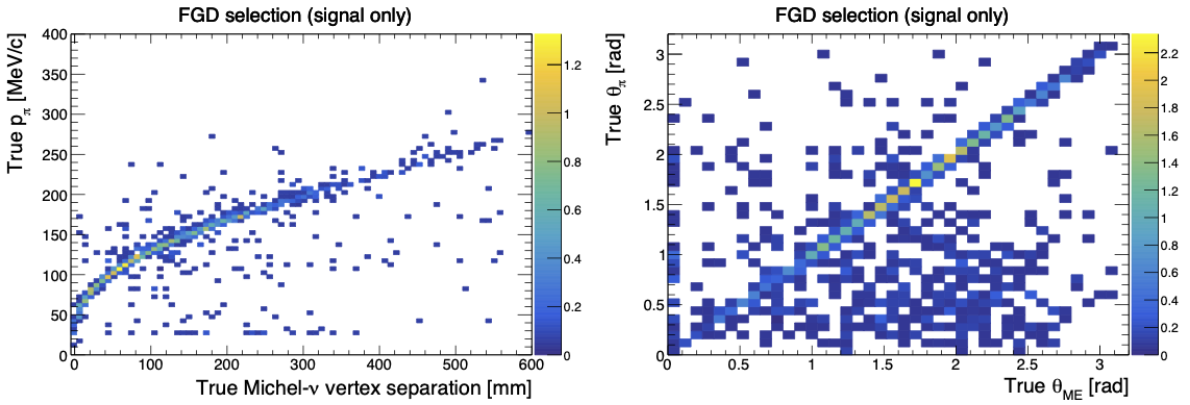

Figure 30. Two-dimensional histograms of the true separation distance between the neutrino vertex and Michel electron vertex d and the true pion momentum p_π^{true} (left), and of the true Michel electron angle $\theta_{\text{ME}}^{\text{true}}$ against the true pion angle θ_π^{true} (right). The z-axis measures the MC event rate per bin.

There are clear trends in both truth-level comparison plots. Discussion of the effectiveness and reconstruction performance utilising these comparisons are presented later in section 5.3.2. This method gives unique access to pion kinematics information at particularly low momentum ranges which have previously been inaccessible. The performance of this reconstruction method has some limitations which are discussed in chapter 5.3. A unique systematic uncertainty is also assigned to this method of momentum reconstruction; this is detailed in section 6.1.

Although the truth-level comparisons are clear, this method is reliant on accurately reconstructing the positions of Michel electrons in FGD1. Hits in FGD1 are recorded with an x- or y-coordinate at each layer as well as the z-coordinate which is extrapolated from the layer at which the FGD hit occurs. To improve the likelihood of accurately reconstructing an electron track, the start of the track requires consecutive hits along the x and y planes of adjacent layers. The reliability of momentum reconstruction is also limited as above $\sim 250\,\text{MeV}/c$, the number of events which enter the truth-level comparison substantially decreases.

CHAPTER 5

EVENT SELECTION

The event selection process attempts to produce samples which maximise the relative presence of $\nu_e \mathrm{CC}\pi^+$ events using the ND280 dataset. This is achieved using a chain of selection cuts which aim to remove background events using the reconstructed observables and functions of these observables measured by the sub-detectors. The event selection was adapted from a published measurement for the inclusive cross section of $\overset{(-)}{\nu}_e\mathrm{CC}$ interactions [85].

Quantitative measures of the selection performance and individual selection cuts are the *efficiency*, ε and *purity*, ρ. These are defined as

$$\varepsilon = \frac{S_{\mathrm{sel}}}{S_{\mathrm{tot}}} \quad \text{and} \quad \rho = \frac{S_{\mathrm{sel}}}{S_{\mathrm{sel}} + B_{\mathrm{sel}}}, \tag{61}$$

where S and B are the number of true MC selected signal and background events respectively; the subscript indicates whether this is the number of events in total (tot) with no selection cuts applied, or the number which pass the event selection (sel). It is also useful to study the changes in efficiency and purity, $\Delta\varepsilon$ and $\Delta\rho$ for each selection cut to determine whether it is beneficial to the full selection. Plots which indicate the overall effects of each cut on $\Delta\varepsilon$ and $\Delta\rho$ are referred to as *N minus one plots* $(N-1)$. A list of the shared selection cuts used by all samples is shown in table III. Another list of the specific selection cuts which separately appear in each sample is shown in table IV. The shared and sample-specific cuts are then described in detail in sections 5.1. The selection outputs are presented in sections 5.2.1 and 5.2.2, while a performance assessment is shown in section 5.3.

Cut	All samples
0	ND280 event quality
1	Track multiplicity
2	TPC quality
3	Main track electron PID
4	Main track muon PID
5	Main track pion PID
6	Main track muon PID (2nd seg)
7	ECal EM energy cut
8	MIP-EM cut
9	P0D veto
10	TPC veto

Table III. A table of the shared event selection cuts common between all samples. The cut number indicates the order in which these are applied. The purpose and implementation of each selection cut is described in sections 5.1.1-5.1.3.

Cut	TPC sample	FGD sample	TPC sideband	FGD sideband
11	Pair track pion PID	Michel electron cut	Pair track pion PID	Michel electron cut
12	ECal polar angle veto	ECal upstream veto	ECal upstream veto	Reverse m_{inv} cut
13	m_{inv} cut	m_{inv} cut	Reverse m_{inv} cut	-
14	-	-	External FGD veto	-

Table IV. A table of the sample-specific selection cuts. The cut number indicates the order in which these are applied. The purpose and implementation of each selection cut is described in sections 5.1.4-5.1.7.

5.1 Selection cuts

5.1.1 Event quality and track multiplicity

All samples share the same initial set of selection cuts to find good quality tracks in FGD1 and TPC2, as well as skipping bunches which have no tracks. These cuts reduce the output file size and hasten the analysis run-time with minimal loss of signal events. The quality and multiplicity cuts are:

0. **ND280 event quality:**
   Events are passed through a data quality check which confirms that the relevant ND280 sub-detector has good data quality and beam spill.

1. **Track multiplicity:**
   Events are passed if they have at least one reconstructed track starting in the FGD1 FV. Each track is also categorised as either positively or negatively charged.

2. **TPC quality:**
   The most energetic negatively charged track starting in FGD1 is required to have at least 36 TPC hits, or 18 hits if the track has an ECal segment. This is the *leading track* which is considered as an electron candidate.

5.1.2 Particle identification

The energy deposition as a function of particle momentum is used to discriminate between electrons, muons, pions and protons. The expected energy loss of a particle with a particular momentum can be compared with the measured energy loss. A residual is defined such that the measured and expected energy loss in the TPC for the i^{th} particle hypothesis, C_T^i, satisfy

$$\delta_i = \frac{C^i_{T,\text{meas}} - C^i_{T,\text{exp}}}{\sigma^i_{\text{exp}}}, \tag{62}$$

where σ^i_{exp} is the resolution of the energy deposition distribution. The terms δ_i for a particular particle species are referred to as the *pull* variables.

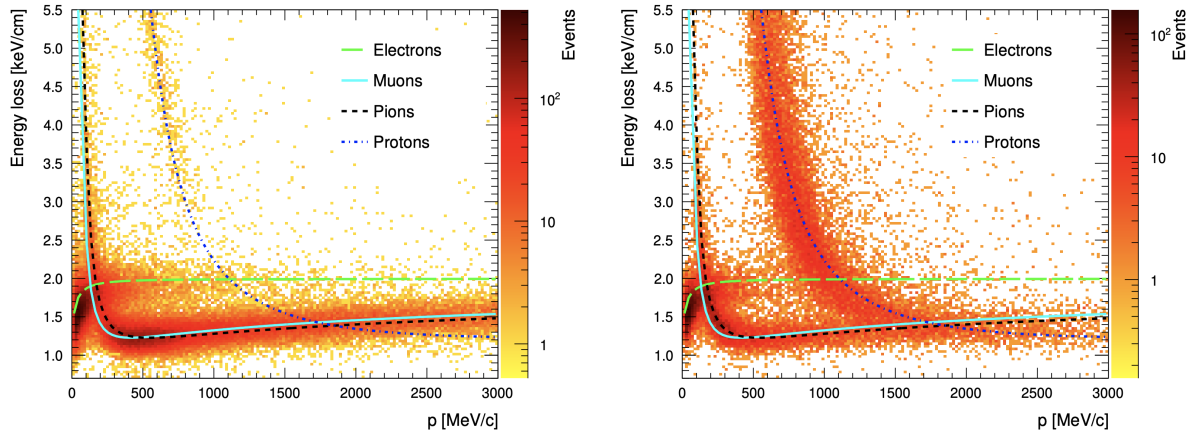

Figure 31. Measurements and fits of the mean ionisation as a function of particle momentum in the TPCs for electron, muon, pion and proton tracks starting in FGD1. This shows the trends for negatively charged tracks (left) and positively charged tracks (right). These plots were taken from Ref. [85].

Leading tracks are subject to the following PID cuts based on these pull variables:

3-5. TPC2 PID:

Selection cuts on the pull variables, $\delta_{e,\mu,\pi}$ defined in Eq. (62) are imposed for electron, muon and pion particle hypotheses. Events are passed if the pulls satisfy all of the following

$$\begin{aligned} -1.5 &< \delta_e < 2.5, \\ -2.5 &> \delta_\mu, \;\; \delta_\mu > 3.0, \\ -2.5 &> \delta_\pi, \;\; \delta_\pi > 3.0. \end{aligned} \tag{63}$$

If the leading track has $p > 300$ MeV$/c$ and enters the ECal, a relaxed electron PID cut is used, requiring

$$-2.0 < \delta_e < 2.5. \tag{64}$$

6. TPC3 PID:

Leading tracks which enter TPC3 with greater than 18 hits are subject to another PID cut, which requires

$$-2.0 > \delta_\mu, \;\; \delta_\mu > 1.5. \tag{65}$$

PID is also performed using information from the ECals to discriminate between electrons and muons as the leading lepton track candidate. The ECals reconstruct the EM energy assuming the deposited energy originates from an EM shower. The geometric variables of ECal clusters, such as the circularity and charge distribution, are used to produce a probability distribution function for each particle species. A log-likelihood variable $R_{\text{MIP/EM}}$ is defined to discriminate between EM showers caused by electrons and minimally-ionising particles (MIPs) such as muons [105].

7-8. ECal PID:

If the leading track is not fully contained or has $p < 800$ MeV$/c$, it must pass an ECal MIP-shower PID cut by requiring $R_{\text{MIP/EM}} > 0$. If the leading track has $p > 800$ MeV$/c$ and is fully contained in the ECal, it must deposit a total energy greater than 1000 MeV to pass PID.

Histograms showing the effect of the TPC and ECal PID on the overall selection outputs are shown in $N-1$ distributions in Figs. 32 and 33.

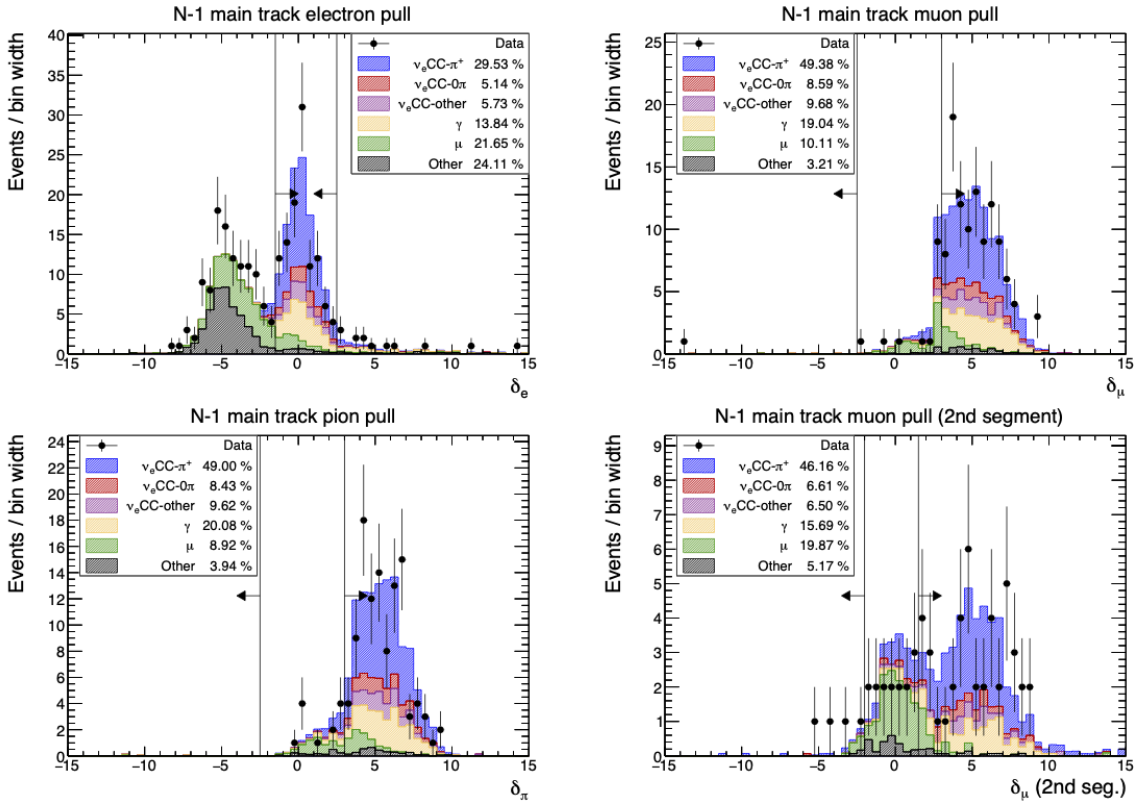

Figure 32. Distributions of the electron, pion and muon pull variables of leading tracks which enter the TPCs downstream of FGD1. The lower right distribution shows the muon pull for tracks which enter TPC3, while the other three show the pulls for tracks which only enter TPC2. The arrows indicate the events which pass the selection cut.

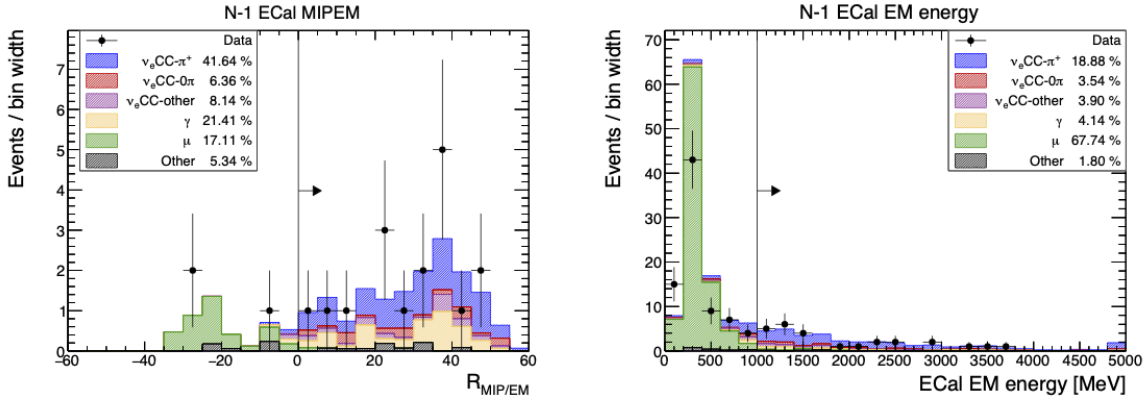

Figure 33. Distributions of the ECal $R_{\mathrm{MIP/EM}}$ values of leading tracks with $p < 800$ MeV/c (left), and the ECal EM energy of leading tracks which enter the ECal and have $p > 800$ MeV/c (right). The arrows indicate the events which pass the selection cut.

5.1.3 Upstream photon vetoes

All samples are also subject to a pair of vetoes which are designed to remove photon events by vetoing tracks which originate from upstream sub-detectors. These vetoes have a small effect on the signal-enriched samples, but they reduce the undesired OOFGD and OOFGDFV photons from the control samples. A source of systematic uncertainty is introduced when these cuts accidentally veto a signal event. Including these cuts in the signal sample selections also simplifies the pile-up count and evaluating this systematic uncertainty. The photon vetoes are:

9. **P0D veto:**
   Events with tracks which originate from the P0D FV are removed.

10. **TPC veto:**
    The most energetic track in the TPC which is not the electron candidate track is selected. The event is vetoed if this selected track has a starting z-coordinate (z_{min}) more than 100 mm upstream of z-coordinate of the main track start position, z_{main},

$$\Delta z = z_{\text{main}} - z_{\text{min}} > -100 \text{ mm}. \tag{66}$$

After the photon vetoes are applied, the selection splits into four branches corresponding to the two signal and two control samples.

5.1.4 TPC sample cuts

The selection cuts used for the TPC signal sample are:

11. **Pion cut:**
    The highest momentum, positively charged track which starts within 40 mm of the leading track is considered as a pion candidate. Pion candidate tracks are required to enter TPC2 and are subject to a pion PID cut, which requires the pion candidates to have

$$-4.0 < \delta_{\pi} < 4.0. \tag{67}$$

    Events are vetoed if there are no pion candidate tracks. However, if there is a successful Michel electron tag, then the event is passed through the FGD sample cuts as described in section 5.1.5. The effect of the PID cut on the TPC signal-enriched sample is shown in Fig. 34.

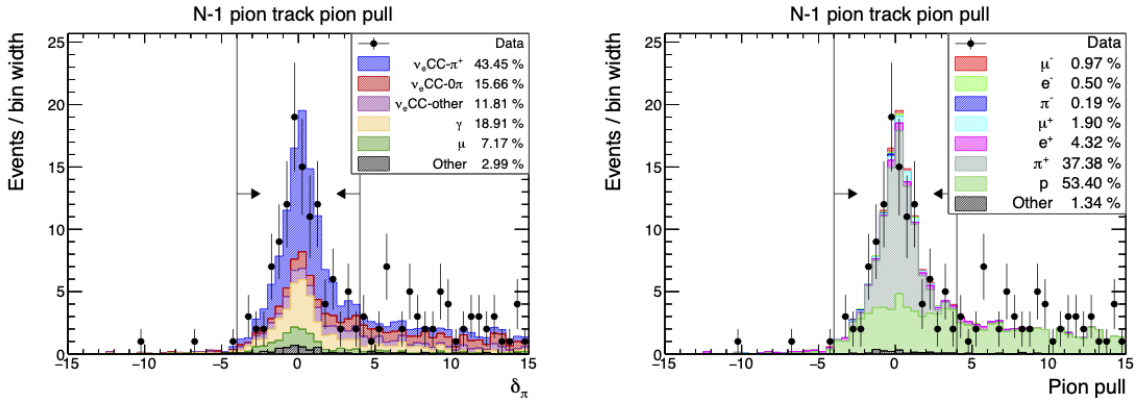

Figure 34. Distributions of the pion pull of pion candidate tracks in the standard event categorisation (left) and the true pion candidate particle categorisation (right). The arrows indicate the accepted events.

12. ECal polar angle veto:

Reconstructed track segments in the same bunch as an electron candidate which enter the tracker ECal are searched for and labelled as ECal tracks. If the leading track has $p < 1000$ MeV$/c$, then ECal track is subject to an angular veto. The polar angle θ_z is the angle between the vector, which connects the start positions of the leading track and ECal track, and the z-axis of ND280. The event is vetoed if

$$\cos\theta_z < 0.6. \tag{68}$$

The vector and θ_z are indicated on example events with a leading track and ECal track in Fig. 35

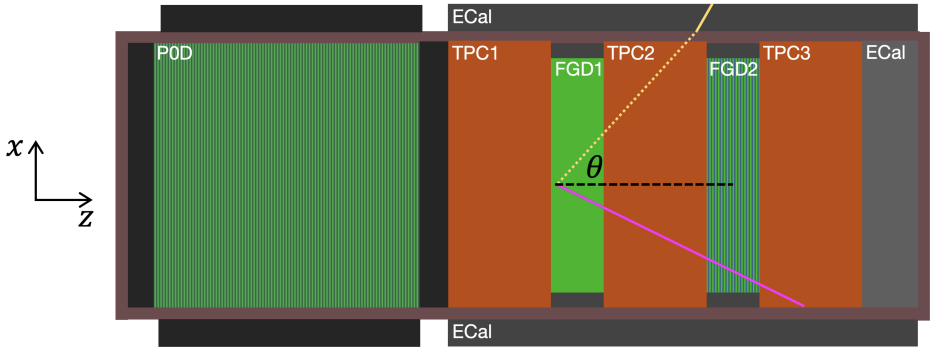

Figure 35. Schematic of the ECal polar angle θ_z on the ND280 geometry. The main electron candidate track (pink) and a track with ECal activity (yellow) are indicated and the dashed black line is parallel with the z-axis of ND280.

.

The effect of this selection cut on the TPC sample is shown in Fig. 36

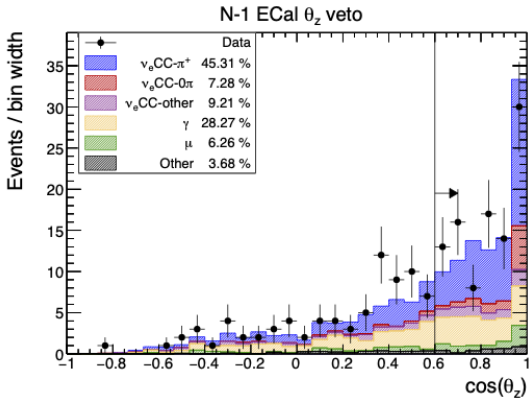

Figure 36. Distributions of the cosine of the ECal polar angle θ_z for events with an electron candidate and an additional track with ECal activity. The arrows indicate events which are passed.

13. Invariant mass cut:

The leading and pion candidate tracks have their invariant mass calculated using their reconstructed momentum and energy, $\vec{p}_{1,2}$ and $E_{1,2}$. The invariant mass, m_{inv}, is calculated assuming the pion candidate is actually a positron,

$$m_{\text{inv}} = \sqrt{2m_e^2 + 2\left(E_1 E_2 - \vec{p}_1 \cdot \vec{p}_2\right)}, \tag{69}$$

where $m_e = 0.511$ MeV$/c^2$ is the mass of an electron. If $m_{\text{inv}} > 110$ MeV$/c^2$, then the event is passed. This removes pair production events where the positron accidentally passes pion PID and therefore reduces the photon background. The effect of this cut on the TPC sample is shown in Fig. 37.

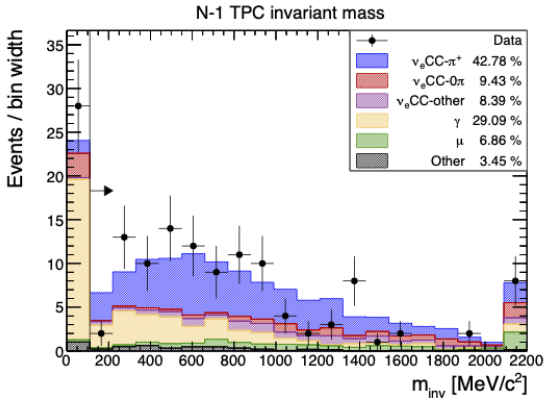

Figure 37. A distribution of the invariant mass, m_{inv}, of the leading and pion candidate tracks for the TPC signal sample. The arrow indicates the accepted events.

Furthermore, events which pass all FGD sample cuts are vetoed from entering TPC sample, making the two selections mutually exclusive. This was because a small number of events passed both selections in the case that the TPC sample had a misidentified proton as the pion track, and there was also a successful Michel electron tag for another pion from the same interaction.

5.1.5 FGD sample cuts

In section 4.3.2, it was explained that pions which remain in FGD1 tend to decay to Michel electrons through the consecutive interactions,

$$\pi^+ \to \mu^+ + \nu_\mu \quad \text{and} \quad \mu^+ \to e^+ + \nu_e + \bar{\nu}_\mu . \tag{70}$$

For these decays, the mass difference between muons and electrons is 105.2 MeV$/c^2$, while the mass difference between muons and pions is 33.9 MeV$/c^2$. As a result, the Michel electrons produced in the secondary interaction have far higher kinetic energy than the muons produced in the first. The muons will therefore not traverse far through the FGD1 before decaying, while the Michel electrons are more likely to and will leave more hits across FGD1. This means Michel electrons tend to leave a number of delayed and clustered FGD hits accompanied by an accumulation of electric charge. Michel electrons are identified by studying these FGD hits over a particular time period. Truth studies shown previously in section 4.3.1 suggest that around 40% of pions from signal events are likely to decay to Michel electrons in FGD1.

Events in the FGD sub-detectors are binned by the time difference between consecutive hits occurring within a cluster of hits. If two consecutive hits occur within 100 ns of each other, they are put into the same time bin. If any two consecutive hits in the cluster have a time difference greater than 100 ns, then a new time bin is initialised and the second hit is placed in this time bin. Muon lifetimes are typically around 2200 ns, which means Michel electrons can be identified by the production of additional, delayed time bins. Events in FGD1 are considered Michel electron candidates if they leave at least seven hits in the delayed time bin. The number of hits is used as a discriminator between Michel electrons and other particles as shown in Fig. 38.

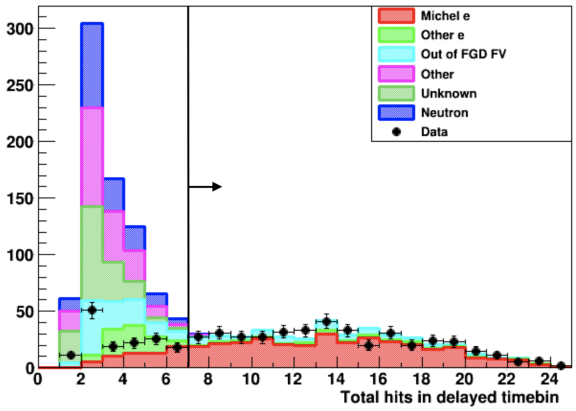

Figure 38. A distribution of the number of delayed time-bin hits, categorised by the type of particle causing the hits for FGD1. This was not produced using the selection outputs and was instead taken from Ref. [106]. Note the data-MC discrepancy below the cut threshold is not fully understood. The 'unknown' category refers to cases where the truth information was not saved which tends to be the case for low energy neutral particles.

The list of cuts used for the FGD signal sample is:

11. **Michel electron cut:**
    Events are tagged and passed if they contain delayed clusters with at least seven delayed time bin hits in FGD1. This identifies events in which a Michel electron is likely to have been produced from a pion decaying to a muon.

12. **Upstream ECal veto:**
    The start position of the most upstream ECal cluster is compared with the start position of the electron candidate track. The event with ECal activity is rejected if the ECal cluster starts greater than 100 mm upstream of the electron track start position.

13. **Invariant mass cut:**
    The same invariant mass cut as described in section 5.1.4 is applied. However, as this sample has no pion candidate, a positron candidate track is identified by searching for positively charged tracks which pass an electron PID cut and originate within 40 mm of the leading track. If multiple positively charged tracks are found within 40 mm, then the track which calculates the lowest invariant mass is selected as this is more likely to be a photon conversion event. The invariant mass of the leading track and the pair track is calculated as before using Eq. (69). If no positron candidate is found, the event is passed. The cut similarly requires $m_{\text{inv}} > 110$ MeV$/c^2$. The effect of this selection cut on the FGD sample is shown in Fig. 39.

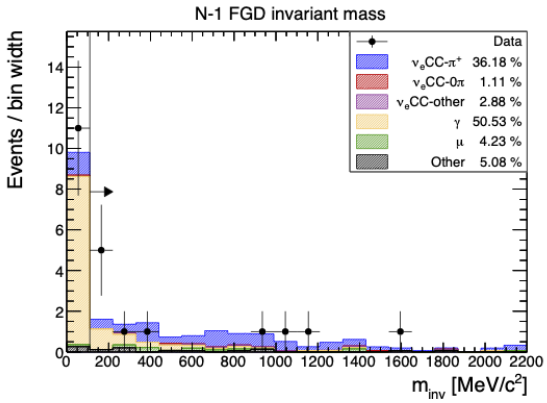

Figure 39. A distribution of the invariant mass, m_{inv}, of the leading and pair candidate tracks for the FGD signal sample. The arrow indicates the accepted events.

5.1.6 TPC control sample cuts

The selection cuts used for the TPC control sample are:

11. Pion cut:

The same pion PID (cut 11) described in section 5.1.4 is applied.

12. Reverse invariant mass cut:

The invariant mass calculations described in sections 5.1.4 and 5.1.5 are also applied, but the selection cut is reversed and re-optimised. The pair track used in the calculation is a tertiary positron candidate in addition to the selected leading and pion tracks. Events are passed if they have $m_{\text{inv}} < 55$ MeV$/c^2$. The effect of this cut on the TPC control sample is shown in Fig. 40.

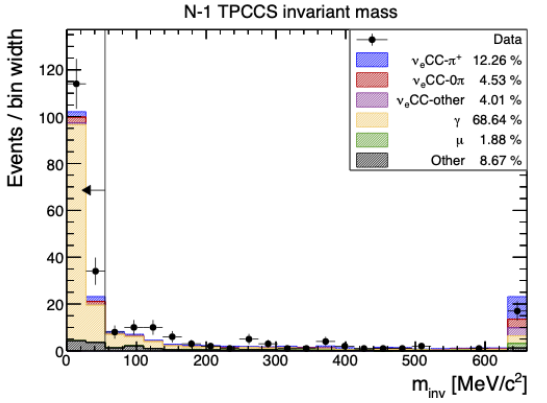

Figure 40. A distribution of the invariant mass, m_{inv}, of the leading and pair candidate tracks for the TPC control sample. The arrow indicates the accepted events.

13. **Upsteam ECal veto:**
    The same upstream ECal veto (cut 12) described in section 5.1.5 is applied.

5.1.7 FGD control sample cuts

The selection cuts used for the FGD control sample are:

11. **Michel electron cut:**
    The same Michel electron tag (cut 11) as described in section 5.1.5 is applied.

12. **Reverse invariant mass cut:**
    The invariant mass calculation described in sections 5.1.4 and 5.1.5 are also applied, but the selection cut is reversed and re-optimised. The pair track is a positron candidate. Events are passed if they have $m_{\text{inv}} < 55$ MeV$/c^2$. The effect of this cut on the FGD control sample is shown in Fig. 41.

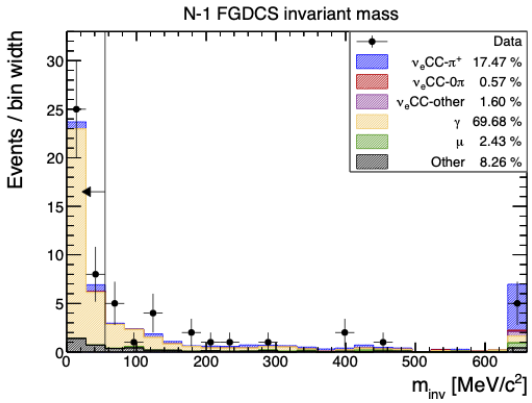

Figure 41. A distribution of the invariant mass, m_{inv}, of the leading and pair candidate tracks for the FGD control sample. The arrow indicates the accepted events.

13. **External FGD cut:**
    Events with tracks originating in FGDs 2 or 3 are removed.

5.2 Selection outputs

5.2.1 Signal samples

Overall, 315 MC events pass the event selection for the signal samples without any phase space restrictions. In the $p_e > 350$ MeV$/c$ restricted phase space, 184 MC events pass which

includes 101 signal events. Only nine signal events have a reconstructed electron momentum below the threshold. The signal samples have a combined purity of $60.1 \pm 1.2\%$ and efficiency of $21.0 \pm 0.5\%$. Out of the selected MC signal events, 86 involve single π^+ production, 13 events involve double π^+ production and one event produces three π^+.

TPC signal sample:

The outputs of the event selection process for the TPC signal sample are shown in several different topologies and sets of variables in Figs. 42, 43 and 44. The TPC sample selects a total of 111 data events and 116 MC events. The TPC sample has a purity of $50.1 \pm 1.0\%$ and efficiency of $12.2 \pm 0.4\%$.

The vast majority ν_e events which pass the TPC selection originate from DIS or RES interactions, and very small contributions occur as a result of CCQE and 2p2h interactions which together comprise around 10% of all ν_e events. The main backgrounds are from ν_e events which do not involve pion production, as well as γ events from ν_μCC and NC interactions.

The leading track particle is correctly identified as an electron in 90% of cases, and around 8% of events instead have a misidentified muon. For the pion track, just over half of selected events have a positively charged pion as the true particle, but a large number of events ($\sim 40\%$) have protons as the pion track true particle. Since the signal definition has no restrictions on additional hadron production, protons are misidentified as the pion track for true signal events around 24% of the time. These are particularly prominent above ~ 1.5 GeV$/c$. For this reason, the phase space boundary on true and reconstructed pion momentum at 1.5 GeV$/c$ is imposed.

The data-MC agreement is generally good in most bins; there are no signs of any substantial low momentum event excesses. The 0-350 MeV$/c$ bin is omitted as this has a high photon background and very low purity; it also does not enter the cross section calculation.

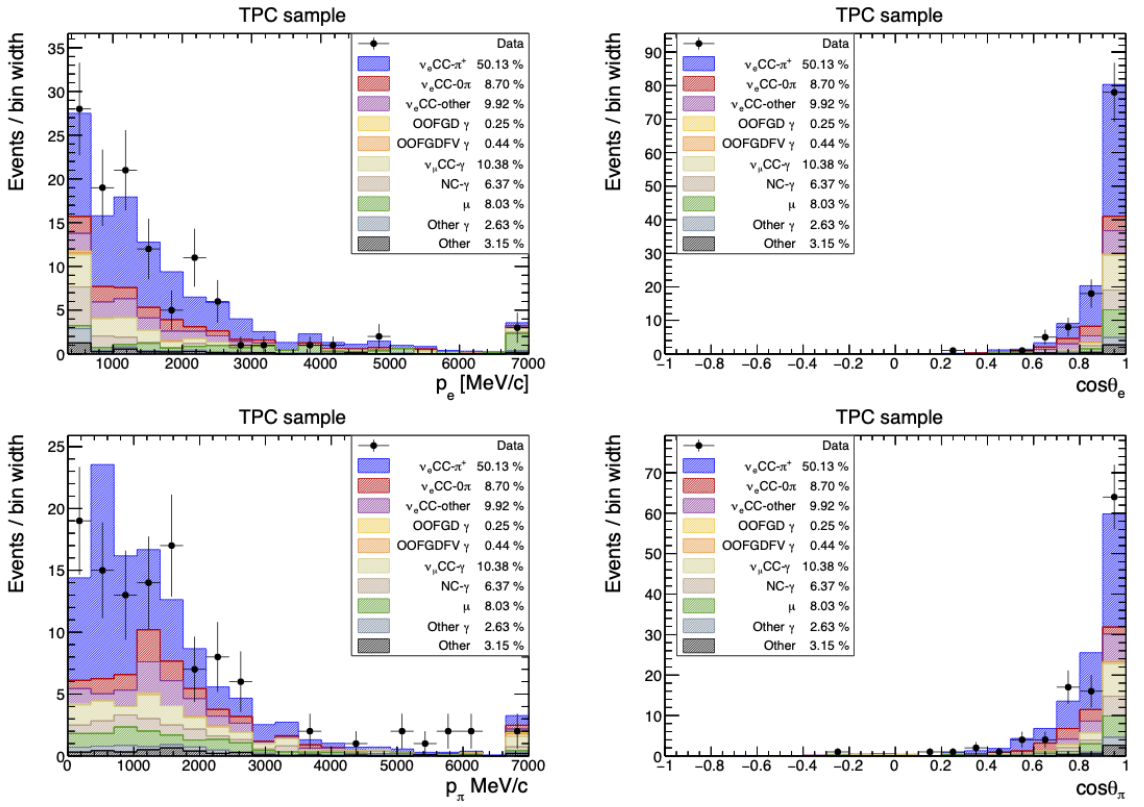

Figure 42. Distributions of reconstructed electron and pion momentum and angle, p_e, $\cos\theta_e$, p_π and $\cos\theta_\pi$, for the TPC signal sample. Events are categorised by the event type categorisation. Events with $p_e < 350$ MeV$/c$ are omitted.

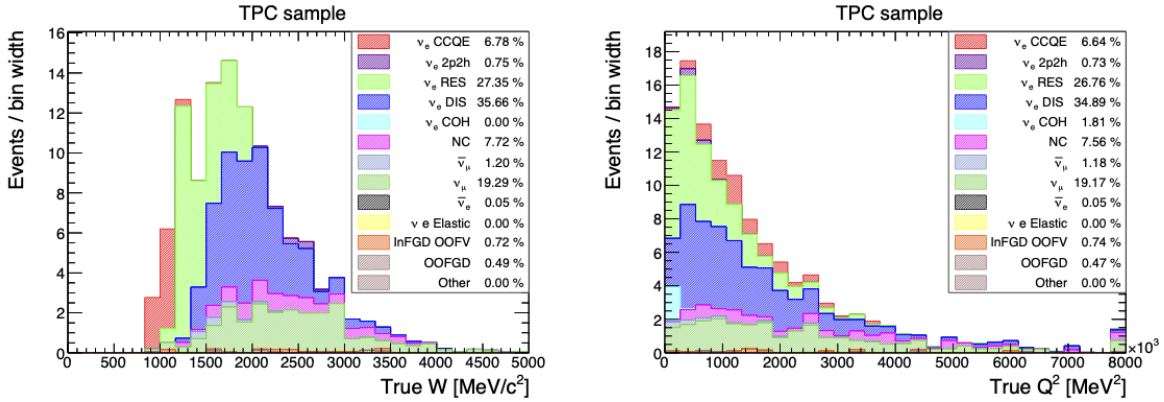

Figure 43. Distributions of true invariant hadronic mass W true momentum transfer Q^2 for the TPC signal sample. Events are categorised by the interaction type categorisation. Events with $p_e <$ 350 MeV$/c$ are omitted.

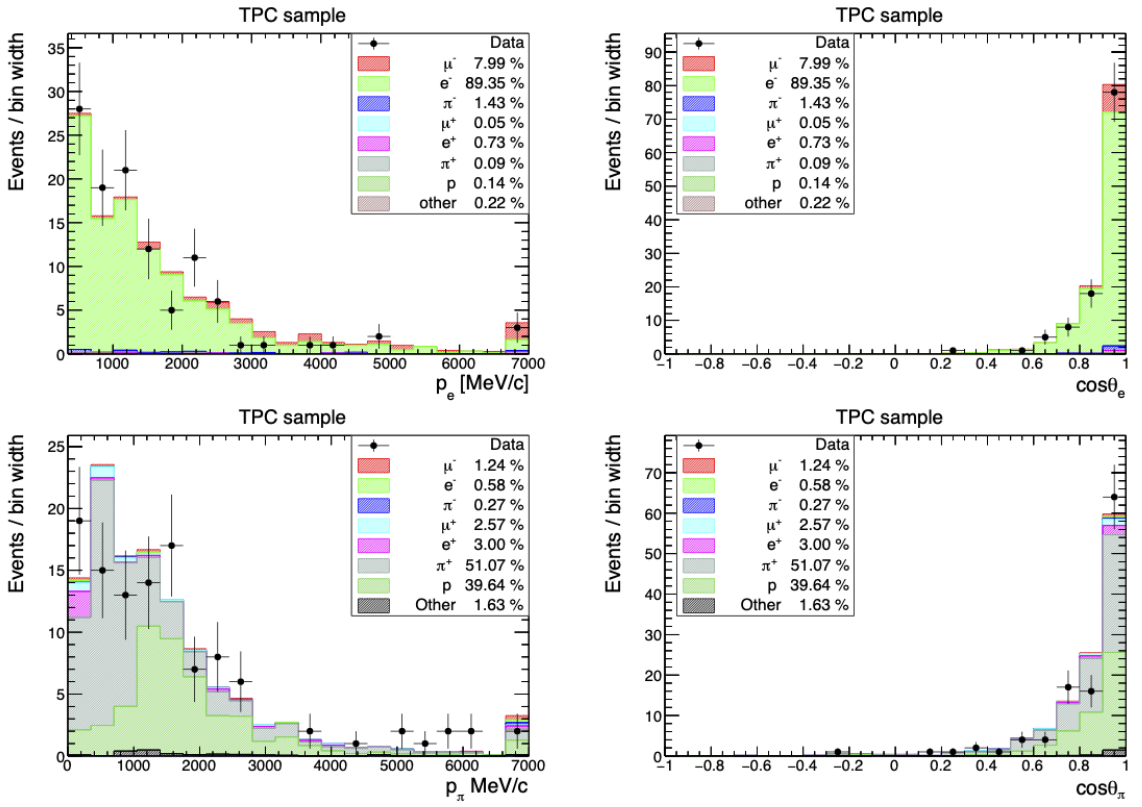

Figure 44. Distributions of reconstructed electron and pion momentum and angle, p_e, $\cos\theta_e$, p_π and $\cos\theta_\pi$, for the TPC signal sample. Events are categorised by the main track (upper) and pion track (lower) particle species topologies. Events with $p_e < 350$ MeV$/c$ are omitted.

FGD signal sample:

For the FGD sample, 62 data events pass the selection compared with 65 predicted from MC. The FGD sample has a purity of $60.2 \pm 0.8\%$ and efficiency of $8.7 \pm 0.3\%$. The outputs of the FGD signal-enriched sample are also shown in several different topologies and variables in Figs. 45, 46 and 47.

As with the TPC sample, the ν_e events also largely originate from RES and DIS interactions for just under 70% of selected events. The largest backgrounds are also generally as a result of ν_μ and NC γ interactions; the ν_e background is notably lower compared with the TPC sample. The FGD sample also has a larger OOFGD-γ contribution to the background than the TPC sample. The track selection performance is comparable to that of the TPC sample.

The data-MC agreement for the FGD sample is also excellent, including for the pion kinematics which uses the novel momentum and angular reconstruction method.

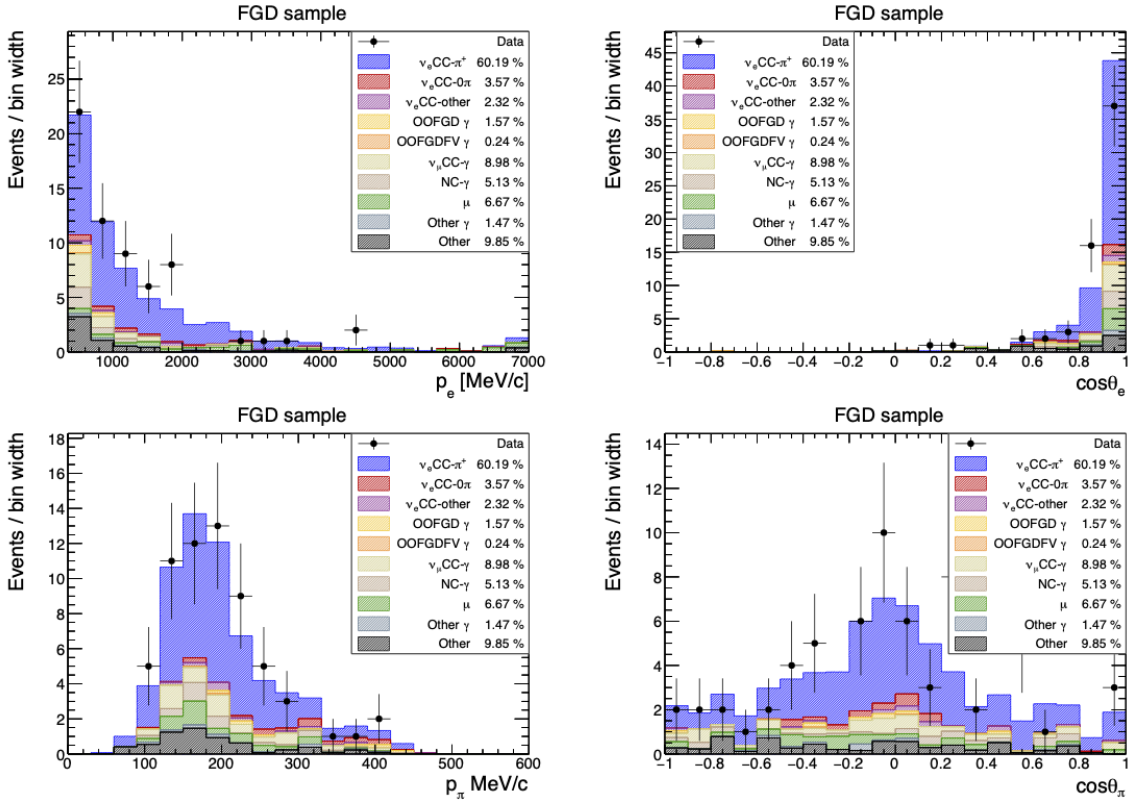

Figure 45. Distributions of reconstructed electron and pion momentum and angle, p_e, $\cos\theta_e$, p_π and $\cos\theta_\pi$, for the FGD signal sample. Events are categorised by the event type categorisation. Events with $p_e < 350\ \mathrm{MeV}/c$ are omitted.

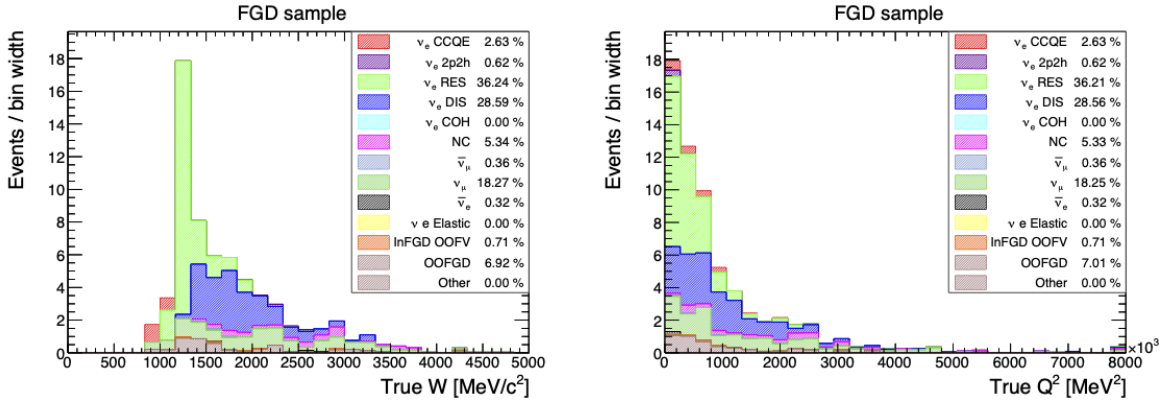

Figure 46. Distributions of true invariant hadronic mass W true momentum transfer Q^2 for the FGD signal sample. Events are categorised by the interaction type categorisation. Events with $p_e < 350\ \mathrm{MeV}/c$ are omitted.

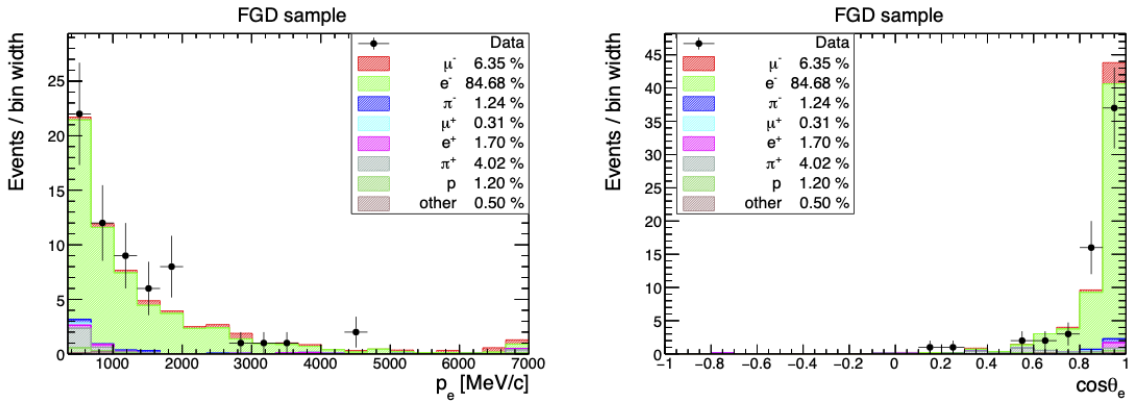

Figure 47. Distributions of reconstructed electron momentum and angle, p_e and $\cos\theta_e$, for the FGD signal sample. Events are categorised by the main track particle species categorisation. Events with $p_e < 350$ MeV$/c$ are omitted.

Combined signal sample phase space:

The distributions of signal and background events for the combined signal-enriched samples are shown as two-dimensional distributions of the true electron and pion kinematic phase spaces in Fig. 48. The signal events in the signal-enriched samples are generally distributed in the same regions of the electron kinematics phase space. In the pion kinematics phase space, the FGD sample contributions are dominant in the low momentum and high angle regions. These contributions are in-line with expectations from the sensitivity studies detailed in section 4.3.1. The relative angular contributions from each signal sample are also as expected given that TPC sample events all move downstream, while FGD sample events can be backwards-going.

Signal events predominantly occupy the low angle electron kinematics phase space ($\cos\theta_e \gtrsim 0.7$); background events are mostly present in the same region as the signal, but the backgrounds tend to also occupy the high electron angle region. The signal is also less present in the low electron momentum region ($p_e \lesssim 300$ MeV$/c$) compared to background events. These differences in relative presence across the true electron kinematics phase space are the basis for the phase space constraints introduced in section 4.2.2.

The signal and background events generally occupy the same momentum and angular regions in the true pion kinematics phase space; it is difficult to impose any equivalent phase space constraints aimed at specifically omitting background events in the pion kinematics distributions.

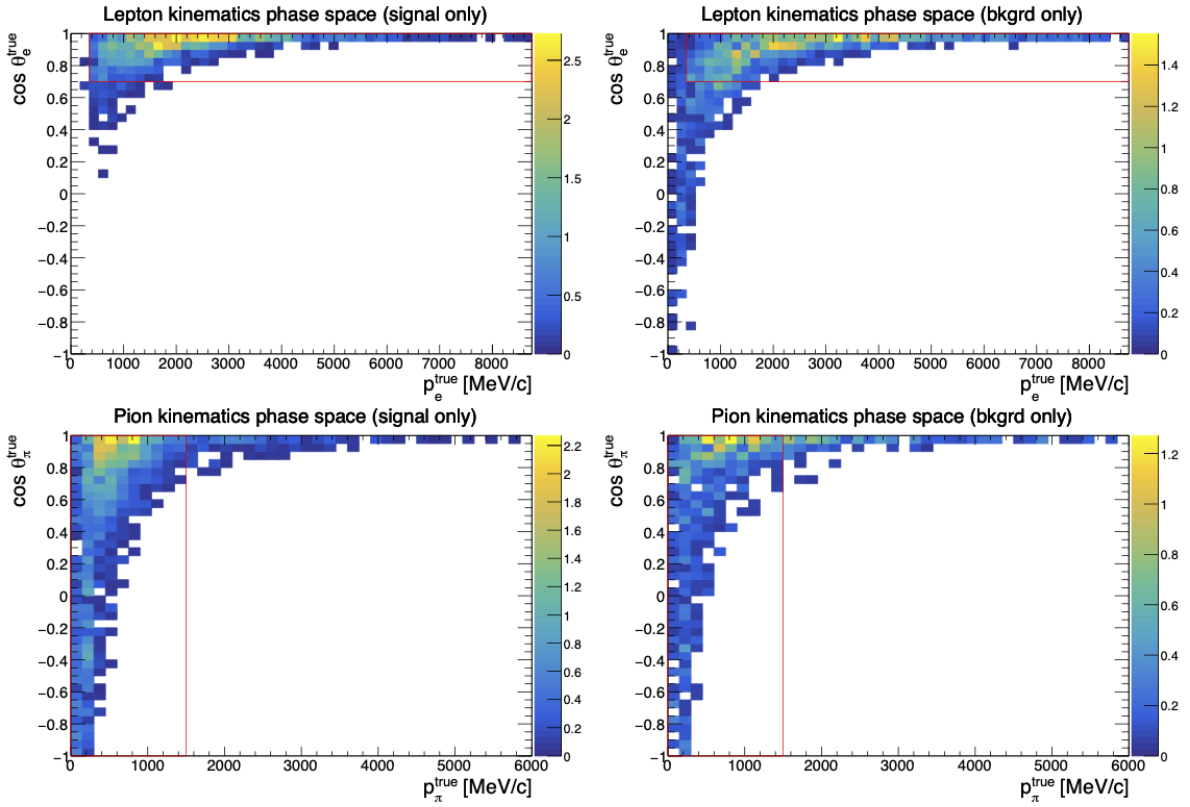

Figure 48. Phase space diagrams for the true lepton kinematics (upper) and true pion kinematics (lower) (p_e^{true}, θ_e^{true}, p_π^{true}, θ_π^{true}). Plots on the left only show signal events. Plots on the right only show background events. The z-axis indicates the POT-normalised MC event count per bin. The red boxes show the in-phase space regions.

5.2.2 Control samples

The control sample outputs are presented in this section. The purities presented in the legends of these plots are referred to such that the in-FGD1 photon events are considered signal.

TPC control sample:

The TPC sample has 148 data events and 123 MC events. The outputs of the event selection process for the TPC control sample is shown in Fig. 49. The in-FGD1 photon purity from ν_μCC-γ and NC-γ events is $\sim$51%; the largest background is from OOFGD and OOFGDFV γ events. A minimal amount of signal enters the sample.

The data-MC agreement is generally reasonable but marginally worse compared to the signal-enriched samples. This is driven both by the relatively poor understanding of the behaviour of photons in ND280, as well as the very low statistics associated with this sample.

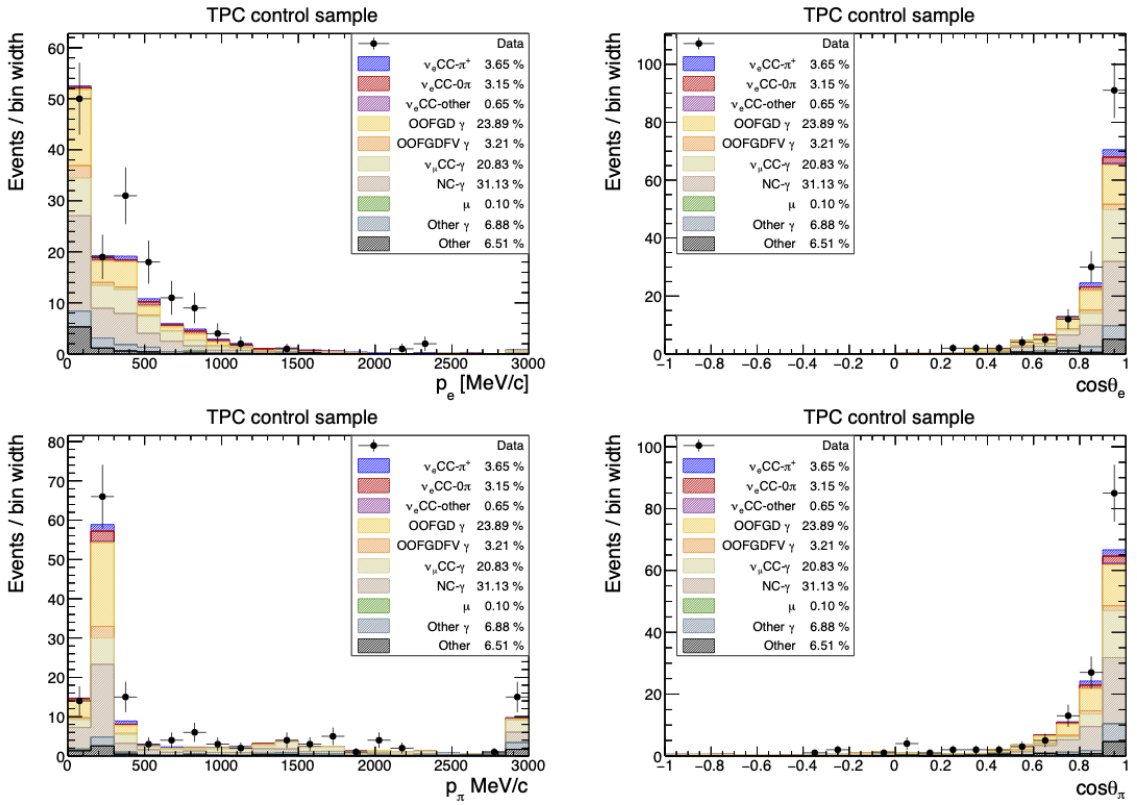

Figure 49. Distributions of reconstructed electron and pion momentum and angle, p_e, $\cos\theta_e$, p_π and $\cos\theta_\pi$, for the TPC control sample. Events are categorised by the event type categorisation.

FGD control sample:

A total of 39 events pass into the FGD control sample compared to the 36 expected. The outputs of the event selection process for the FGD control sample are shown in Fig. 50. The in-FGD1 photon purity from ν_μCC-γ and NC-γ events is $\sim$67% and, as with the TPC control sample, the remaining OOFGD- and OOFGDFV-γ events constitute the largest background and a minimal amount of signal enters the sample.

As with the TPC control sample, the overall data-MC agreement is generally reasonable. In some cases, the disagreement appears larger but the sizeable uncertainties on the data points as a result of the very low statistics means these are generally all within 2σ.

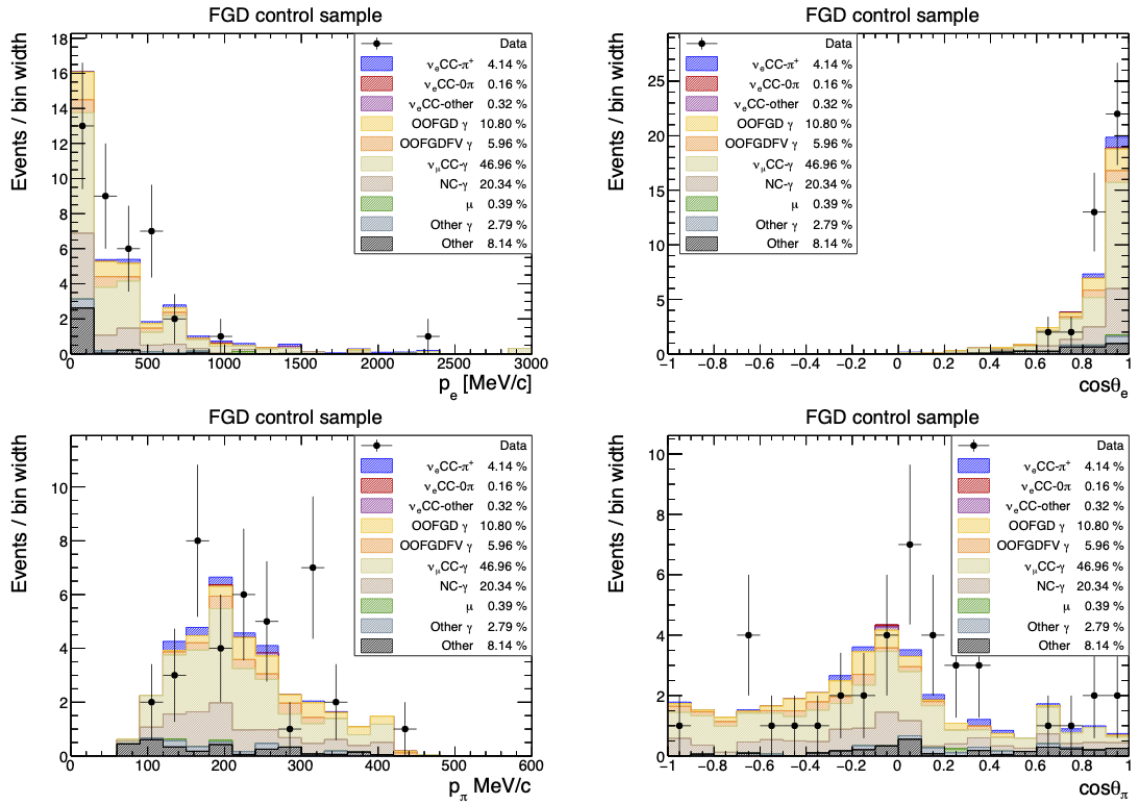

Figure 50. Distributions of reconstructed electron and pion momentum and angle, p_e, $\cos\theta_e$, p_π and $\cos\theta_\pi$, for the FGD control sample. Events are categorised by the event type categorisation.

5.3 Selection performance

5.3.1 Selection cuts

The effectiveness of a particular selection cut is quantified by comparing the purity and efficiency of the sample with and without the specific cut applied. The change in purity and efficiency after applying the selection cut are used to assess the overall impact on the sample. Histograms of the change in purity $\Delta\rho$ and efficiency $\Delta\varepsilon$ of each selection cut for all samples are shown in Fig. 51; these are alternative representations of the $N-1$ plots with the change in selection parameters listed by cut. Note that the efficiency and purity definitions are modified for the control sample histograms such that the in-FGD1 photon background is treated as the signal. The most effective selection cuts should substantially increase the selection purity with minimal efficiency loss.

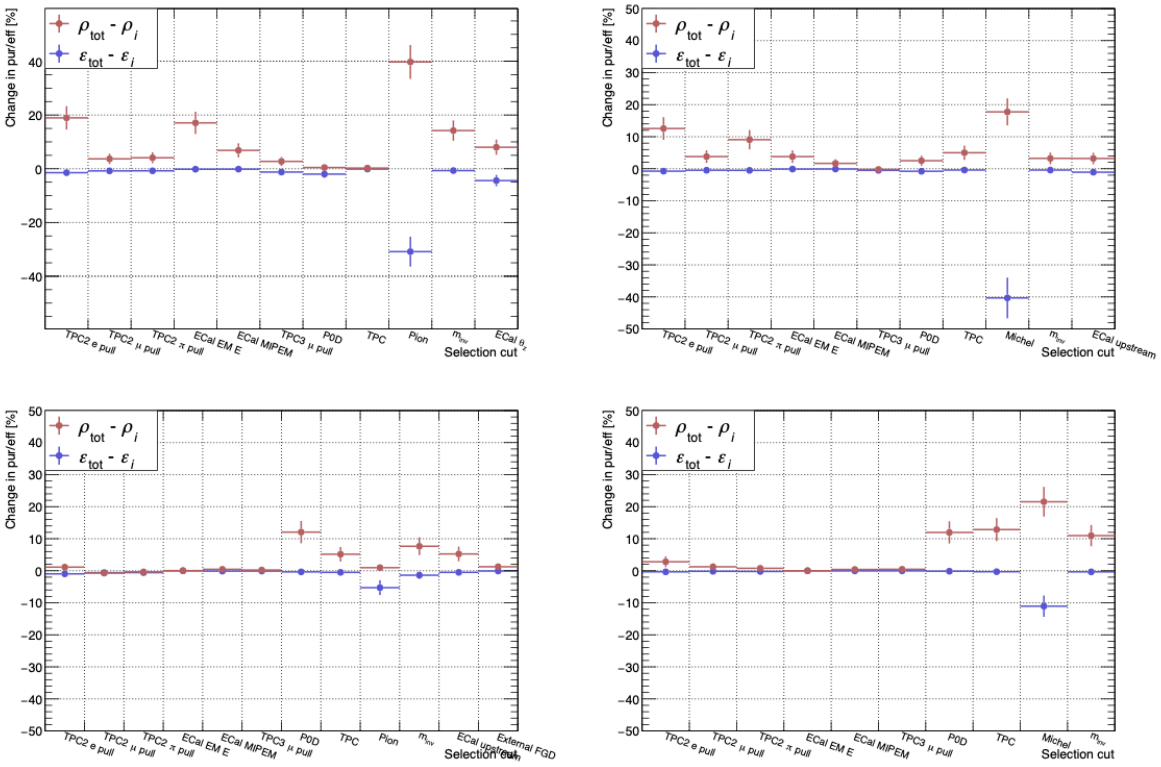

Figure 51. $N-1$ bar charts of the selection cut performance for the TPC signal sample (upper left), FGD signal sample (upper right), TPC control sample (lower left) and FGD control sample (lower right). These indicate the change in purity and efficiency, ρ_i and ε_i, as a result of the i^{th} cut in each sample. Note that the leading track momentum constraint of 350 MeV$/c$ is not applied.

The vast majority of the selection cuts in the signal samples perform well. Notably the pion and Michel electron cuts significantly decrease the efficiency at the expense of large purity increases. These cuts have the same effect on the control samples and raise the in-FGD1 photon purity moderately but at the expense of a large efficiency loss. Although inefficient, these cuts are necessary to achieve purity values above $\sim 50\%$, but future selections with the upgraded ND280 should attempt to re-optimise or replace these specific cuts.

The TPC and P0D vetoes offer minimal improvement to the TPC signal sample. However, these are retained because they significantly improve the purity of the FGD sample and both control samples. Keeping these cuts common in all selection branches simplifies the pile-up calculation for evaluating the systematic uncertainty associated with when these vetoes accidentally remove signal events. The remaining cuts all perform excellently with minimal efficiency loss and moderate or large purity increases. The invariant mass cuts are particularly effective in all samples.

5.3.2 Track reconstruction

The reconstruction performance of the TPCs is generally very accurate. Clear diagonal trends between reconstructed and true variables are apparent as shown in the truth-level comparison plots in Fig. 52. Some low momentum bias is evident in the electron momentum plot, which is a result of electrons losing energy to radiating photons through Bremsstrahlung.

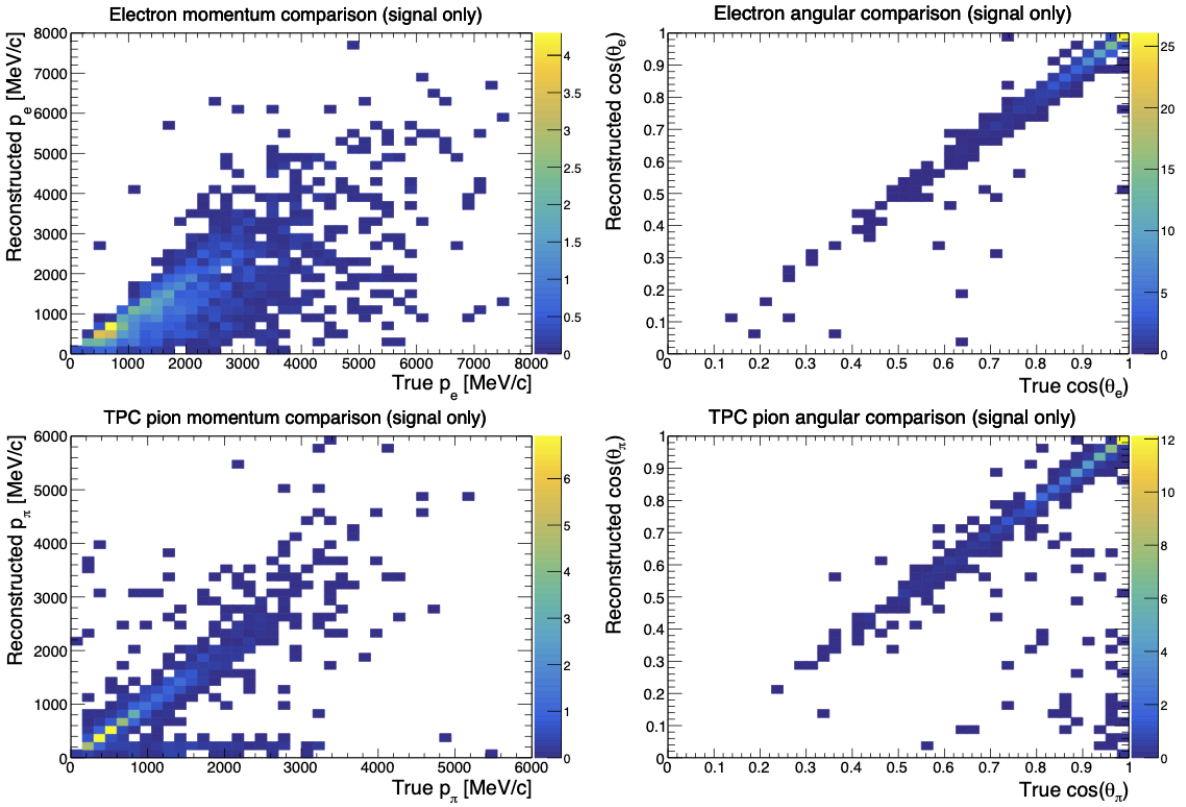

Figure 52. Truth-level comparison of the reconstructed electron (upper) and pion (lower) momentum $p_{e,\pi}$ and angular $\cos\theta_{e,\pi}$ distributions for particles which cross the TPCs and leave reconstructable tracks. These plots only show signal MC events.

The performance of the Michel electron pion reconstruction technique is assessed by comparing the true and reconstructed pion momentum and angle distributions; these plots are shown in Fig. 53.

The momentum reconstruction performs reasonably well, there is a clear diagonal trend between the true and reconstructed momentum, but with slightly more spread when compared with the TPC reconstruction performance. Below $\sim$50 MeV$/c$, the reconstruction performance tends to worsen and there is a slight bias towards low true pion momentum values. The

resolution of the reconstructed pion momentum is shown in Fig. 54. Below $\sim$75 MeV/c, the reconstruction performance degrades significantly as the residuals deviate significantly from zero. However, the number of events tends to be very low in this region and most events are contained within the 100-300 MeV/c range. The angular reconstruction is substantially worse; signs of a diagonal trend are present but there is significant deviation from this at all angles. This is because accurately reconstructing the exact position of the Michel electron vertex is difficult due to the alternating layer structure of the FGDs. The angular information for the FGD sample is therefore not used in the cross section analysis and a single pion angle bin is used for the FGD sample binning scheme.

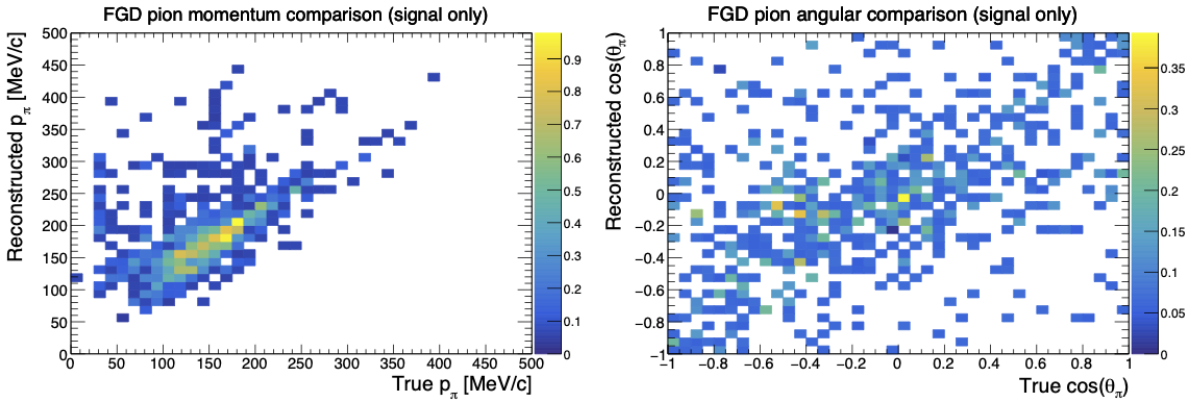

Figure 53. Two-dimensional histograms showing the true pion momentum p_π (left) angular $\cos\theta_\pi$ (right) distributions against the equivalent reconstructed variables. These plots are only shown for signal events which enter the FGD sample.

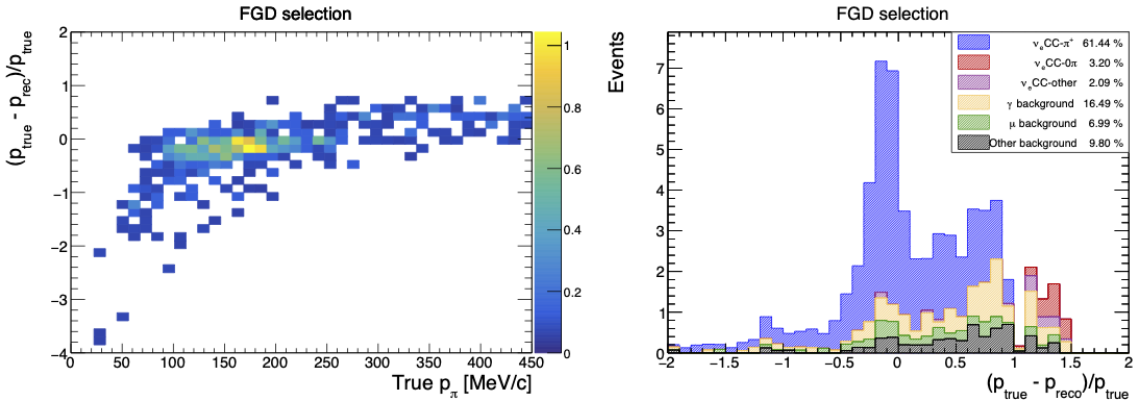

Figure 54. The pion momentum resolution $(p_{\text{true}} - p_{\text{reco}})/p_{\text{true}}$ as calculated from Michel electron FGD hits, as a two-dimensional, signal-only histogram as a function of true pion momentum (left) and as a one-dimensional histogram with background events included (right).

5.3.3 Differential efficiencies

The differential selection efficiency as a function of true kinematic variables is shown for the signal-enriched samples in Fig. 55. These plots show the relative performance of each sample, as well as the overall efficiency which is useful for determining the binning scheme for the cross section extraction. For the true electron kinematics, the efficiency distribution shapes are similar and the FGD sample is generally less efficient. The efficiencies vary more significantly for the true pion kinematics. The FGD sample has a higher efficiency than the TPC sample in the low pion momentum range as the FGD-contained pions generally have lower momentum. The TPC sample also has better efficiency for low-angle pions, while the FGD sample is able to select a significant amount of backward-going or high-angle pions from Michel electrons.

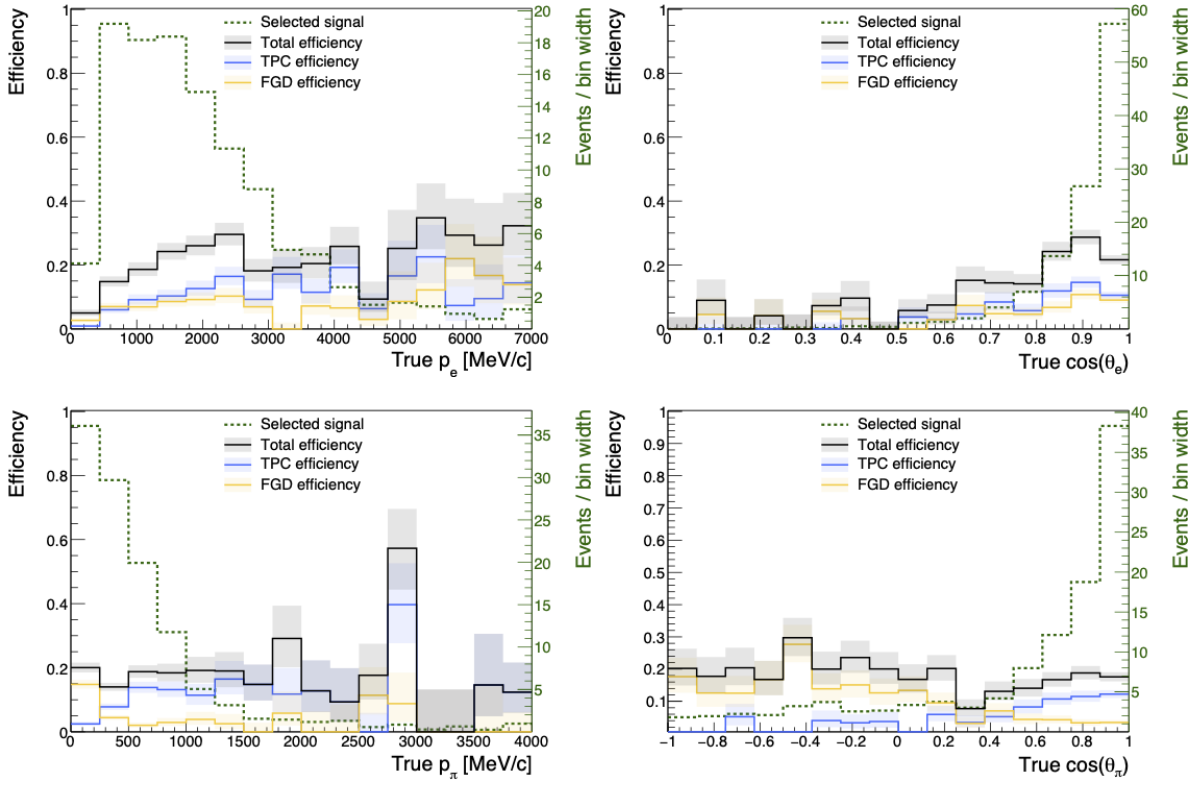

Figure 55. The selection efficiency as a function of true lepton and pion kinematics, p_e, $\cos\theta_e$, p_π and $\cos\theta_\pi$, for the TPC, FGD and combined signal samples with all selection cuts applied. The green distribution show the true signal events which pass all selection cuts.

The differential efficiency plots of both signal samples across the two-dimensional phase spaces for true electron and pion kinematics are shown Fig. 56. The efficiency is generally lowest in the high angle, low momentum regions for the true electron kinematics phase space.

The pion phase space show no significant patterns in the efficiency.

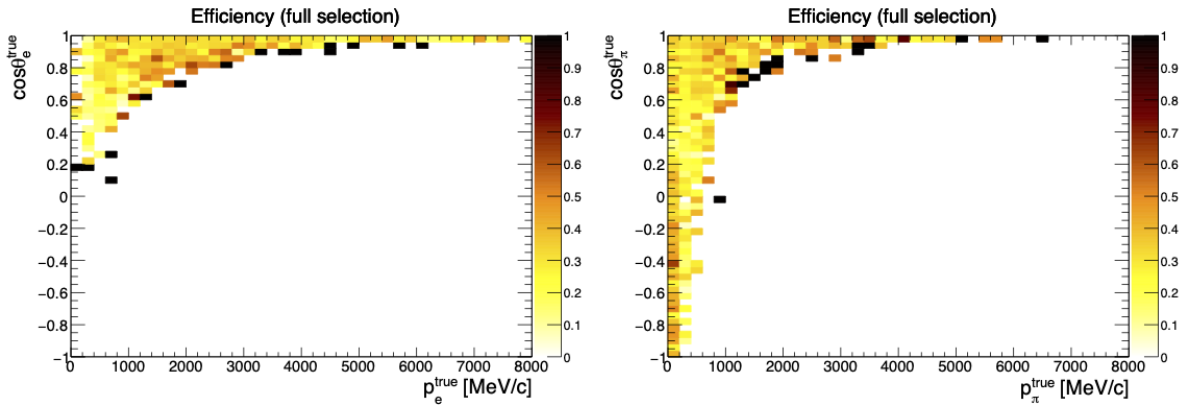

Figure 56. Two-dimensional distributions of the selection efficiency as projected onto true electron kinematics (left) and true pion kinematics (right). The z-axis indicates the efficiency values for each two-dimensional bin.

5.3.4 Control sample validation

The control samples aim to select the same types of photon background events which appear in the signal-enriched samples. Several comparisons are performed to ensure the selected photons in the control samples are representative of the photon backgrounds which appear in the signal samples. These comparisons are performed with MC events only, as it is not possible to distinguish the interaction types of data events.

The shapes of several kinematics distributions are compared in Fig. 57. The true electron momentum shows the largest disagreement between the two distributions. The photons which appear in the selection as background events tend to have higher momentum, while the control sample photons are more concentrated to the lower momentum bins. The reconstructed electron angle, true pion momentum and true Q^2 match more closely and agree within the statistical uncertainty for most bins.

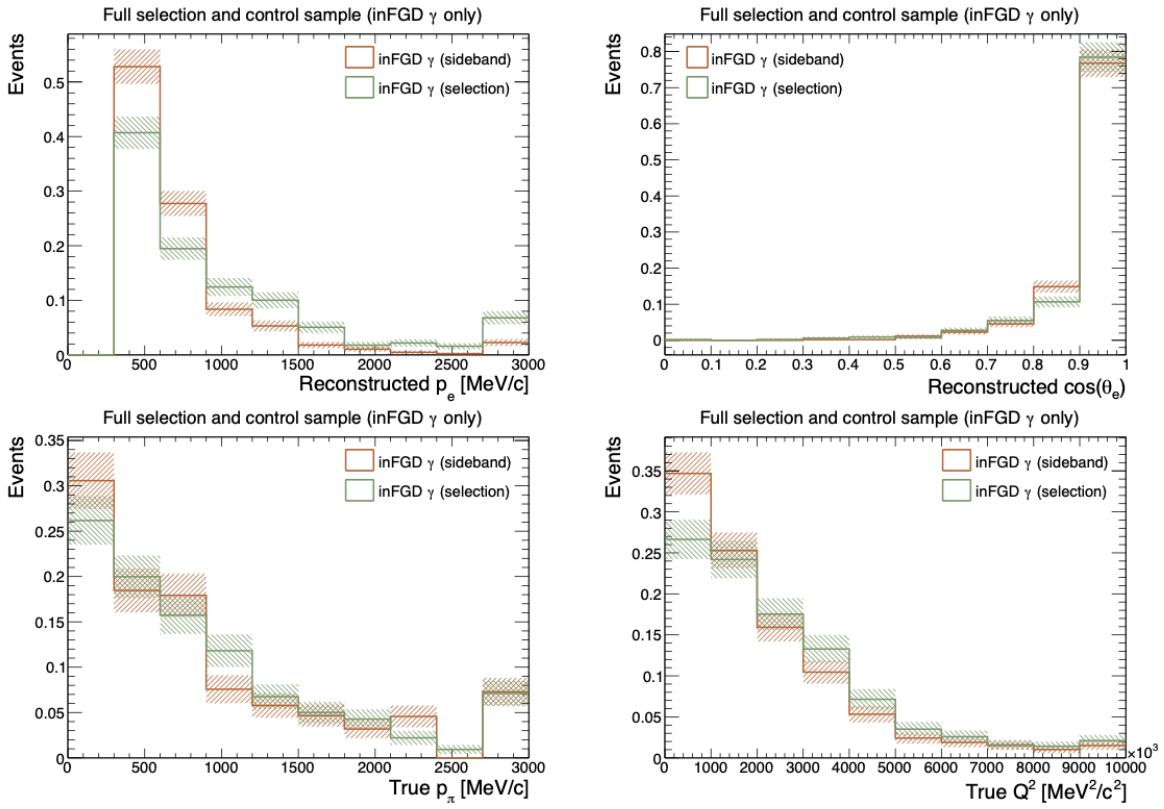

Figure 57. Shape comparisons of the control sample and signal sample in-FGD photon events for the reconstructed electron kinematics, p_e and $\cos\theta_e$ (upper), as well as for the true pion momentum p_π and true momentum transfer squared Q^2 (lower). All histograms are normalised to unity and error bars indicate the statistical uncertainties.

Comparisons of the interaction types which comprise the in-FGD1 photon backgrounds are also shown in Fig. 58. The background and control sample photons both have DIS and NC as the main interactions, but the control sample has $\sim$15% higher purity for NC events and 11% lower purity for DIS events. The RES contribution is also 5% lower in the control samples.

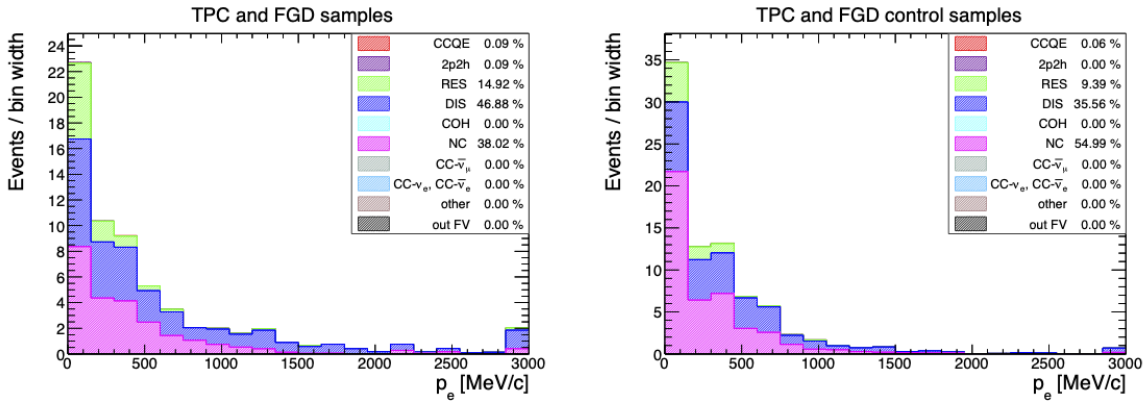

Figure 58. Comparison of the electron momentum with events categorised by interaction types for in-FGD photons only for the combined signal samples (left) and the combined control samples (right).

Another validation compares the proportions of photon events which occur from CC or NC interactions and the number of neutral pions produced. This is shown in Fig. 59. The main difference is that in-FGD1 NC single pion production is more prevalent in the control samples than in the backgrounds of the signal samples by $\sim$15%. The proportion of photons originating from CC single and multiple pion production is also lower by $\sim$ 5-10%.

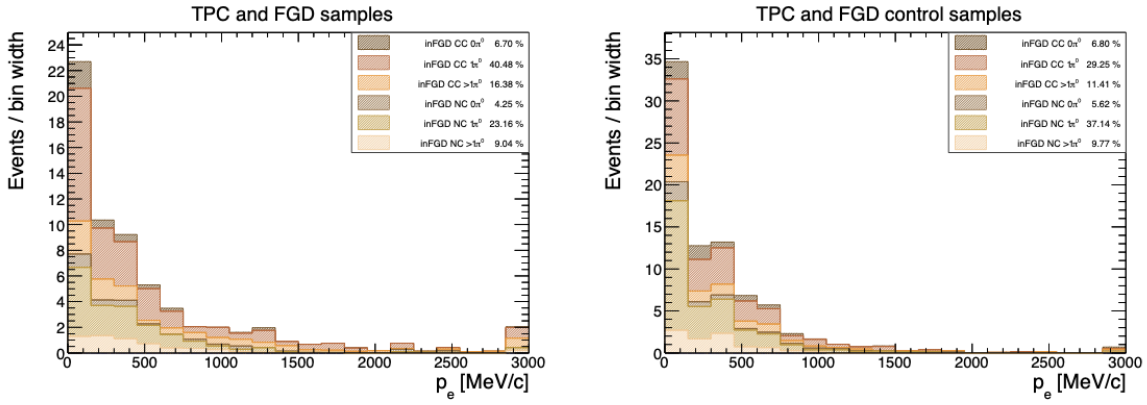

Figure 59. Comparison of the electron momentum with events categorised by interaction types for in-FGD photons only for the combined signal samples (left) and the combined control samples (right).

Given the limited statistics and small overall number of in-FGD1 photon events, the control samples generally describe the photon background reasonably well, with similar ratios of interaction types and photon origins that cover the same regions of kinematics phase space.

CHAPTER 6

SYSTEMATIC UNCERTAINTIES

This chapter describes how the systematic uncertainties from detector, flux and cross section model sources are evaluated; these are described in section 6.1, 6.2 and 6.3. Each source of systematic uncertainty is supplied to the cross section fit model as a covariance matrix; these are separately evaluated and parametrised as part of the fitting process.

6.1 Detector systematic uncertainties

Detector systematic uncertainties are associated with the detection and reconstruction methods utilised by this analysis. A set of standard uncertainties has been extensively studied and evaluated before using ND280 and no significant re-evaluation is performed as part of this work. Brief descriptions of each uncertainty are presented in section 6.1.1. There are also several custom uncertainties which are unique to this analysis and are therefore described in more detail in section 6.1.2.

6.1.1 Standard ND280 detector systematic uncertainties

The following systematic uncertainties from ND280 are considered and addressed:

- **Magnetic field distortions:**
  In the TPCs, charged particles drift along the magnetic field lines of the UA1 magnet towards the readout planes. Imperfections in the magnetic and electric fields can cause the paths of drift electrons to become distorted, leading to biases in momentum reconstruction. Corrections are applied based on measurements of the magnetic field

[107].

- **TPC momentum resolution and scale:**
  Charged particles trajectories often span multiple TPCs. This means the momentum of a charged particle can be separately measured by studying the transverse momentum relative to the *B*-field. A systematic uncertainty is derived from data-MC comparisons of measurements of the transverse momentum in different TPCs [108].

- **TPC PID variation:**
  Pull distributions based on energy deposition curves are used to discriminate between particle species in the TPCs. These tend to be Gaussian and fit comparisons between data and MC yield a systematic uncertainty on TPC PID process [109].

- **ECal EM energy resolution and scale:**
  The EM energy of a reconstructed ECal cluster is calculated from its hit distribution and charge deposition. A systematic uncertainty is derived by comparing the momentum of reconstructed TPC-ECal tracks as measured independently in separate detectors. The data-MC difference is calculated to determine the systematic uncertainty [110].

- **TPC cluster efficiency:**
  TPC clusters are identified by searching for groups of adjacent single TPC pad hits. These correspond to points along the ionisation trace created by charged particles moving through the TPC gas volume. The centre of ionisation is calculated from the angles of these reconstructed tracks. Imperfections in the TPC hardware can cause some tracks to be missed affects the cluster identification process. An uncertainty on the accuracy of cluster reconstruction is determined from studies involving beam and cosmic muons [111].

- **TPC track efficiency:**
  The TPC track efficiency is the systematic uncertainty associated with the reconstructing the tracks of charged particles. A control sample of through-going muons is used to derive an uncertainty on track detection by comparing the efficiency between data and MC [112].

- **TPC charge ID efficiency:**
  Particle charge is determined by studying the curvature of tracks in the TPCs. In some cases, hardware imperfections may lead to the same tracks being identified as oppositely-charged in different TPCs. A control sample of upstream muons which have starting

vertices in the P0D is used to evaluate this uncertainty in different momentum ranges by comparing data and MC [113].

- **TPC-ECal and TPC-FGD matching efficiencies:**
  The TPC-ECal and TPC-FGD matching efficiencies are systematic uncertainties which quantify the how effectively adjacent sub-detector modules match 'local' tracks contained within the sub-detector to the same 'global' track across all of ND280. A range of control samples are used to determine the track matching efficiency between detectors and the uncertainty is derived from data-MC differences [110, 114].

- **OOFV background:**
  Some events have true vertices outside of the FGD1 FV, but the vertices can sometimes be mis-reconstructed within this region. An uncertainty of 30% is assumed for these events [115]. This accounts for several sources of OOFV ν_e events, including π^0 production and detector edge effects.

- **Pion and proton secondary interactions:**
  Pions and protons can undergo secondary interactions which occur outside of the nucleus where hadron production occurs; these processes may lead to particle misidentification. A systematic uncertainty for each particle is determined by performing simulation studies using `GEANT4` [116].

- **ECal PID:**
  The ECal PID systematic uncertainty quantifies the error associated with the MIP-EM PID technique which discriminates between muons and photons. The efficiency is evaluated for control samples of electrons, muons and protons assuming a cut value of $R_{\mathrm{MIP/EM}} = 0$ and the systematic uncertainty is derived from the difference between data and MC [110].

- **Michel electron efficiency:**
  The Michel electron cut has a systematic uncertainty associated with its performance in successfully tagging Michel electrons. The cut efficiency and purity are calculated using a control sample of cosmic muons which trigger the FGD. The systematic uncertainty is determined from the differences between the efficiency and purity from evaluating with data and MC [106].

- **Sand muons:**
  Muons can be produced when beam neutrinos interact with the out-of detector matter

which surrounds ND280. These are referred to as *sand muons* and are capable of mimicking FGD interactions. Systematic studies suggest that there is approximately a 10% difference in the number of MC sand events from a dedicated control sample compared with data, so a systematic uncertainty of 10% is assumed [117].

- **FGD mass:**
  The FGD mass is approximated in the ND280 software and a systematic uncertainty is applied to account for any differences between the actual FGD mass. This is propagated at the cross section fitter stage and is not propagated using the event selection outputs.

6.1.2 Custom ND280 detector systematic uncertainties

The additional set of unique systematic uncertainties includes:

- **Pile-up:**
  The TPC, P0D and ECal vetoes used in the event selection can accidentally be triggered by sand muons. This may occur in the same bunch as an event which would otherwise pass the selection. Several *pile-up* systematic uncertainties are used to estimate the errors associated with the event count when these are triggered. Sand muons accidentally triggering any photon veto decreases the total number of events passing the selection.

  These uncertainties are evaluated by calculating correction factors which represent the number of times the vetoes are triggered. This was developed based on a similar implementation as part of the $\overset{(-)}{\nu}_e$CC analysis [85]. The correction factors are calculated by running a dedicated event selection algorithm with each of the four vetoes as the only selection cuts. A tailored MC sample only consisting of sand muons, normal MC and data are supplied to the event selection and the correction factors are calculated. The correction factors are normalised so that the MC and data represent the same number of ND280 spills and POT.

  The systematic uncertainty for each veto is evaluated by calculating the difference in the correction factors between data and MC. The pile-up correction factors also need to be evaluated sequentially to avoid over-counting the correction. For this analysis, the order in which the pile-up corrections are evaluated is: TPC, P0D, upstream ECal and polar ECal. The errors propagated as a function of selected particle kinematics for each of these pile-ups is shown in Fig. 60.

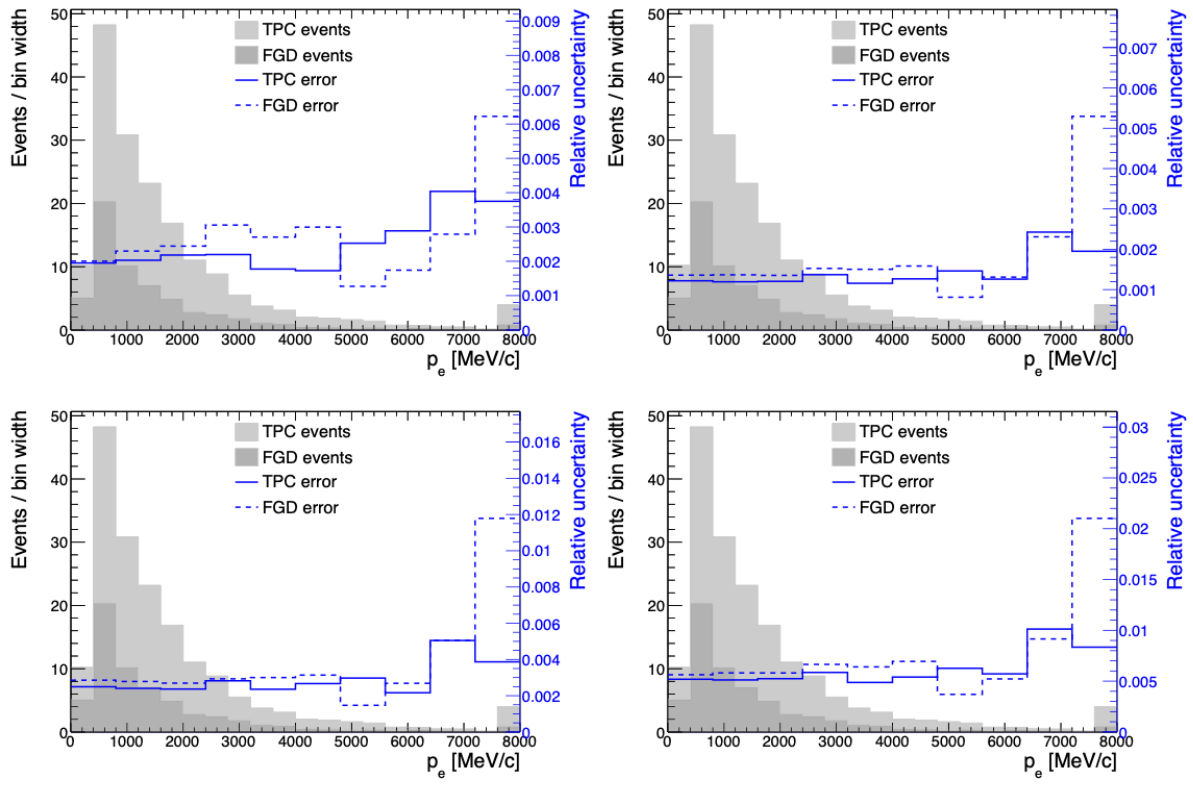

Figure 60. The relative errors overlayed on the signal samples for the P0D veto (tl), TPC veto (tr), upstream ECal veto (bl) and ECal polar angle veto (br) pile-up systematic uncertainties.

- **FGD vertex association:**

  The process of selecting pion and positron tracks requires these to start within 40 mm of the main electron track. A systematic uncertainty is associated with the chosen cut value. This is necessary because some tracks are likely to start within 40 mm of the electron track by coincidence when they may not originate from the same interaction. Alternatively, paired tracks from the same interaction may have mis-reconstructed vertices more than 40 mm apart.

  A control sample of e^+e^- pairs is used to evaluate this systematic uncertainty. This control sample is used as pair production from $\pi^0 \to \gamma\gamma$ decays constitutes the largest background in ν_e selections, meaning the development of this sample from the main selection algorithm is relatively straightforward. An analogous sample involving pion production is likely to be statistically limited and the e^+e^- results are assumed for pion-producing interactions.

  Tracks separated by more than 100 mm are unlikely to have originated from the same

vertex, so the cut efficiency is only evaluated for reconstructed separation distances of 0-100 mm. This control sample shares the same selection cuts as the TPC control sample described in section 5.1.6, but the cuts used to remove the photon backgrounds and identify pions are omitted. A histogram showing the events which pass this control sample is shown in Fig. 61. Note that for this plot, the 40 mm cut is not applied and the cut region is indiciated by the black line.

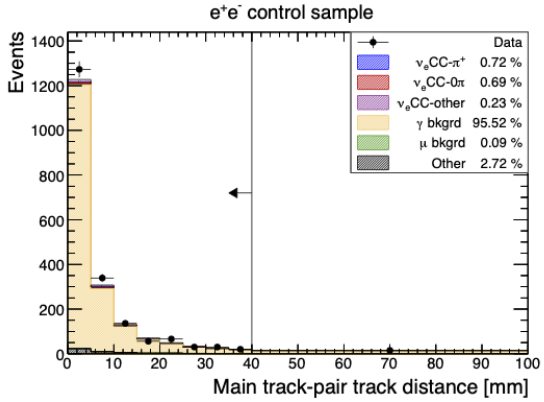

Figure 61. Distribution of the reconstructed distance between the leading and paired track for the electron-positron pair control sample. The black line indicates where the distance cut is imposed in the selection.

The selection has a high OOFV photon purity of $\sim$95%. The efficiency of this selection cut using the 40 mm distance parameter is shown for data and MC in table V.

Sample	Selected pairs	Total pairs	Efficiency
Runs 2, 3, 4, 8 FHC MC	1507.6	1643.0	$0.9176^{+0.0077}_{-0.0065}$
Runs 2, 3, 4, 8 FHC Data	1950.0	2130.0	$0.9155^{+0.0065}_{-0.0060}$

Table V. The number of events passing the 40 mm pair separation cut and the efficiencies for data and MC. The values and errors for the efficiency are calculated using the Clopper-Pearson extraction method in `root` [118].

The relative error corresponding to the FGD vertex association systematic uncertainty is shown overlayed onto the signal sample events in Fig. 62.

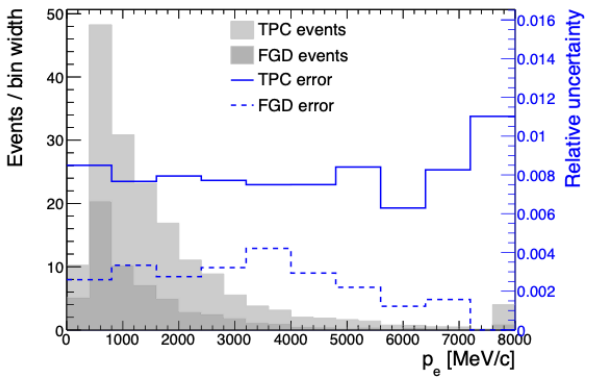

Figure 62. The relative error for the FGD vertex association systematic uncertainty projected onto electron momentum.

- **FGD pion momentum resolution:**
  The momentum of pions from Michel electrons is reconstructed using a function derived from correlating the true Michel electron vertex position and true pion momentum as described in section 4.3.2. A systematic uncertainty accounts for the resolution of this reconstruction method. This was evaluated for a study of ν_μCC1π^+ interactions in ND280 which uses the same pion kinematics reconstruction technique [104].

  A control sample of TPC pions with $p_\pi < 600$ MeV$/c$ is compared with the momentum of reconstructed pions from Michel electrons. Distributions of momentum resolution are fitted with a Lorentzian function. The systematic uncertainty is derived from the differences between the means and resolutions of the Lorentzian fits applied to data and MC distributions. The relative uncertainty is shown in Fig. 63.

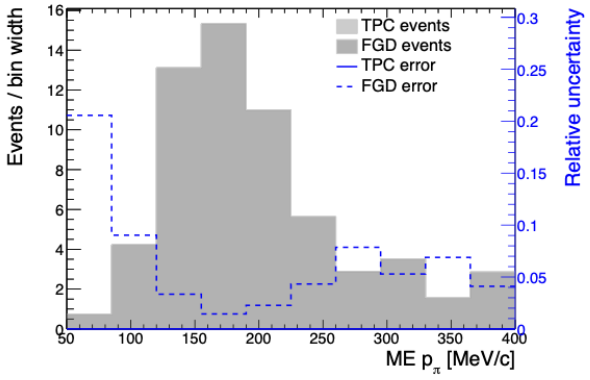

Figure 63. The relative error for the FGD pion Michel electron resolution systematic uncertainty projected onto FGD pion momentum.

6.1.3 Overall uncertainties

A list of all total relative errors from each detector systematic uncertainty is shown in table VI. These errors are listed for the sub-selections of the signal and control samples, as well as the overall error in each case.

Systematic uncertainty	**Selection error [%]**			**Sideband error [%]**		
	TPC	**FGD**	**TOT**	**TPC**	**FGD**	**TOT**
B-field distortions	0.136	0.260	0.115	0.337	0.793	0.373
TPC momentum resolution	0.467	0.730	0.338	1.149	1.487	1.062
TPC momentum scale	0.431	0.489	0.447	0.576	1.161	0.578
TPC PID variation	2.115	1.531	1.739	1.580	2.149	1.465
ECal EM energy resolution	0.075	0.077	0.053	0.014	0.047	0.012
ECal EM energy scale	0.245	0.147	0.207	0.007	0.027	0.006
TPC cluster efficiency	0.015	0.015	0.015	0.010	0.050	0.014
TPC track efficiency	1.184	1.086	1.149	1.303	0.765	1.266
TPC charge ID efficiency	0.704	0.622	0.655	0.737	0.446	0.688
TPC-FGD matching efficiency	0.174	0.093	0.146	0.112	0.199	0.126
TPC-ECal matching efficiency	1.996	1.671	1.879	1.873	1.680	1.809
ν_e OOFV background	0.269	3.447	1.311	9.385	3.937	8.662
Pion secondary interactions	1.801	0.200	1.234	0.642	2.712	0.617
Proton secondary interactions	1.043	0.841	0.973	0.626	0.622	0.618
ECal PID	0.784	0.828	0.779	0.689	0.534	0.642
Michel electron efficiency	0.262	1.304	0.281	0.021	1.005	0.112
Sand μ background	0.000	0.000	0.000	0.000	0.000	0.000
TPC veto pile-up	0.122	0.136	0.126	0.126	0.120	0.127
P0D veto pile-up	0.202	0.221	0.209	0.216	0.181	0.211
ECal upstream veto pile-up	0.246	0.279	0.257	0.254	0.251	0.259
ECal θ_z veto pile-up	0.521	0.572	0.538	0.542	0.498	0.541
FGD vertex association	0.797	0.293	0.622	1.102	0.980	1.076
FGD pion momentum resolution	0.000	0.412	0.412	0.000	0.656	0.656
Total	4.208	5.348	3.966	10.03	6.851	9.285

Table VI. List of the total relative error values for each source of systematic uncertainty due to detector effects split by sample.

The largest sources of uncertainty come from TPC PID variation, TPC-ECal matching, ν_eOOFV and pion SI. The dominant systematic uncertainties are the same between the signal and sideband samples. The uncertainty as a function of the reconstructed electron and pion kinematics for all selected events broken down by sample is shown in Fig. 64.

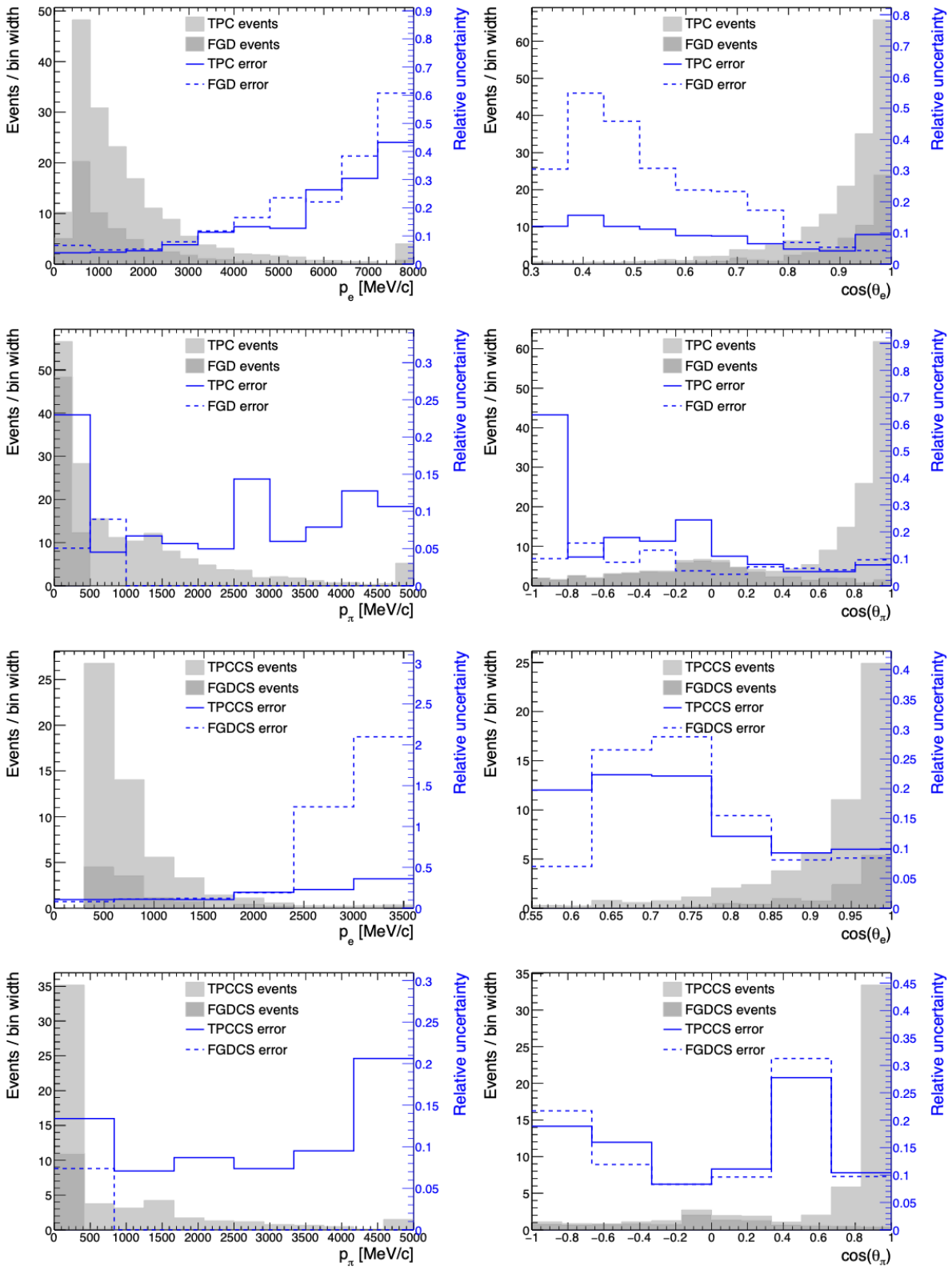

Figure 64. The relative error due to the total detector systematic uncertainty as a function of electron kinematics and pion kinematics. Grey histograms show events of all types which pass the selection cuts organised by sample. The upper four plots show the signal samples and the lower four pots show the control samples.

The total detector systematic uncertainty is also displayed by event type for all selected events in all four samples in table VII. The total systematic uncertainty due to detector systematics is 9.7%.

Topology	Uncertainty [%]
Signal	3.7
ν_e background	5.9
γ background	7.8
μ background	18.1
Other background	17.0
All events	9.7

Table VII. List of the total relative error values for each source of systematic uncertainty due to detector effects split by event type.

6.2 Flux systematic uncertainties

The neutrino beam flux as measured at ND280 is subject to several sources of systematic uncertainty. Hadronic processes such as pion production multiplicity, kaon production and secondary nucleon production are capable of affecting the neutrino beam composition. Other properties such as the horn current and off-axis angle also introduce uncertainty to the process of measuring the neutrino flux at the near detectors. These sources of systematic uncertainty on the FHC flux components are shown as a function of neutrino energy in Fig. 65. Hadronic interactions tend to be dominant for both flavours.

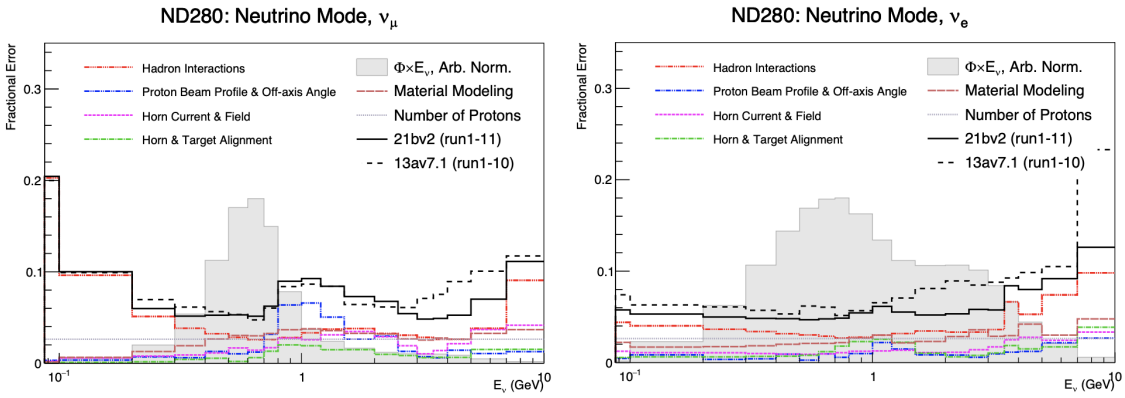

Figure 65. The fractional error as a function of neutrino energy on the ν_μ (left) and ν_e (right) flux from different sources. The solid black line indicates the total uncertainty. These plots are taken from Ref. [119].

The flux uncertainties are also stored as a covariance matrix which holds an uncertainty value for each neutrino flavour binned by the true neutrino energy. This is projected, broken down into each flux component, as one-dimensional distributions as a function of the true neutrino energy of all selected events for this analysis in Fig. 66.

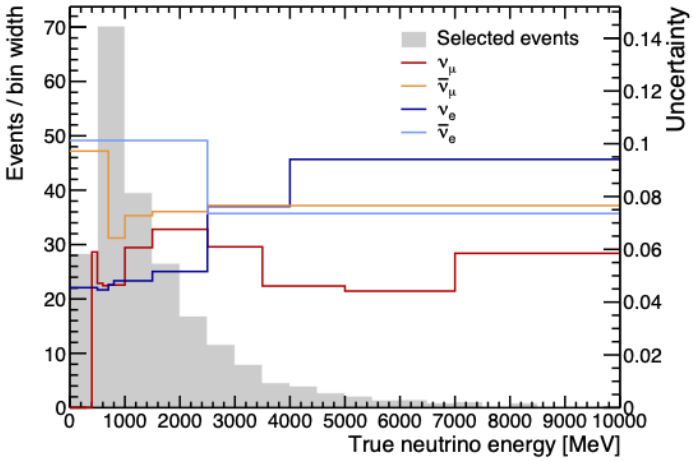

Figure 66. The systematic uncertainties on the neutrino beam fluxes, distinguished by contributions from ν_μ, $\bar{\nu}_\mu$, ν_e and $\bar{\nu}_e$ measurements. The grey histogram shows the true neutrino energy for all events which pass the selection.

The uncertainties on each flux type are shown in table VIII. These are estimated by calculating the average uncertainty across all energy bins used in the plot shown in Fig. 66.

Flux type	Uncertainty [%]
ν_μ	5.9
ν_e	6.4
$\bar{\nu}_\mu$	8.6
$\bar{\nu}_e$	8.7

Table VIII. The overall uncertainties on the flux components of the neutrino beam as measured at ND280.

The flux binning schemes for each neutrino flavour are shown in tables XXI, XXII, XXIII and XXIV in appendix A.2.3. The coarse binning scheme is used because the first two bins of true neutrino energy from the selection outputs are empty as shown in Fig. 66.

6.3 Cross section model systematic uncertainties

Another group of systematic uncertainties is associated with the neutrino interaction cross section models. The models used to generate MC are acknowledged to be incomplete and are subject to continuous refinement. Specific aspects of the cross section modelling implementation by NEUT are assigned to scaling parameters which are constrained with a prior uncertainty. A list of all model parameters used by this analysis and their uncertainties are shown in table IX.

Parameter	Physics	Uncertainty	Units
M_A^{QE}	CCQE	0.06	GeV/c^2
M_A^{RES}	RES/COH	0.10	GeV/c^2
C_5^A	RES/COH	0.10	-
Non-res I_{12} bkg.	RES/COH	0.27	-
FEFQE	FSI	0.31	-
FEFQEH	FSI	0.86	-
FEFINEL	FSI	0.11	-
FEFABS	FSI	0.43	-
FEFCX	FSI	0.31	-
FEFCXH	FSI	0.29	-
Q^2 norm. 1	CCQE	0.11	-
Q^2 norm. 2	CCQE	0.18	-
Q^2 norm. 3	CCQE	0.40	-
SRC norm. C	Other	2.00	-
CCRES π^0 norm.	RES/COH	0.30	-
CCCOH C	RES/COH	0.30	-
CCDIS BY	DIS/Mπ	0.35	-
CC multi-π norm. ν	DIS/Mπ	0.50	-
Nucleon FSI	FSI	0.30	-
p-shell norm. C	Other	0.20	-
s-shell norm. C	Other	0.40	-
CC multi-π DIS BY CORR	DIS/Mπ	1.00	-
CC multi-π TotXSec	DIS/Mπ	1.00	-
CC multi-π shape	DIS/Mπ	1.00	-
CCDIS BY CORR	DIS/Mπ	1.00	-
CCRES E_b C	RES/COH	1.00	MeV
Rein-Seghal Δ decay	RES/COH	1.00	-

Table IX. A table of all cross section model parameters used for this analysis and their prior uncertainty values. The physical meanings of these parameters are discussed on the next page under the bullet point corresponding to the label in the physics column. Generally, each parameter corresponds to different types of events within a particular interaction mode such as CCQE, DIS, RES and COH, or additional processes such as FSI or multiple pion production (Mπ).

Each of the listed parameters controls the shape or normalisation of events of particular interaction types subject to different true kinematics constraints depending on the parameter. The choice of parameters is based on the main backgrounds in the signal samples. These can be grouped into four main categories:

- **CCQE scattering:**
  CCQE scattering interactions are implemented in NEUT using the relativistic global and local Fermi gas models, as well as the Benhar spectral function model [67] with modifications from the Nieves Fermi gas models [120]. There is a single axial mass parameter M_A^{QE} which can modify the shape and normalisation of signal events, corresponding to uncertainty on the dipole form factor. There are also three parameters which act as normalisations for CCQE events in different regions of Q^2 between 0.25 and 1.00 GeV^2.

- **RES and COH pion production:**
  Pion production through RES and COH processes are implemented in NEUT by the Rein-Sehgal model [75]. There are several parameters controlling the shape and normalisation of different RES processes. The M_A^{RES}, C_5^A and Rein-Seghal Δ decay parameters can modify the Rein-Seghal implementation directly. The I_{12} parameter weights the non-resonant backgrounds. The CCRES π^0 norm parameter is also included which is correlated with some of the main background modes involving neutral pion production. Several other parameters are also included, corresponding to COH scattering processes, such as CCCOH C which acts as a normalisation of coherent scattering occurring off a carbon nucleus.

- **DIS and multi-pion production:**
  DIS and multi-pion production processes are more complicated to model; these are implemented in NEUT using the PYTHIA generator [121] which applies structure functions from GRV98 parton distributions with Bodek-Yang corrections. A number of parameters are used to make modifications to this implementation. The CCDIS, CC multi-π DIS, CCDIS by CORR, CC multi-π norm, CC multi-π xsec, CC multi-π shape all control different aspects of the DIS and multi-pion production modelling.

- **FSI:**
  NEUT uses an intra-nuclear re-scattering model to treat final-state pions. The pions are distributed based on nuclei-specific Woods-Saxon potentials with an initial set of kinematics. The pion is moved through the nucleus in steps until absorption or escape

occurs based on calculable interaction probabilities. This is parametrised by six scaling factors all starting with the letters FEF. These all correspond to the probability of pion interactions, such as QE scattering (QE), inelastic scattering (INEL), charge exchange (CEX) and absorption (ABS). These are further distinguished into whether these occur at high (H) or low (L) energies. The pion FSI parameters all have small self-correlations. A further uncorrelated nucleon FSI parameter corresponds to nucleon scattering within the nucleus; this is implemented using the Bertini cascade model [122].

Several other parameters such as the *s*- and *p*-shell normalisation factors do not enter any of these categories; these correspond to aspects of the SF model used to describe the initial-state nucleons.

The evaluation of the uncertainties on each parameter has been performed externally by members of the T2K collaboration, the details of which are outside the scope of this thesis. To propagate the model uncertainties, these parameters are adjusted during the cross section fitting process in section 7. Modifying the weights of all input events during the fitting process is impractical, so a re-weighting technique is used to modify particular events based on truth information. Cross section parameters are modelled as response functions called *splines*. The splines encode the event weight as a function of the cross section parameter values. The function can be interpolated to obtain the event weight for a specific parameter value. A more detailed discussion of how the splines are used is presented in Ref. [123]. For this analysis, each cross section parameter has 1716 spline functions, corresponding to the product of the number of event type categories (13), the number of interaction types (12) and the number of true kinematics bins (11). An example of a typical spline function is shown in Fig. 67.

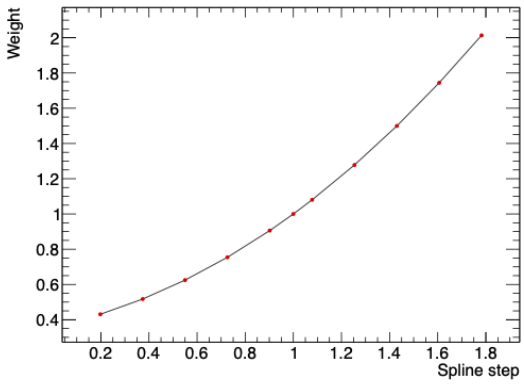

Figure 67. An example of a spline response function which is used to store information about an event weight as a function of arbitrary cross section parameter values.

CHAPTER 7

CROSS SECTION EXTRACTION

This chapter describes how the event selection outputs are used to perform a cross section extraction. The method for obtaining a set of best-fit parameters which best describes the data given the input MC is outlined in section 7.1. The unfolding method requires the selection outputs to be organised into bins which correspond to some of the fit parameters; the binning scheme and how the main results are then obtained are described in section 7.2. An important part of this process is to validate whether the fit model responds as expected to particular sets of purposely-modified MC, referred to pseudo data. A list of pseudo data studies, the main fit metrics and the results of these studies are shown in section 7.3.

7.1 Fitting and cross section extraction

7.1.1 Fit method

The process of obtaining best-fit values for $\hat{N}_i^{\text{sig}}$, as well as Φ and ε, employs a binned maximum log-likelihood method. This methodology is outlined in several recent ND280 cross section measurements including those in Refs. [88, 89]. This entails iteratively varying a group of *template* and *nuisance* parameters such that they best describe the input dataset by minimising the total χ^2_{tot} between the data and MC. The template parameters are weights which directly correspond to the number of signal events in a particular true kinematics bin. There are three sets of nuisance parameters which correspond to the systematic uncertainties associated with the ND280 detector, the neutrino beam flux and cross section models. These systematic parameters are each uniquely proportional to different combinations of the selected events.

The number of signal and background events for a particular binning scheme are supplied as inputs, as well a set of three covariance matrices which describe the correlations between the nuisance parameters. The fitting process yields a set of best-fit parameters $\vec{\theta}$, as well as the uncertainties and correlations between each parameter. The best-fit parameters maximise the likelihood function $\mathscr{L}$ for a given input dataset $\vec{y}$,

$$\mathscr{L}\left(\vec{y};\vec{\theta}\right) = \mathscr{L}_{\text{stat}}\left(\vec{y};\vec{\theta}\right) \times \mathscr{L}_{\text{syst}}\left(\vec{y};\vec{\theta}\right). \tag{71}$$

This corresponds to a minimisation of the total chi-square, χ^2_{tot}, which is given by

$$\chi^2_{\text{tot}} = -2\ln\mathscr{L}_{\text{stat}} - 2\ln\mathscr{L}_{\text{syst}}. \tag{72}$$

This expression contains two terms, (i) the *statistical* term, $-2\ln\mathscr{L}_{\text{stat}}$, which incorporates the statistical uncertainty contribution due to the intrinsic data-MC agreement, and (ii) the *penalty* term, $-2\ln\mathscr{L}_{\text{syst}}$, which increases if systematic uncertainty parameters are moved away from their nominal values. The statistical term is a modified Poisson likelihood ratio

$$-2\ln\mathscr{L}_{\text{stat}} = \sum_{j}^{\text{bins}} 2\left(\beta_j N_j^{\text{exp}} - N_j^{\text{obs}} + N_j^{\text{obs}}\ln\frac{N_j^{\text{obs}}}{\beta_j N_j^{\text{exp}}} + \frac{\left(\beta_j - 1\right)^2}{2\sigma_j^2}\right), \tag{73}$$

where N_j^{exp} is the predicted rate of events derived from MC, N_j^{obs} is the number of observed events, β_j is the Barlow-Beeston scaling parameter, σ_j^2 is the statistical uncertainty on the predicted MC event rate and j indicates the true bin index. The expression for $\mathscr{L}_{\text{stat}}$ has been modified from a standard Poisson likelihood ratio to account for the statistical uncertainty associated with finite MC using the Barlow-Beeston method [124]. The scaling parameter is given by

$$\beta_j = \frac{1}{2}\left(-\left(N_j^{\text{exp}}\sigma_j^2 - 1\right) + \sqrt{\left(N_j^{\text{exp}}\sigma_j^2 - 1\right)^2 + 4N_j^{\text{obs}}\sigma_j^2}\right). \tag{74}$$

In the limit of infinite statistics, $\beta_j \to 1$ and $\sigma_j \to 0$ and the expression reduces to the standard Poisson likelihood ratio. The systematic penalty term is given by

$$-2\ln\mathscr{L}_{\text{syst}} = \sum_{p}\left(\vec{p} - \vec{p}_{\text{prior}}\right)\left(V_{\text{cov}}^{\text{syst}}\right)^{-1}\left(\vec{p} - \vec{p}_{\text{prior}}\right), \tag{75}$$

where $\vec{p}$ is a vector containing all of the systematic parameters, $\vec{p}_{\text{prior}}$ holds the nominal values for these parameters and $V_{\text{cov}}^{\text{syst}}$ is the covariance matrix which encapsulates the error of each systematic parameter and any correlations between these parameters.

The fitting procedure assigns a free parameter with normalisation coefficient c_i to each true kinematics bin; these can be changed such that they increase or decrease the signal rate in the truth bin. The procedure iterates and changes the free parameter weights, while analysing the propagation to the reconstructed bins by comparing this with the data distribution. The fitting software [125] optimises this such that the set of c_i and nuisance parameter values minimises the χ^2_{tot}. The set of minimised values are then used to calculate the number of signal events in the truth bins which best describes the data. The free parameter weights c_i, or *template weights*, are given by

$$N_i^{\text{exp, sig}} = c_i N_i^{\text{MC, sig}}, \tag{76}$$

where event rate in the j^{th} bin is

$$N_j^{\text{exp, sig}} = \sum_i^{\text{true}} c_i N_i^{\text{MC, sig}} t_{ij}, \tag{77}$$

here, t_{ij} is the detector smearing matrix from MC events. The overall number of events in reconstructed bin j is given by the sum of all signal and background (bkg) events,

$$N_j^{\text{exp, tot}} = \sum_i^{\text{true}} \left(c_i N_i^{\text{MC, sig}} + \sum_k^{\text{bkg}} N_{ik}^{\text{MC, bkg}} \right) t_{ij}. \tag{78}$$

The index k runs over all background categories. The nuisance parameters for all systematic uncertainty sources are also accounted for in the form of additional weight factors, which re-weight the number of expected reconstructed events as

$$N_j^{\text{exp}} = \sum_i^{\text{true}} \left[c_i \left(N_i^{\text{MC, sig}} \prod_a^{\text{model}} w(a,\vec{x}) \right) + \sum_k^{\text{bkg}} N_{ik}^{\text{MC, bkg}} \prod_a^{\text{model}} w(a,\vec{x}) \right] t_{ij} d_j \sum_n^{E_\nu} v_{in} f_n. \tag{79}$$

Note the index i runs over the template parameters which correspond to the true kinematic variable bins, while j runs over the equivalent bins for reconstructed kinematic variables. Various terms in Eq. (79) also contain the weight information of different sources of systematic uncertainty:

- The detector weights d_j coefficients re-weight the number of events in reconstructed bins j for all samples. This has a covariance matrix which is supplied and describes the correlations between reconstructed sample bins.
- The flux weights f_n and v_{in} re-weight events in a particular true energy bin n which will have corresponding true bins i. This also has a covariance matrix encapsulating the

correlations between different flux modes at ND280.

- The $w(a,\vec{x})$ terms re-weight events corresponding to a particular cross section parameter which is assigned to all events with a particular event type category, underlying interaction type and set of true kinematic variables. This is also supplied with a covariance matrix describing the correlations between model systematic parameters.
- The smearing matrix t_{ij} accounts for detector smearing when comparing events in true bin i and reconstructed bin j.

The values of d_j, f_n and $w(a,\vec{x})$ have nominal values of one and a particular initial uncertainty. The values for c_i are also nominally one, but these have no prior uncertainty, meaning they are the easiest to move during minimisation. The calculations which produce the covariance matrices corresponding to detector, flux and cross section model systematic uncertainties are discussed in more detail in section 6.

The minimisation of the χ^2 function is performed using Minuit2 [126] with the MIGRAD and HESSE algorithms. MIGRAD explores the parameter space to find the minimum of the χ^2 function, while HESSE uses the finite differences method to calculate the matrix of second derivatives around the minimum. This second derivatives matrix is then inverted to yield the covariance matrix of the fit parameters. The output of the fitting software is a vector of the best-fit parameters, their uncertainties and correlations. The rate of events in each true bin is then given by

$$N_i^{\text{exp, sig}} = \sum_j^{\text{reco}} \left(c_i N_i^{\text{MC, sig}} \prod_a^{\text{model}} w(a,\vec{x}) \right) (t_{ij})^{-1} d_j \sum_n^{E_\nu} v_{in} f_n. \tag{80}$$

An efficiency correction, target and flux normalisation is then applied to calculate the flux-integrated cross section from the number of events in Eq. (56).

7.1.2 Cross section extraction

The best-fit parameters and uncertainties obtained from the fitting process are then used to calculate the three-dimensional cross section in each true bin. The function which describes how the three-dimensional cross section depends on the best-fit parameters is not known, so the cross section uncertainties are propagated using numerical methods. The fitting process produces a post-fit covariance matrix, Σ, which encapsulates the uncertainties of all best-fit

parameters, $\vec{\theta}_f$, and their correlations. This post-fit matrix is Choleksy decomposed

$$\Sigma = LL^*, \tag{81}$$

where LL^* is the Choleksy decomposition. Then $\vec{\theta}_f$ is varied by adding a unit Gaussian throw of random numbers, $\vec{r}_t$, multiplied by the Cholesky decomposition. The result is a random variation of the post-fit parameters distributed in accordance with the post-fit covariance matrix,

$$\vec{\theta}_t = \vec{\theta}_f + (L \times \vec{r}_t)\,. \tag{82}$$

A large number (N_t) of randomly-generated parameter throws, $\vec{\theta}_t^{N_t}$, is used to explore the likelihood space associated with Σ. For all cross section studies in this analysis, $N_t = 5000$ is used. The three-dimensional cross section is then calculated for each $\vec{\theta}_t^{N_t}$ and the cross section covariance matrix, which is associated with the uncertainty on the cross section, is calculated by

$$V_{ij} = \frac{1}{N_t}\sum_t \left[\left(\frac{d\sigma}{dx}\right)_{t,i} - \left(\frac{d\sigma_{\text{best}}}{dx}\right)_i\right]\left[\left(\frac{d\sigma}{dx}\right)_{t,j} - \left(\frac{d\sigma_{\text{best}}}{dx}\right)_j\right], \tag{83}$$

where $d\sigma$ is the i^{th} cross section value for throw t which has values between $1 < t < N_t$. The $d\sigma_{\text{best}}$ term is the best-fit cross section value and V_{ij} is the ij^{th} element of the covariance matrix. The value x represents the three-dimensional product of all input kinematic variables, $x = p_e \cos\theta_e p_\pi$. The remaining parameters such as the flux, efficiency and number of targets are also varied as part of the random throwing of $\vec{\theta}_f$.

The output is a set of three-dimensional best-fit cross sections and their uncertainties. The projection methods to produce the one-dimensional differential and total cross section results are outlined in section 7.2.2 which is discussed after the full analysis binning is established.

7.2 Binning

7.2.1 Binning optimisation

In order to perform the cross section measurement, the kinematics phase space is divided into three-dimensional bins based on the true particle kinematics. Separate values of the ν_eCCπ^+ cross section are calculated in each bin are integrated to produce the main cross section results. There are several considerations required for constructing an appropriate binning scheme;

- Given the very low event rates expected from the MC, each bin should contain a similar number of signal events when projected to the one-dimensional distributions of true observables. This ensures each bin has reasonable sensitivity to signal events and to ensure stable minimisation.
- The efficiency values within a particular bin should not vary substantially (greater than $\sim 10\%$) to reduce model dependence.
- Bin widths should not be finer than the detector resolution.

In the full selection output with no restrictions in the kinematic phase space, there are 109 expected true signal events in total with the full data POT. A binning scheme which has two bins for each of the three kinematic variables is used, which corresponds to a total of eight in-phase space (INPS) bins. There are also three out-of-phase space (OOPS) bins in which the signal purity is particularly low, or the TPC pion PID performance encounters issues. In these OOPS regions, a cross section value will not be reported, but the template parameters corresponding to these are still part of the minimisation process. In total, there are 11 true bins to be used for the overall fit and these are listed in table XVI in appendix A.2. The bin edges all lie within the phase space constraints outlined in section 4.2.2.

The true binning scheme is visualised on plots of the electron kinematics phase space in Fig. 68. This shows the template parameters which correspond to the INPS regions and indicates how many signal events these each correspond to.

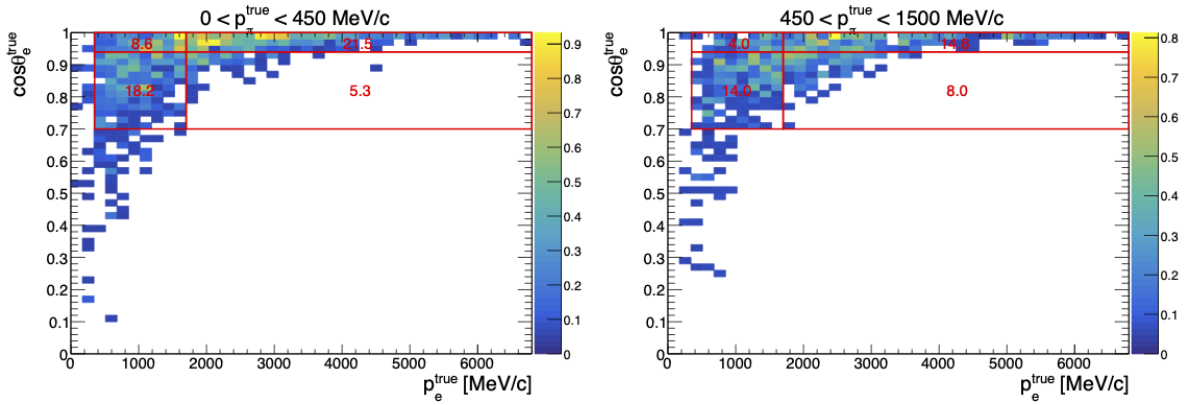

Figure 68. The true binning scheme for the INPS region imposed on the true electron phase space for the lower p_π bin (left) and the upper p_π bin (right). The red regions indicate the bin edges in electron kinematics and the number is the true signal event rate.

The efficiency corresponding to each truth bin is shown in Fig. 69. As shown, the efficiency

is generally between 23-35% for the INPS regions.

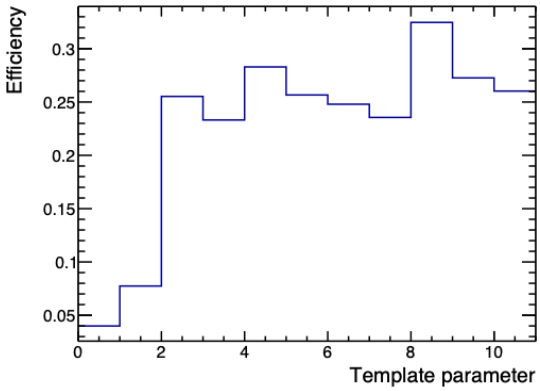

Figure 69. The efficiency for all truth space bins. The template parameter indices correspond to the true bin indices listed in table XVI.

The phase space constraints apply to all true and reconstructed bins. The intermediate truth space bin edges were optimised by aiming to distribute the same number of signal events per bin when projecting down to one-dimensional true kinematic distributions.

There are also 11 bins for each reconstructed sample. The same procedure for optimising the binning scheme was used for the reconstructed samples. In these cases, the binning constraints are less important, provided the reconstructed events have true events which map to bins with non-zero entries. Each reconstructed sample also has several OOPS bins with the same boundaries as the true binning scheme. The reconstructed binning schemes are unique for each sample to account for differences in the reconstruction performance and the distributions of events. For the FGD sample, the upper bin edge on the second p_π bin is set to 450 MeV$/c$ as all Michel electron pion events are contained within this limit. The upper limit is set to 1500 MeV$/c$ for the TPC sample which is the approximate value at which the true particles in the MC are more likely to be protons than pions. The control sample bins have the same boundaries as the signal sample bins, however the FGD control sample has a higher upper limit on p_π of 1500 MeV$/c$. One of the OOPS bins was removed from the TPC control sample as it contained zero expected events which led to problems with the minimisation process.

The full list of bins for each combination of reconstructed electron and pion kinematics for the signal and control samples is shown in tables XVII and XVIII, XIX and XX in appendix A.2.

7.2.2 Projections

The cross section extraction stage of the fit produces a three-dimensional cross section as a function of the template parameters. To convert these to meaningful physics results, the cross sections σ_i in each truth bin of index i need to be summed over and weighted according to the bin width. The differential projection along electron momentum is given by the sum of σ_i for the INPS bins ($i > 3$) while multiplying by the bin width in the remaining two variables, $\Delta\cos\theta_e$ and Δp_π,

$$\left(\frac{d\sigma}{dp_e}\right)_j = \sum_{i=4}^{11} \sigma_i \Delta\cos\theta_{e,i} \Delta p_{\pi,i} \quad \text{where} \quad \begin{cases} j=1, & i=4,6,8,10 \\ j=2, & i=5,7,9,11 \end{cases} \tag{84}$$

The equivalent projection for electron angle is

$$\left(\frac{d\sigma}{d\cos\theta_e}\right)_j = \sum_{i=4}^{11} \sigma_i \Delta p_{e,i} \Delta p_{\pi,i} \quad \text{where} \quad \begin{cases} j=1, & i=4,5,8,9 \\ j=2, & i=6,7,10,11 \end{cases} \tag{85}$$

Similarly for pion momentum,

$$\left(\frac{d\sigma}{dp_\pi}\right)_j = \sum_{i=4}^{11} \sigma_i \Delta p_{e,i} \Delta\cos\theta_{e,i} \quad \text{where} \quad \begin{cases} j=1, & i=4,5,6,7 \\ j=2, & i=8,9,10,11 \end{cases} \tag{86}$$

The total flux-integrated cross section is instead given by summing over all bin indices and multiplying by the entire three-dimensional bin widths

$$\sigma = \sum_{i=4}^{11} \sigma_i \Delta p_{e,i} \Delta\cos\theta_{e,i} \Delta p_{\pi,i}. \tag{87}$$

7.3 Fit validation

The fitting process and results are validated using *pseudo data studies*. These studies involve supplying purposefully-modified MC as data to the fitting software. The fitter then attempts to minimise the difference between the pseudo data and MC by iteratively adjusting the template and nuisance parameters as previously described in section 7.1. The main results are are then checked for problems and indications of statistical significance.

7.3.1 Fit metrics

Each study is performed using the fitting software [125] with the default MIGRAD strategy with an effective distance-to-minimum tolerance of 2×10^{-3}. Fitter performance is quantified by calculating the χ^2 values between post-fit parameter histograms and the nominal or pseudo data histograms. For the fitting process, the χ^2 expression is

$$\chi^2_{\text{fit}} = 2\sum_{i=1}^{N}\left(N_i^{\text{fit}} - N_i^{\text{obs}} + N_i^{\text{obs}}\ln\frac{N_i^{\text{obs}}}{N_i^{\text{fit}}}\right). \tag{88}$$

Here, N_i^{fit} is the expected event rate in bin with index i and N_i^{obs} is the observed event rate in the (pseudo) data in the same bin. This measures the statistical difference between the predicted and measured results during the fitting procedure. For the cross section extraction, a different definition of χ^2 is used. This is

$$\chi^2_{\text{xsec}} = \sum_{i=1}^{N}\left(\sigma_i^{\text{fit}} - \sigma_i^{\text{true}}\right) V_{\text{fit}}^{-1}\left(\sigma_i^{\text{fit}} - \sigma_i^{\text{true}}\right), \tag{89}$$

where there are N cross section bins, σ_i^{fit} is the post-fit cross section in the i^{th} bin and σ_i^{true} is the true cross section in the same bin. The covariance matrix V_{fit} encapsulates the correlations between fit parameters.

For each of the χ^2 metrics, the p-values are calculated using the ROOT function `TMath::Prob(`χ^2`,` $ndof$`)` [118], where χ^2 is the total fit χ^2 for the fit metric, or the total three-dimensional cross section χ^2. The value of $ndof$ is 32 for the fit χ^2 or 11 for the three-dimensional cross section. The p-values in both cases should not be smaller than 0.05, otherwise it would represent an unlikely statistical fluctuation of the nominal MC given the fit model. This scenario would warrant further investigation.

7.3.2 Pseudo data studies

Pseudo data studies can be broadly categorised into three groups:

- *Closure studies* - basic studies which test the response of the fitting software to simple re-weightings.
- *Coverage studies* - many random statistical and systematic fluctuations are generated to explore the parameter space.

- *Stress studies* - tests which use different underlying physics models or otherwise push the software to its limits.

The closure tests are listed in the upper section of table X. The lower section covers the stress tests and further studies which are usually motivated by the behaviour of different physics models or studies performed at other experiments. For all studies, the p-values for the fit and cross section are listed.

Name	Description of pseudo data	p_{fit}	p_{xsec}
Asimov	The nominal MC.	1.00	1.00
Stat. fluc.	Poissonian fluctuations of the nominal MC.	0.55	0.11
Stat. & syst. fluc.	Poissonian fluctuations of the nominal MC and randomly-thrown nuisance parameters.	0.64	0.08
Enhanced signal	All signal events are re-weighted by $+20\%$.	1.00	1.00
Enhanced DIS	All DIS events re-weighted by $+20\%$.	1.00	1.00
Enhanced flux	All events and the best-fit flux integral are re-weighted by $+20\%$.	1.00	1.00
Inflated γ bkgrd.	In-FGD1 γ events are re-weighted by $+50\%$.	1.00	0.99
Deflated γ bkgrd.	In-FGD1 γ events are re-weighted by -50%.	1.00	0.99
Alt. generator	MC generated using GENIE [61].	0.99	0.77
Low Q^2 SPP	$Q^2 < 0.7$ GeV^2 CC1π RES events suppressed using results from Refs. [127, 128].	1.00	0.99
SPP adversarial	$p_\pi < 0.3$ GeV$/c$ CC1π events suppressed.	1.00	0.99
RS to Martini 1π	Alternative pion production model [129].	1.00	0.99
Alt. π kinematics	Alternative pion production model.	1.00	0.99
Low E_ν excess	$E_\nu < 1.25$ GeV events re-weighted by $+100\%$.	1.00	0.99

Table X. List of pseudo data studies conducted as part of fit validation. The description column contains a brief explanation of the pseudo data. The p-values for the fit and cross section result are also listed. The upper part covers the closure and coverage tests, and the lower part covers the stress tests. Note that the p-values for studies involving statistical fluctuations are for one random seed only.

As shown, the fit p-values are close to one for the vast majority of studies, indicating that the fit is able to effectively minimise the pseudo data-MC agreement. The fitter performs worse for studies involving statistical fluctuations, but the fit p-values are above 0.05 in each case. The cross section p-values are also generally close to one, meaning the measured cross section values are close to the true cross sections. The main exceptions are, again, the statistical studies and also the alternative event generator study, the former of which have p-values near 0.1; this only represents one specific statistical fluctuation. To explore the range of p-values that can be expected from a large number of statistical fluctuations, coverage studies were performed using

1005 random seeds. The main results of the coverage studies are shown in Fig. 70.

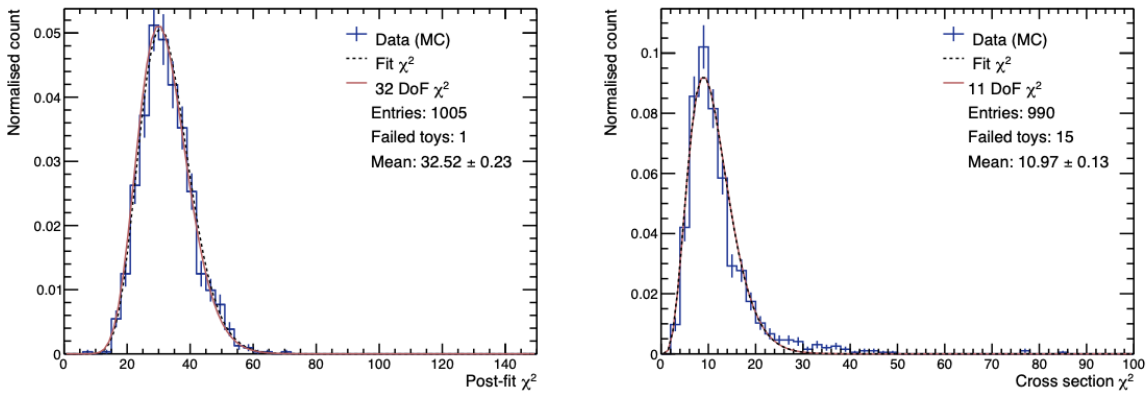

Figure 70. Distributions of the post-fit (left) and cross section (right) χ^2 values for 1005 fits with statistical and systematic uncertainty fluctuations enabled. The blue histogram shows the pseudo data distribution, the black line shows the χ^2 fit to this histogram, and the red lines show the theoretical χ^2 distribution for the annotated number of degrees of freedom.

As shown, the measured distributions of χ^2_{fit} and χ^2_{xsec} closely follow the distributions for the expected number of degrees of freedom in both cases. Failed toys are defined when the χ^2 value from either study exceeds the maximum value on the x-axis or if the fit fails to converge. The failure rates are very low, 0.09% and 1.5% for the fit and result respectively.

Plots of the cross section results for the closure studies and physics-motivated tests are shown in Figs. 71 and 72 respectively. These show the calculated cross sections compared to the nominal Asimov configuration results as well as the fractional biases which are defined as the difference between the measured and true cross sections divided by the measured cross section uncertainty,

$$\text{Fractional bias} = \frac{\sigma^{\text{meas}} - \sigma^{\text{true}}}{\Delta\sigma^{\text{meas}}}. \tag{90}$$

Generally the fractional biases are small for all pseudo data studies with values between ± 0.5 in all cases except for the alternative neutrino event generator study. This pseudo data study has larger bias, particularly in low pion momentum and high electron momentum. This may be because the control samples generated using GENIE have a notably lower ν_eCC-other component, meaning the control samples are slightly less representative of the main backgrounds. The p-values and projected results indicate no issues with any of the pseudo data studies.

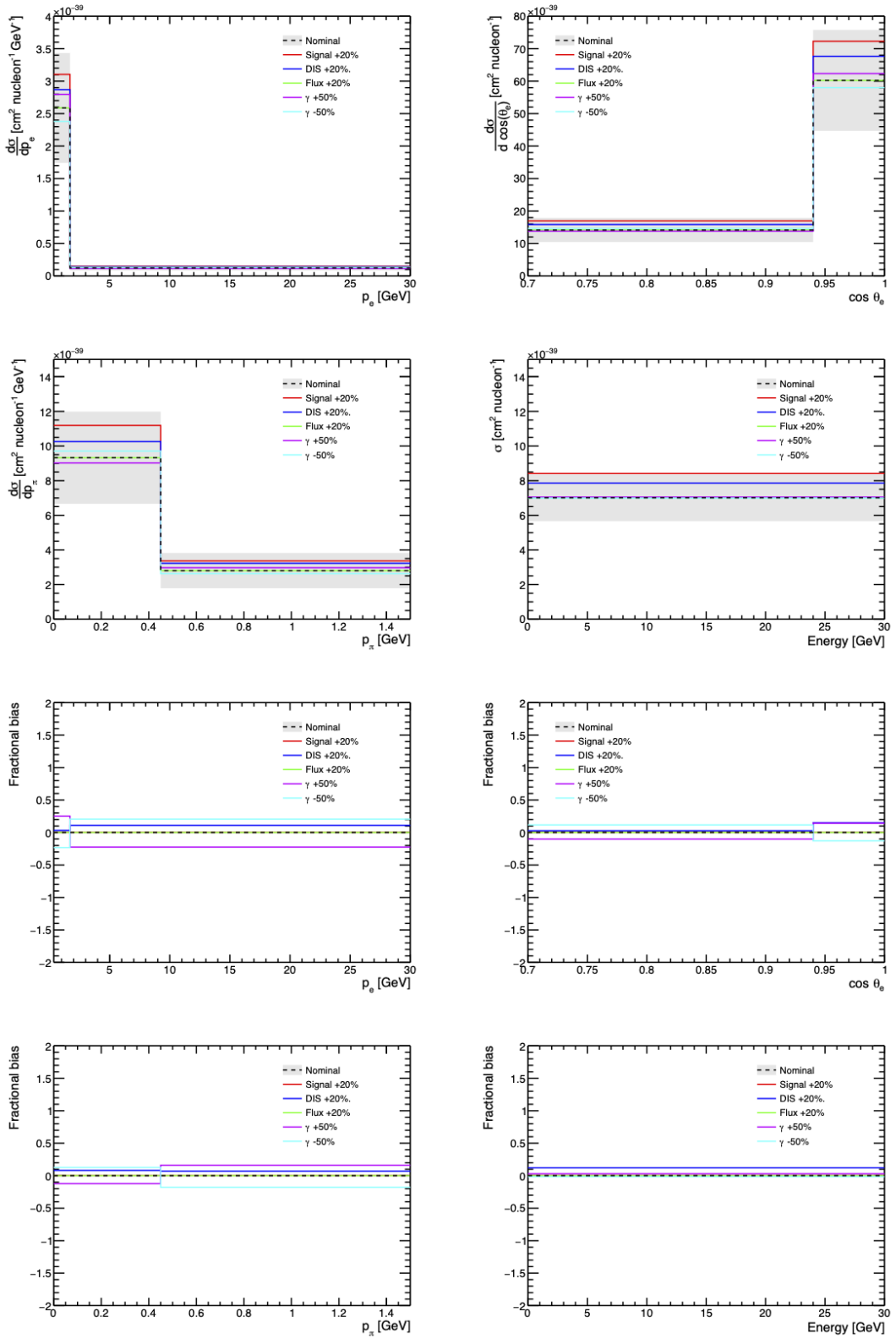

Figure 71. The cross section results for all closure studies. The upper four plots show the cross section values. The lower four plots show the fractional bias between the true and measured cross sections.

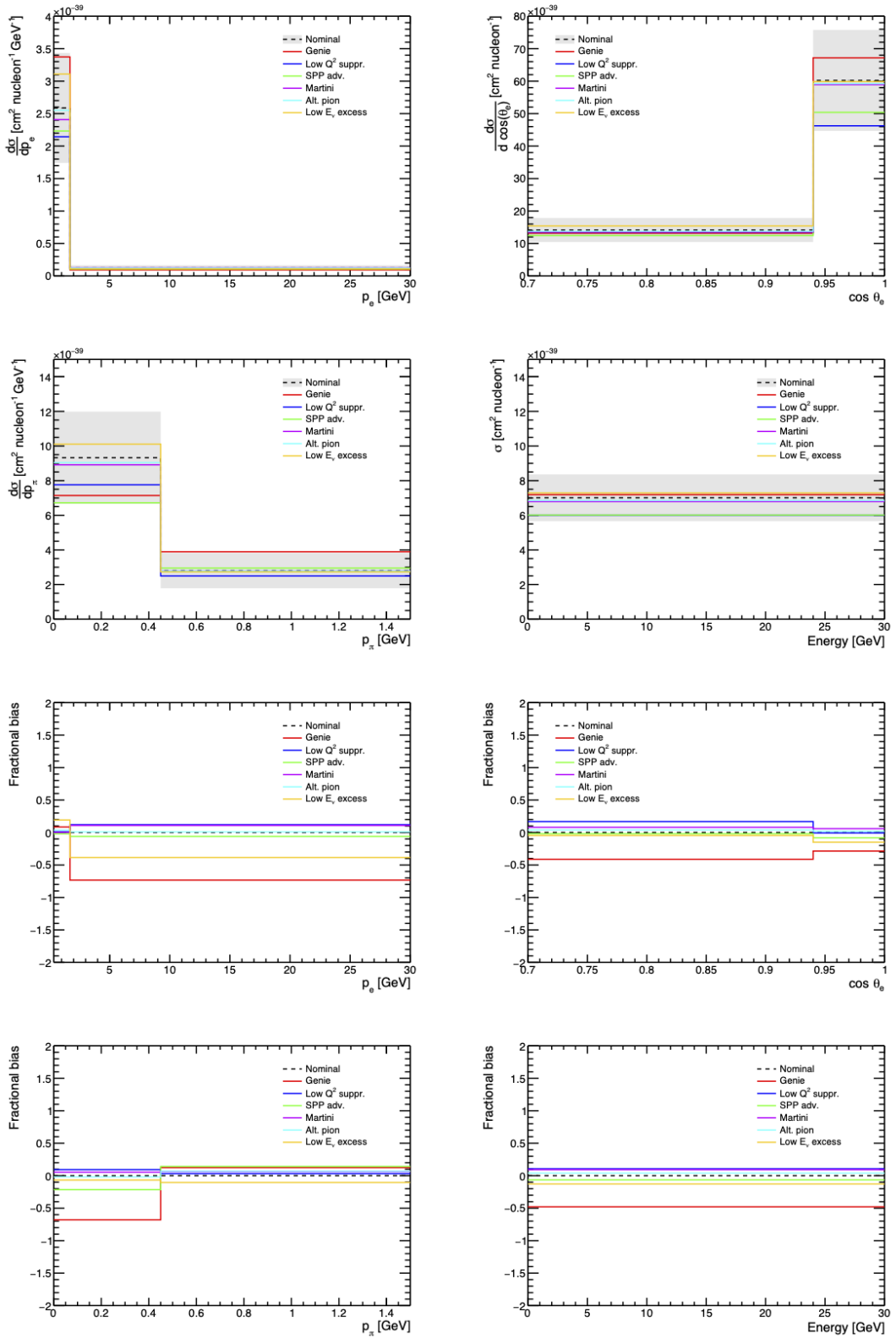

Figure 72. The cross section results for all stress tests and physics-motivated studies. The upper four plots show the cross section values. The lower four plots show the fractional bias between the true and measured cross sections.

CHAPTER 8

RESULTS

Plots showing the nominal MC event rate for both signal samples as a function of E_{rec}^{Δ} are presented in Fig. 73. The TPC sample exhibits no notable event rate excesses. However, the FGD sample does see a 3σ excess in the lowest energy bin which corresponds to neutrino energies of 0-500 MeV. The signal purity in this bin is less than 5%, so it is not possible to determine whether the event excess is associated with the signal or poorly-understood backgrounds. A perfectly analogous comparison with the event rate in the $1\,R_e + 1$ d.e. sample at Super-K is not possible due to the large photon and other backgrounds. It is probable that the OOFGD- and OOFGDFV-γ or other backgrounds contribute most to this excess given that they constitute $\sim$50% of the events in this bin.

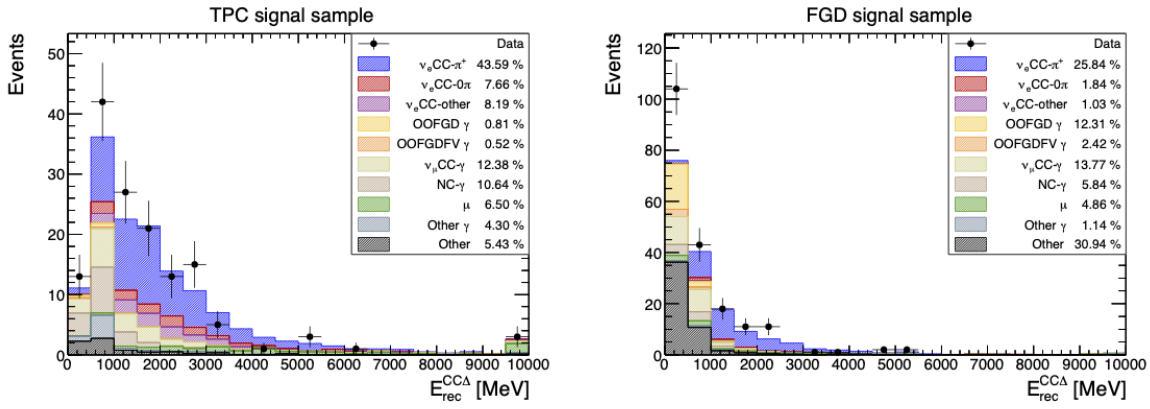

Figure 73. Signal sample histograms of the neutrino event rate as a function of reconstructed neutrino energy assuming CCΔ kinematics. Note that these histograms show the pre-fit MC event rates.

Using the nominal inputs, the fit using real data was performed with the same parameters

used for the pseudo data studies. The nominal and post-fit NEUT event rates, as well as the data event rates, are shown by sample in the three-dimensional reconstructed binning schemes in Fig. 74.

The post-fit event rates generally agree very well with the data. The agreement is slightly poorer in the more statistically-limited control samples, but the post-fit χ^2 values are smaller than the number of degrees of freedom in each case and do not exhibit statistically significant discrepancies. The fit has a p-value of 0.50 which indicates that the data represents a likely statistical fluctuation of the nominal MC within the expectations of the fit model. In most bins, the MC under-predicts the data and so the post-fit event rates generally increase by between 5 and 20%.

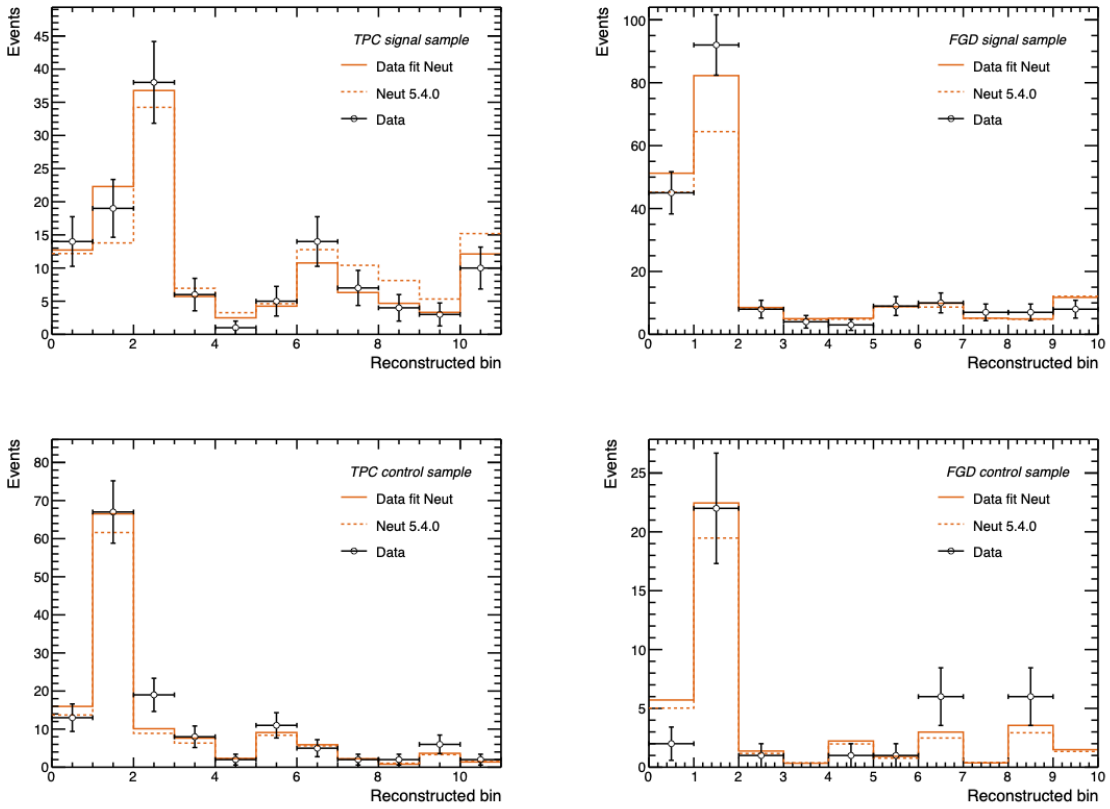

Figure 74. The nominal and post-fit number of reconstructed events in the three-dimensional binning scheme for each sample from the data fit. The binning indices used for these plots are listed by sample in appendix A.2.

The responses of the template and nuisance parameters are shown in Fig. 75. As the

nominal MC marginally under-predicts the data, most parameters increase moderately during the fitting process. The minimisation process also favours reducing some cross of the section parameters associated with final-state interactions. All nuisance parameters variations are within $\pm 50\%$ and all cover the nominal parameter values within their uncertainties. One of the OOPS template parameters (bin 1) increases substantially, but the uncertainty on this is also large. This bin almost exclusively contains OOFGD-γ events which tend to be poorly modelled and so the minimisation process attempts to shift this parameter more readily than the INPS or lower statistics OOPS template parameters. The parameter responses are generally similar to those found when studying the pseudo data results and no unexpected behaviour is observed.

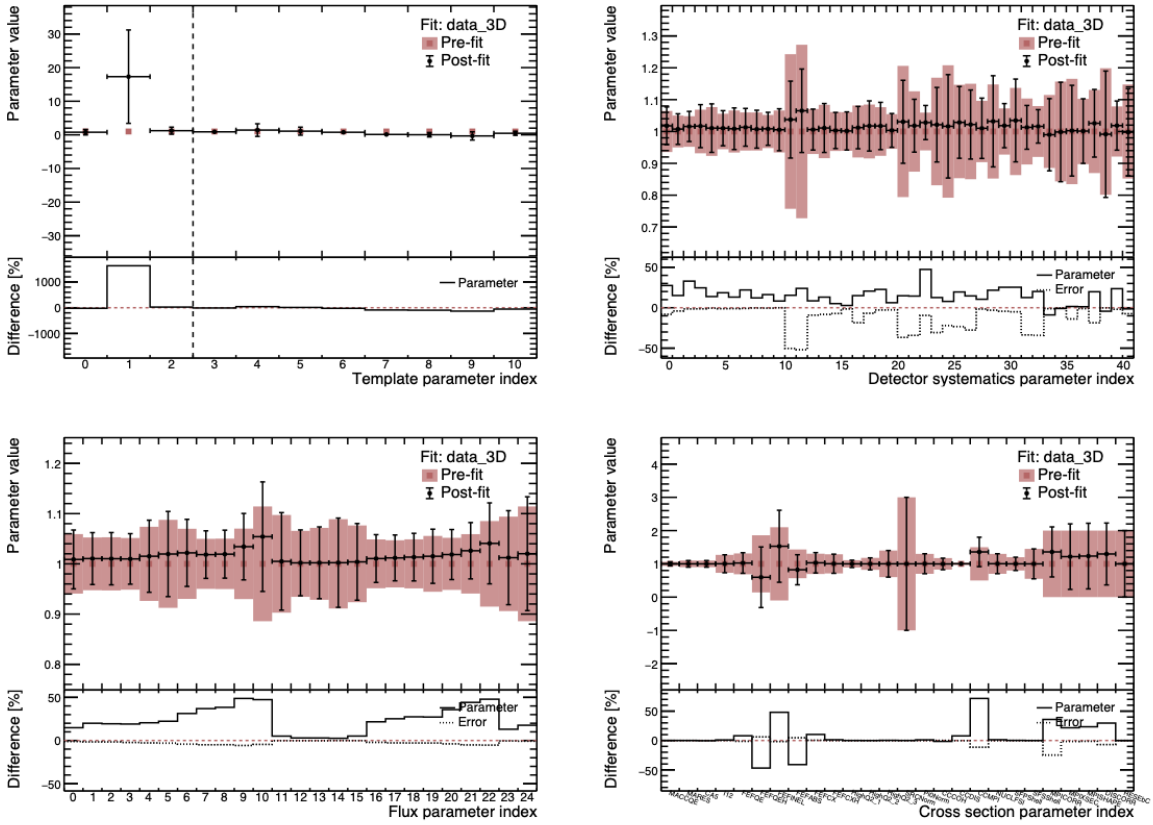

Figure 75. The template and nuisance parameter values and uncertainties for the data fit. The lower plots show the fractional difference between the pre-fit and post-fit parameters.

The total flux-integrated and differential cross sections as a function of particle kinematics results are presented in Fig. 76. The measured cross sections are generally lower than predicted by the nominal MC in most bins. This is particularly noticeable for the higher pion momentum bin result which is more than 2σ away from the NEUT prediction. The main exception to

this trend is the low pion momentum bin which agrees within 1σ of both event generator predictions.

The cross section results for all other bins are all within 2σ of the nominal NEUT predictions; the disagreement with GENIE is greater in all bins as this generator predicts a $\sim$20% uniformly higher cross section. The total flux-integrated cross section result is

$$[5.04 \pm 0.94(\text{stat.}) \pm 0.73(\text{syst.})] \times 10^{-39} \text{ cm}^2 \text{ nucleon}^{-1}. \quad (91)$$

The flux-integrated cross section is also lower than both the NEUT and GENIE predictions by 1.6σ and 2.9σ respectively.

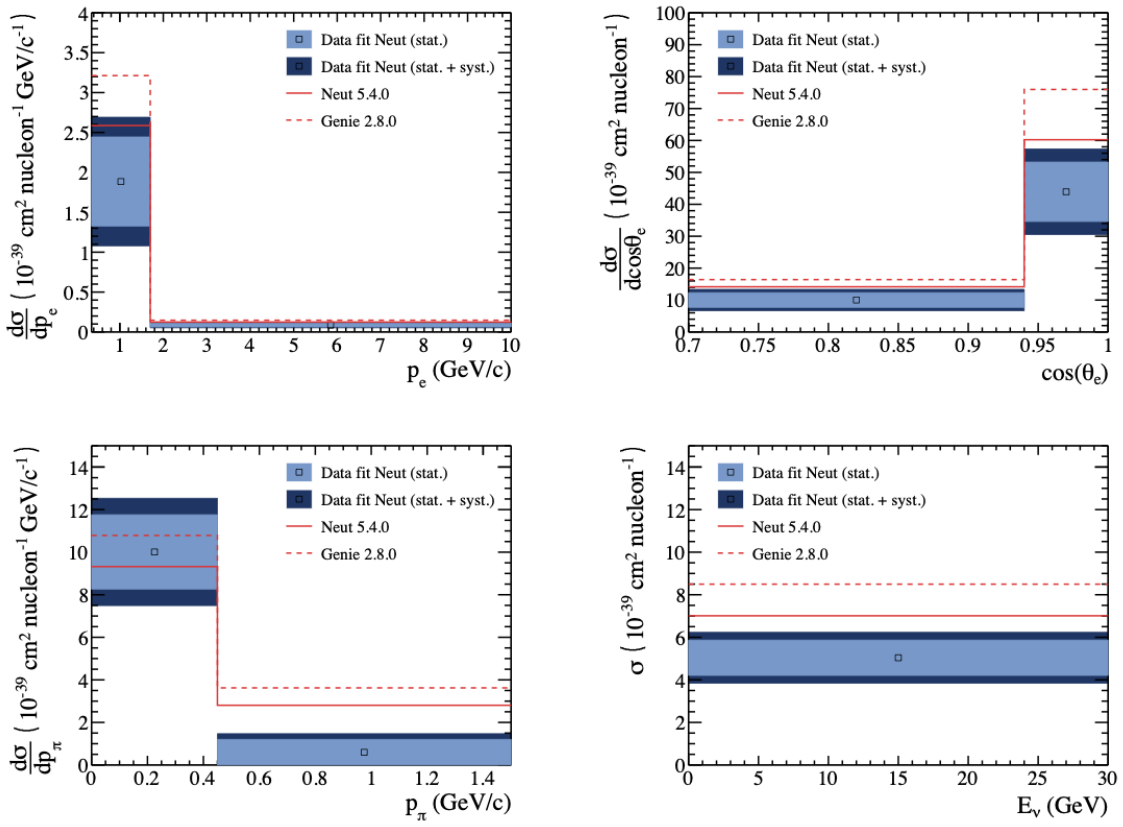

Figure 76. The one-dimensional and total flux-integrated cross section results for the data fit comapred to the NEUT and GENIE predictions. Note the second p_e bin extends to 30 GeV but is restricted to 10 GeV in the plot for clarity.

The p-value for the three-dimensional cross section is 0.43 which suggests this data is a likely fluctuation of the nominal MC within the model constraints.

The uncertainty on the total flux-integrated cross section value, broken down by the source of uncertainty, is shown in table XI. The cross section model uncertainty is marginally dominant, but the overall statistical uncertainty dominates the precision threshold measurement.

Source	**Error**
Detector	5.6%
Flux	6.8%
Cross section	7.8%
Total systematic	11.7%
Total statistical	16.3%

Table XI. The systematic and statistical uncertainty contributions to the overall cross section error.

This work represents the first measurement of ν_eCCπ^+ interactions on a carbon target; it is also the most recent ν_e analysis involving ND280 using data. Given the relative flux of electron neutrinos compared to muon neutrinos, this demonstrates the advanced capabilities of ND280 in selecting sub-dominant interactions. The results appear to be reasonable, but the measurement uncertainties are dominated by the limited statistics for associated with this analysis. It is hopeful that the next-generation ν_eCCπ^+ analysis will be able to have access to a greater number of events and be able to probe beyond the phase space boundaries of this measurement. This would offer a more meaningful comparison with the event excesses seen in other T2K datasets.

A greater number of events would also likely facilitate a four-dimensional fit, providing shape information on the cross section as a function of pion angle. The PID methods being developed in the upgraded ND280 detector should ideally focus on two main areas to improve this analysis: (i) better photon-signal discrimination at low energy and (ii) address proton-pion PID overlap at high pion momentum. Scope for further work could also include dedicated control samples for the particular muon and ν_e backgrounds seen in these results, but the development of these control samples was limited by the very low statistics associated with this analysis. With more data, an isolated pion track sample could also be introduced and it may be the case that a sample of this type would be useful, given the low expected event rate for the given amount of POT. Nevertheless, these results represent another milestone in studying ν_e interactions to high precision and may offer input for neutrino oscillation studies in future. This work can also serve as a benchmark for the sensitivity of ND280 ν_e studies focused on studying the far detector excesses.

Part III

Optical Calibration Development at Hyper-Kamiokande

INTRODUCTION TO PART III

The final part of this thesis focuses on hardware work conducted in preparation for the Hyper-Kamiokande experiment, which will be referred to as Hyper-K in the remaining sections. An overview of the Hyper-K experiment, discussion of its physics goals and expectations, as well as the current design plans, are presented in chapter 9. Chapter 10 is then dedicated to the optical calibration and the work conducted on the light injection modules. Details about the collimator development are also presented in chapter 10.

CHAPTER 9

THE HYPER-KAMIOKANDE EXPERIMENT

Hyper-K [49] is the next-generation successor experiment to T2K and Super-K. This experiment will utilise the same water Cherenkov technology used to detect neutrinos in Super-K, but the fiducial volume will be significantly increased. With a substantially larger number of sophisticated PMTs, Hyper-K is expected to have enhanced sensitivity to low energy neutrino events on the MeV scale. The detector designs are summarised in section 9.1. The main physics goals of Hyper-K are discussed in section 9.2.

9.1 Experimental set-up

Hyper-K is intended to operate primarily as a long-baseline experiment, using the neutrino beam-line produced at J-PARC, as well as the near detectors, ND280, INGRID and Wagasci-BabyMIND. The ND280 detector and beam power have both been upgraded as described in part II, which will continue to operate as part of T2K phase-II until the remaining Hyper-K detectors are commissioned. The main new detectors in Hyper-K are two water Cherenkov detectors similar to the tank used at Super-K. The far detector is located in the re-purposed Tochibora mine, while a smaller intermediate detector will be located in Tōkai around 1-2 km west of J-PARC. Hyper-K will also be capable of functioning independently of the neutrino beamline as a neutrino observatory, focusing on the detection of neutrinos from natural sources.

9.1.1 Far detector

When constructed, Hyper-K will use the world's largest water Cherenkov tank as the far detector. This will have a height of 64 m and a diameter of 70 m, resulting in a FV five times that of Super-K. A diagram of the Hyper-K experiment is shown in Figure 77.

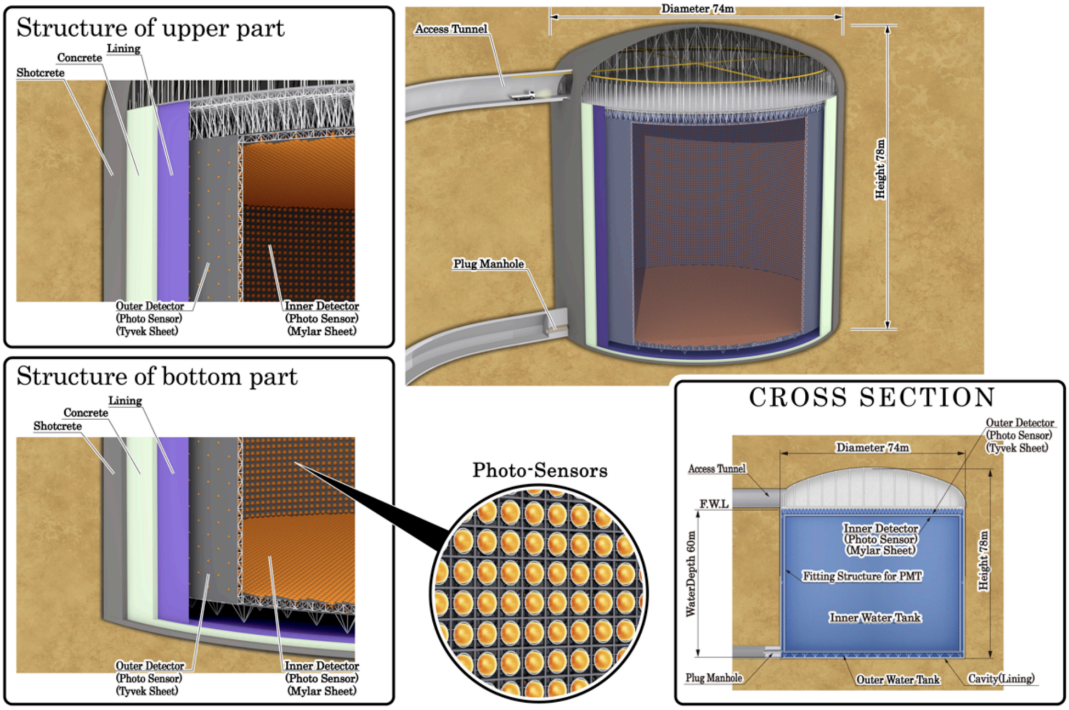

Figure 77. A schematic diagram of the Hyper-Kamiokande far detector. This graphic is taken from Ref. [49].

Hyper-k is also situated 2.5° off-axis with respect to the neutrino beam. It will be situated 0.65 km beneath the peak of Mount Nijuugo-yama. As of March 2024, the dome cavern has been excavated and the vertical excavation is ongoing. Data-taking is expected to commence at some point from 2027.

The far detector will be comprised of two layers of detectors separated by 60 cm walls. The inner detector (ID), similarly to the configuration in Super-K, will contain and surround the inner water tank with a PMT coverage of 40% from 40,000 PMTs. A cylindrical outer detector (OD) will surround the ID. The OD will consist of 6,700 outward-facing PMTs in the outer water tank. As with Super-K, the Hyper-K OD will have the main purpose of constraining the dominant backgrounds which are likely to enter the inner water tank, such as cosmic ray muons. This will also help to determine whether events are ID-contained. Both the ID and OD

are to be mounted on a large cylindrical stainless steel tank, optically separated by a layer of Tyvek. Similarly to Super-K, the inner tank surface will be covered in a layer of Mylar.

The PMTs being designed are also upgrades of those used in Super-K. They are expected to have double the time resolution and better performance when dealing with the main backgrounds such as the dark rate. The ID will make use of 50 cm PMTs, with the possibility of new multi-PMTs being added which should improve the spatial resolution and reduce backgrounds further. Smaller 20 cm PMTs are intended for the OD.

9.1.2 Intermediate water Cherenkov detector

A new intermediate water Cherenkov detector (IWCD) is to be placed around 1-2 km from the neutrino beam source. The IWCD is a cylindrical water Cherenkov detector with height 10 m and diameter 8 m situated within a 50 m deep pit. The elevation of the IWCD and therefore off-axis angle with respect to the neutrino beam will be adjustable between 1-4°. As with the far detector, the IWCD is a Cherenkov tank with inward-facing PMTs with around 40% coverage. The effectively adjustable neutrino flux means IWCD can make analogous measurements of the oscillated neutrino spectrum at the far detector. This can reduce the uncertainties associated with extrapolations between the near and far detectors. IWCD will also be capable of measuring the cross section ratio of muon neutrinos and electron neutrinos on water, as the purity of $\nu_e(\bar{\nu}_e)$ is enhanced at particular off-axis angles. It is also possible that IWCD may be able to offer insight into sterile neutrino searches by measuring $\nu_e(\bar{\nu}_e)$ appearance as a function of the off-axis angle.

9.2 Physics goals

9.2.1 Neutrino oscillation measurements

One of the main goals of Hyper-K is to measure the PMNS mixing matrix parameters to precisions exceeding those reached by T2K and NOvA. In particular, the CP phase δ_{CP} is expected to be measured more precisely with complementary datasets from atmospheric and accelerator neutrinos using $\overset{(-)}{\nu}_e$ appearance studies. Measurements of δ_{CP} are likely to indicate or exclude CP violation to 4σ and eventually 5σ. The magnitude of δ_{CP} should be measurable to within 23° and the CP violation coverage to 5σ is likely to exclude over half of the parameter space. The uncertainties on measurements of the mixing angles θ_{13} and θ_{23} are expected to be improved as well from enhanced $\overset{(-)}{\nu}_e$ appearance and $\overset{(-)}{\nu}_\mu$ disappearance studies respectively.

The mass hierarchy should also be determinable to 4σ and Δm^2_{32} will be measurable.

9.2.2 Astrophysical neutrino studies

Hyper-K will also function as the most sensitive probe of natural neutrinos from astrophysical origins, which can be used as tests for various cosmological and supernova models. The energy threshold for neutrino detection is expected to be lowered to the MeV scale, which allows for solar and supernova neutrinos to be detected individually as they produce interactions in the Cherenkov tank on an event-by-event basis. It is also likely to be able to measure the diffuse supernova background for the first time.

9.2.3 Nucleon decay searches

Additionally, Hyper-K has other physics goals unrelated to neutrino phenomenology. In particular, Hyper-K will be able to search for evidence of proton decay. Some BSM theories predict the proton lifetime to be $\mathcal{O}(10^{35})$ yr or longer. Protons are predicted to decay via $p^+ \to e^+ + \pi^0$, where the neutral pion then decays by the subsequent $\pi^0 \to 2\gamma$ interaction. The resulting signal would be three simultaneous electron-like rings produced from the same event, or two rings with a reconstructed π^0 mass within a certain range. Other BSM theories predict proton decay through $p \to \bar{\nu} + K^+$, which Hyper-K is also expected to be sensitive to. Hyper-K will be able to use improved neutron tagging techniques to advance studies of the main backgrounds and final state interactions most relevant to nucleon decay signals. After approximately 10 years of operation, Hyper-K should be able to increase the upper limit on the proton decay time by a further order of magnitude, therefore ruling out some BSM extension theories.

CHAPTER 10

COLLIMATORS FOR OPTICAL CALIBRATION

This chapter describes the main hardware work contributing to this thesis, which was the design and testing of a new collimator for calibration purposes relating to the Hyper-K far detector. An overview of the light-injection system is detailed in section 10.1. The current collimator design is presented in section 10.2. The apparatus used to test the collimator is shown in section 10.3. Details of the analysis software for processing the collimator outputs into measurable quantities are provided in section 10.4. Finally, a summary of the optical performance results is presented in section 10.5.

10.1 The light-injection system

The light-injection system is a set of optical components intended to be placed in specific locations around the ID and OD of the Hyper-K Cherenkov tank, as well as the IWCD. The main optical devices to be mounted on each module are a diffuser and a collimator. The diffusers are designed to produce a wide-angle ($\theta = \pm 40^{\circ}$) beam to uniformly illuminate a large number of PMTs. The collimators are designed to inject a narrow-angle ($\theta < 4^{\circ}$) beam of light to illuminate a small area of PMTs on the other side of the Cherenkov tank. Each light-injection module will be connected to optical fibres which inject pulses of light at particular positions with chosen wavelengths. The light-injection modules will be placed at on the walls and base of the Cherenkov tank such that the relevant properties can be studied across all parts of the far detectors.

These instruments will serve important calibration purposes, such as measuring the timing, gain and response of the PMTs of all three sets of PMT arrays in the Cherenkov tanks. The collimator will specifically allow for measurements of water scattering processes and determinations of properties such as attenuation length as a function of tank depth. The diffuser intends to measure aspects of the PMT responses, such as uniformity, timing and angular consistency. An understanding of these processes and properties is essential to correctly calibrate the far detectors; it will allow the detectors to operate continuously while monitoring scattering processes and PMT responses during data-taking periods which was not possible with Super-K. This thesis chapter focuses largely on the work conducted for development of the collimators.

A total of 70 collimators will be produced; the number of collimators corresponding to each detector of Hyper-K is listed in table XII. It is possible that the features of the collimator, such as the targeted opening angle, will vary between detectors given their different dimensions. A tunable opening angle is therefore a desirable feature of the collimators.

Detector	**Number**
HK far inner detector	36
HK far outer detector	16
IWCD inner detector	12
Spares	6
Total	70

Table XII. A table showing the number of collimators intended to be produced for each of the water Cherenkov detectors for Hyper-K.

An early version of the light-injection modules was deployed in the Super-K far detector for testing the feasibility of installing such devices and for performing early studies using real data. These were installed at five locations in Super-K corresponding to different depths within the Cherenkov tank. The results from this deployment gave indications of the performance of the collimators and diffusers. In particular, one of the collimators demonstrated degrading performance over a long-term duration, which may be due to a leak. The designs of the collimators and diffusers are ongoing subject to suggestions from the calibration experts at Hyper-K, as well as the wider Hyper-K review process.

10.2 Design

10.2.1 Physical and optical requirements

The collimators are designed such that scattering and attenuation measurements can be performed at Hyper-K. A narrow-angle beam is preferred for these purposes because the amount of scattering and absorption tends to scale with the volume of water traversed by the injected photons. The extents of these processes can be determined by comparing simulation studies of light scattering in water with the PMT hits as measured when photons are injected. A narrow beam also means the uncertainties associated with determining the scattered beam centre are minimised.

The collimators are carefully designed with several primary considerations. Each collimator must:

- Illuminate the same number of PMTs, ensuring measurements do not experience positional dependence within the detector.
- Exhibit the same optical properties across the entire visible electromagnetic spectrum so that scattering processes which may change the photon wavelength do not substantially affect the beam behaviour.
- Be capable of withstanding high pressures ($\sim$700 kPa) for durations of $\mathcal{O}(10\,\mathrm{yr})$ which corresponds to the expected operation times of Hyper-K.

The area of PMTs illuminated by the collimator is a function of the opening half-angle θ. Assuming a constant beam expansion rate, a collimated beam with initial radius r_0 at a distance of d will have an effective area

$$A(d) \simeq \pi \left(r_0 + 2d\tan\theta\right)^2, \tag{92}$$

where, for Hyper-K, $d \simeq 70$ m. The number of PMTs aimed to be illuminated by the collimator beam was optimised using MC studies of the beam centre reconstruction accuracy. The main study performed quantifies the expected difference in the true beam centre and the reconstructed beam centre in accordance with the PMT set-up planned for Hyper-K. A plot of the beam centre reconstruction residuals in Fig. 78 suggests the optimal opening angle lies between 2.0° and 3.6°. Below 2°, the residuals increase significantly due to asymmetry in PMT coverage. This effect also occurs between 2.5° and 3.2° to a lesser extent before the next ring of PMTs is

reached. The residuals then decrease again as the next layer of PMTs is hit by the beam.

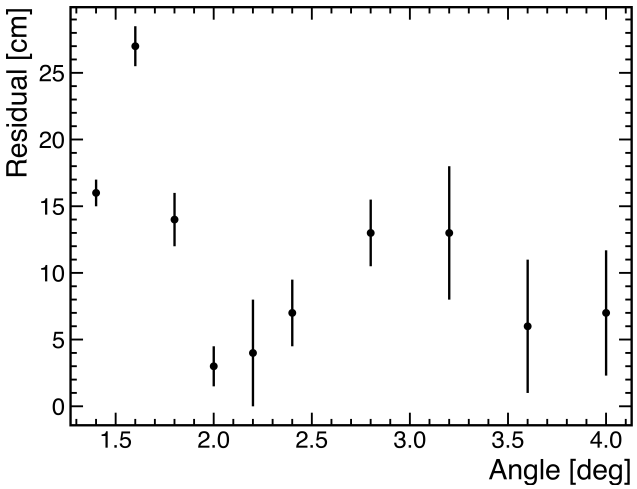

Figure 78. A plot of the beam centre reconstruction residuals, showing the difference between the true and reconstructed beam centre positions for different opening half-angle values. This plot was reproduced from Ref. [130].

A target angle of 2.2° was chosen to minimise the amount of scattered light masked by the direct beam spot. Accounting for the refractive index of water using Snell's law, this implies an optimal opening angle in air of $\sim$ 2.6-2.8°.

The remaining two physics requirements regarding pressure survivability and wavelength invariance are satisfied with the choice of lens and by encasing the optical configuration within a stainless steel waterproof housing unit. These two properties are discussed in the next section as part of the collimator design.

10.2.2 Components and assembly

The collimator is comprised of several main components which will be assembled in a pressure vessel to minimise liquid contamination on the components. The components are acquired from a mixture of custom and commercial sources. The current collimator design consists of three main parts:

- An optical alignment tube containing the collimating optics.
- The external waterproof housing and front-facing window.
- An optical feed-through.

An exploded schematic of these components is shown in Fig. 79.

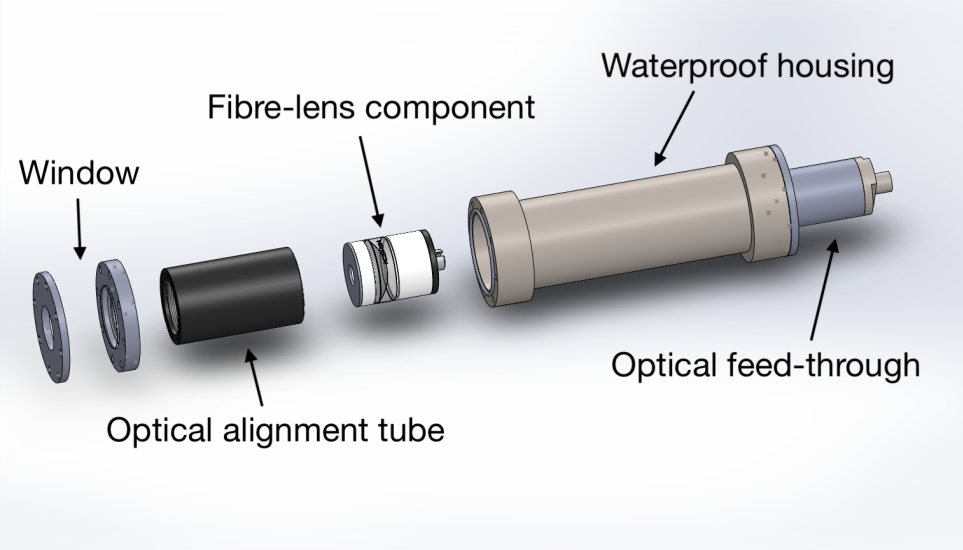

Figure 79. An exploded CAD schematic of the collimator design with main components labelled.

The collimating optics consists of a 1" doublet lens with a focal length of 30 mm and a fibre plate. An 8 mm aperture is placed in front of the lens to ensure the collimator beam profiles have sharp edges. The aperture, lens and fibre plate are separated by perspex spacer tubes which are engineered to ensure the components are kept at particular distances from each other.

The other side of the fibre plate has a patch cord which connects to an internal fibre. The internal fibre is partially coiled around the empty section of the housing and is attached to the optical feed-through. The feed-through will be connected to the input fibres which control the light-injection system. A glass window is held in front of the collimating optics by an additional section of metal housing. A CAD schematic with all components assembled is shown in Fig. 80.

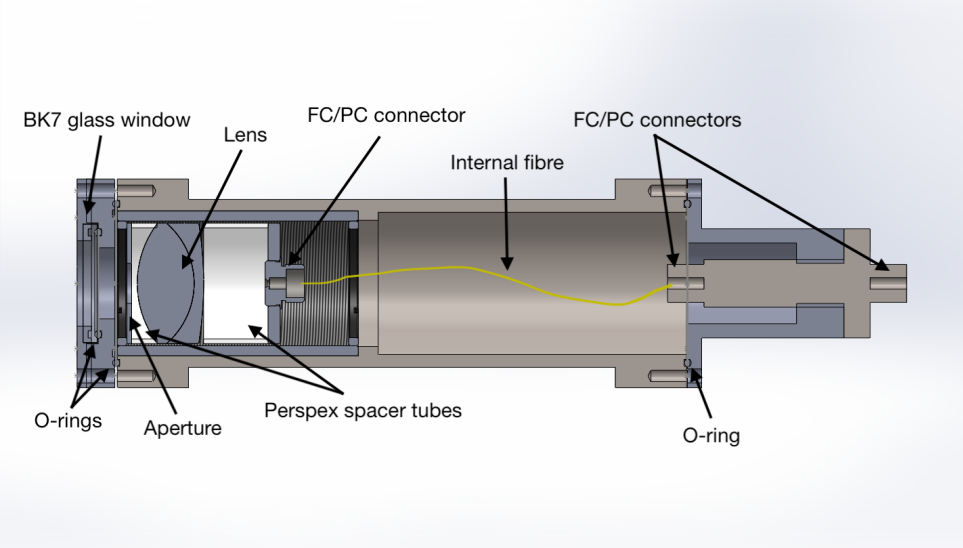

Figure 80. A CAD schematic of the design of an assembled collimator with main components labelled.

The collimating optics is contained within a threaded optical alignment tube; the precise distances between the main components control the beam divergence and profile shape.

An older version of the collimator used a thinner gradient index lens, but this design was superseded as the alignment tolerances were of $\mathcal{O}(10^{-6}\ \mathrm{m})$ which made assembly consistency difficult. One advantage of the doublet lens is that the alignment tolerances are around $\mathcal{O}(10^{-3}\ \mathrm{m})$ which is far more manageable; alignment studies in section 10.5 show that the beam angle generally remains consistent within offsets of around 0.5-1.0 mm and 1.0-4.0 mm parallel and perpendicular to the beam direction respectively.

10.3 Test-stand

10.3.1 Equipment

The collimator test-stand is designed to capture cross-sectional images of the beam produced by collimator prototypes and eventually all collimator models as part of the assembly procedure. The apparatus consists of a SONY ICLE-7M2 camera mounted to three perpendicularly-connected linear stages, allowing for full three-dimensional positional control. A collimator model is mounted on two optical posts and is connected to five LEDs. The LEDs are connected to an external HM7044 power supply and the camera and stages are connected to a computer containing the DAQ software. Three of the LEDs are connected to a wavelength combiner

which allows for different wavelengths to be tested without re-attaching the input fibre.

The input wavelengths used by this test-stand are 340, 365, 395, 505 and 625 nm. The voltage of the power source controls the collimator beam intensity. The test-stand is enclosed within a dark box to eliminate background sources of light. The coordinate system used for measurements defines the z-axis to be parallel to the cylindrical axis of the collimator, and with the positive z direction in the same direction as the beam emitted from the collimator. The y direction is the defined to be the vertical direction and the x axis is oriented to define a right-handed coordinate system. A photograph of the test-stand is shown in Fig. 81.

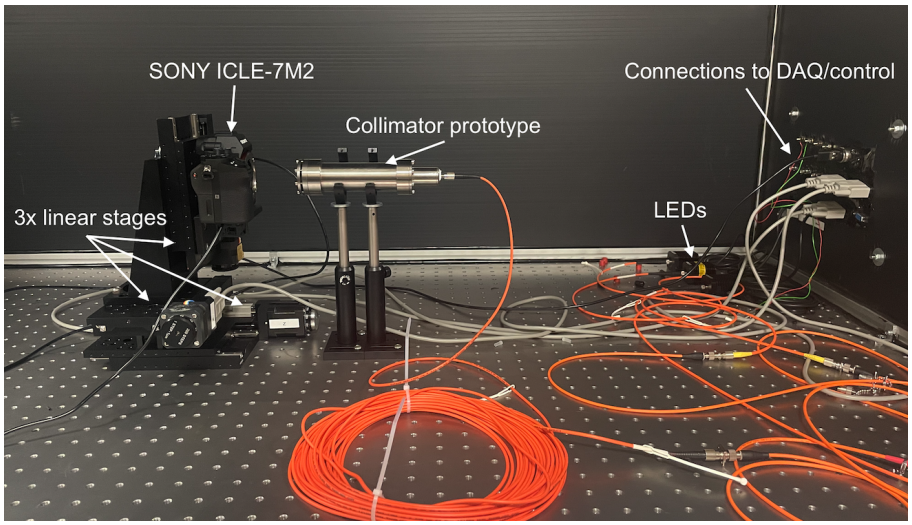

Figure 81. The collimator test-stand with main devices and components labelled. The apparatus is enclosed within a dark box which is closed during operation.

10.3.2 Scanning

To determine the profile and expansion rate of a collimator, information about the beam size at different positions is required. This information is obtained through a scan, during which the camera captures an image of the collimator beam at a particular position using the linear stages. To conduct a typical scan, the DAQ requires several inputs:

- $N_{x,y,z}$ - number of steps along the x-, y- and z-directions.
- $\Delta x, \Delta y, \Delta z$ - the step size along each direction; the step sizes along x and y are typically set to the camera lens size in these directions. The step size along z can be varied depending on the scan type, but is usually $\mathcal{O}(1\text{ mm})$.

- (x_0, y_0, z_0) - the start position of the camera, which is typically chosen such that the beam centre approximately aligns with the chosen start position.
- *Background mode* - defines the combination of steps at which background light is sampled.

Two other quantities relating to the camera are also externally controlled:

- *Shutter speed* - the length of time during which the camera sensors are exposed to light; this is set to 1 s.
- *ISO* - changes to the CCD electronics gain; this is kept at a value of 100.

Together, these quantities effectively control the camera exposure. These values were chosen by checking the images and the noise of collimator profiles.

When a scan is performed, the stages move the camera to the start position (x_0, y_0, z_0) and the camera captures an image. The stages then move the camera to $(x_0, y_0, z_0 + \Delta z)$ and captures another image; this is repeated N_z times until the camera position is $(x_0, y_0, z_0 + N_z\Delta z)$. The camera moves back to the next pair of y- and x-coordinates until $N_x \times N_y \times N_z$ images are captured, with the final position $(x_0 + N_x\Delta x, y_0 + N_y\Delta y, z_0 + N_z\Delta z)$. For most purposes, only one-dimensional scans are necessary and $N_x = N_y = 1$, with N_z images captured in total alongside background images. Three-dimensional scans are necessary if the beam size is larger than the camera aperture at any point during the scan. The camera has an area of 2.39×3.58 cm^2 which is typically large enough for most near-field measurements, but far-field measurements require images to be stitched together. The number of steps along the z-axis should be at least six, however for most scans, 20 steps are used, as a small number of scan positions are likely to have fits which fail when passed through the analysis software.

Background images are captured at different intervals depending on the background sampling mode. The power supply is temporarily turned off automatically by the DAQ. For most studies, background images are captured at the start and end of the scan process. These are captured before the first and last images. The background scan uses the same exposure time used when capturing normal beam images.

The image, background image and (x, y, z) coordinates of each step are stored in an output directory which is then accessible to the analysis software. An image map file stores the locations of each file such that the analysis software can correctly compute the beam divergence. Examples of collimator beam images at different z-axis positions are shown in Fig. 82.

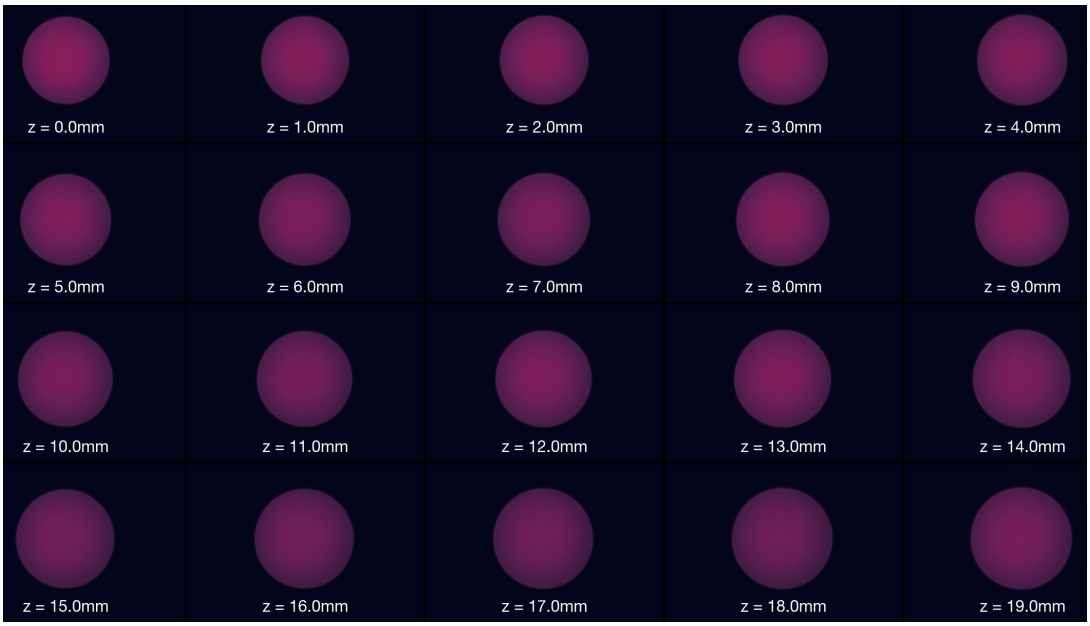

Figure 82. Cross-sectional images of the collimator beam at different z-positions for a typical scan.

10.4 Analysis

A separate analysis software is used to process these images into useful plots for examining the properties of the collimated beam. The process for converting raw camera images into beam radii values involves the following steps:

1. **Background subtraction:**
   The background images are subtracted from each normal image; options are available to subtract average initial and final background images or background images along each step.

2. **Image filtering:**
   A median filter with a circular brush of radius 10 px is used to reduce beam imperfections and sharp discontinuities in the beam profile which may interfere with the subsequent analysis. The filtering process has no significant effect on the beam profile or expansion, but reduces the likelihood of fits failing.

3. **Binarisation:**
   The filtered images are binarised; all pixels are assigned a value of one or zero. The binarisation threshold is set at half of the maximum image intensity; any pixels with intensity above (below) this have a corresponding binarisation of one (zero).

4. **Edge detection:**
   The Canny edge detection algorithm [131] is used to determine the edges of the beam.
5. **Masking:**
   The closest six pixels to the image borders are removed, as bright pixels which tend to appear at the extremities of the camera sensor are capable of interfering with successive steps.
6. **Fitting:**
   The beam is fitted with a circle to measure the radius at the half-maximum intensity. Note that some circular fits may fail and any entries of this type are omitted from the final beam expansion calculations.

The radius of the half-maximum intensity is used to calculate the beam radius r,

$$r = r_0 + d\tan\theta, \tag{93}$$

where r_0 is the initial beam radius, d is the distance along the beam axis and θ is the divergence. Plots of d against $r - r_0$ therefore give the divergence as a function of the gradient m,

$$\theta = \arctan m. \tag{94}$$

The analysis software outputs information on how many fits have failed. The other outputs are accessed by scripts, which load the fit and can produce plots of the horizontal, radial and azimuthal beam profile, as well as the beam expansion rate.

10.5 Optical performance

10.5.1 Expansion and profile

An example of a beam expansion and horizontal profile for a collimator prototype are shown in Fig. 83.

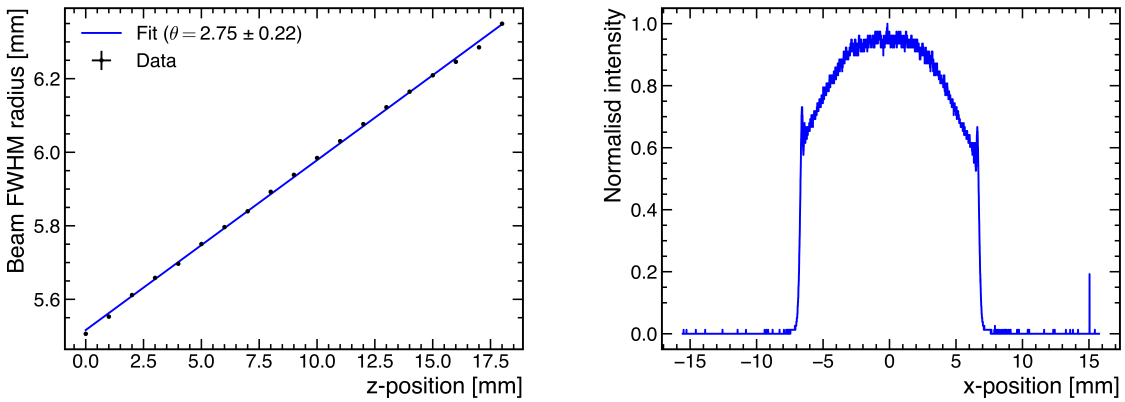

Figure 83. Example plots of the beam divergence (left) and horizontal profile (right) of a typcial collimator scan.

As shown, the beam opening angle is within the desired rangse in air of 2.6-2.8°. The beam profile has a flat central peak which drops off sharply to zero at around ±6 mm. Some notable artefacts include a spike at approximately 15 mm which tends to happen randomly for particular pixels spiking. Furthermore, around the main beam are two small spikes just before the beam intensity drops to zero. These tend to exclusively occur for very near-field measurements and are likely to be related to the collimator beam reflecting off the side of the aperture. This effect tends to disappear with further afield measurements. Generally, the profile and beam expansion closely match the requirements envisioned for deployment in Hyper-K.

10.5.2 Alignment tolerances

One of the main motivations for using a doublet lens is the improved alignment tolerances. To quantify the alignment tolerances of this lens, a simple study was conducted where the components in the collimating optics were mounted on separate posts and small displacements parallel and perpendicular to the beam axis were introduced. The collimator beam was scanned after each displacement and the beam expansion rates were measured. These are shown in Fig. 85.

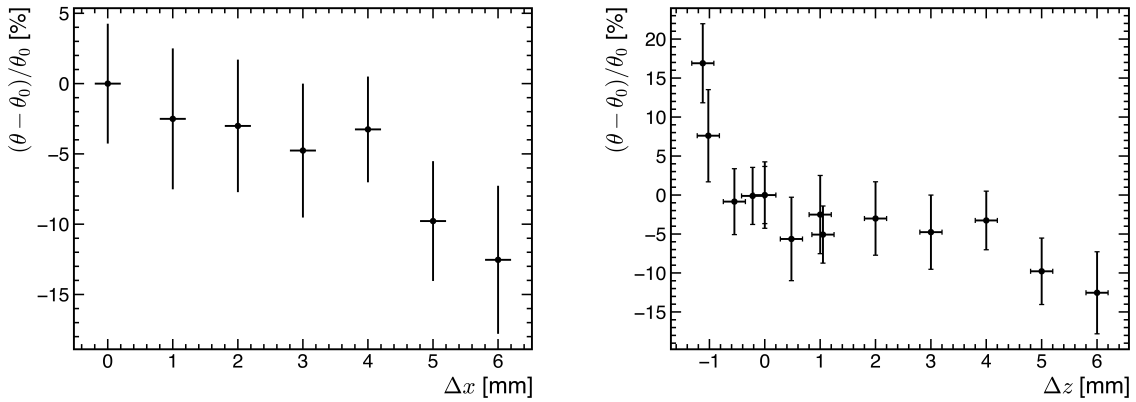

Figure 84. Plots showing the alignment tolerances along the x- and z-directions, where Δx and Δz represent small shifts of the fibre-lens separation in these directions. The x- and z-directions are perpendicular and parallel to the beam axis respectively.

As shown, displacements perpendicular to the beam axis tend to only result in significant deviations in the beam size after around 4 mm. Displacements parallel to the beam axis are more sensitive, and deviations outside of the fit uncertainty tend to occur after displacements of ± 1 mm. These alignment tolerances are still a substantial improvement on the gradient index lens collimators which were a factor of $\sim 10^3$ more sensitive. Alignment accuracies of $\mathcal{O}(1\,\text{mm})$ are much easier to achieve with the available construction tools.

10.5.3 Beam divergences

Studies were conducted to measure the range of beam divergences achievable by varying the fibre-lens separation distance. In this case, the fibre-lens separation was adjusted between 5 and 30 mm and scans were performed. A plot of the beam divergence as a function of the fibre-lens separation is shown in Fig. 85.

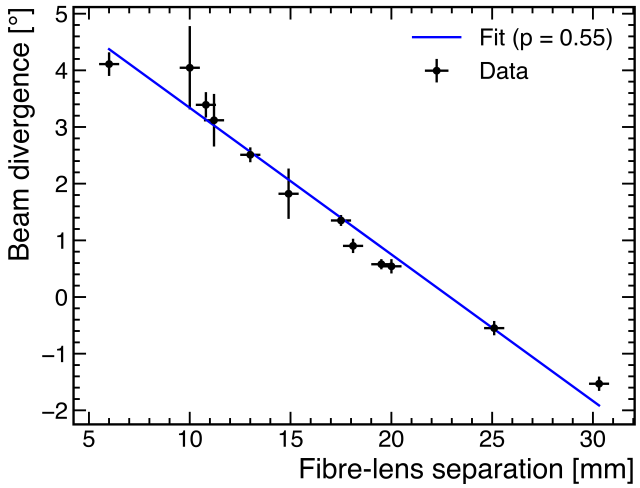

Figure 85. A plot of the beam divergence values obtained as a function of fibre-lens separation.

The opening half-angle demonstrates a linear dependence on the fibre-lens separation. The best-fit function for the data is

$$\theta = 5.926 - 0.259d. \tag{95}$$

This shows that there is significant flexibility in the opening half-angles that can be obtained. The angles range from $\sim 4^\circ$ to -2°. This range easily covers the approximate optimal angle values for the Hyper-K ID. Adjustments of $\mathcal{O}(0.5\text{ mm})$ lead to a change in the opening half-angle of around 0.12°, which allows for mm-level tuning of the collimator divergence.

10.5.4 Wavelength variance

To test the wavelength dependence of the beam behaviour, five LEDs covering much of the visible and start of the ultraviolet range were used. The beam cross-sections were captured using separate scans. The results of this study are shown in Fig. 86.

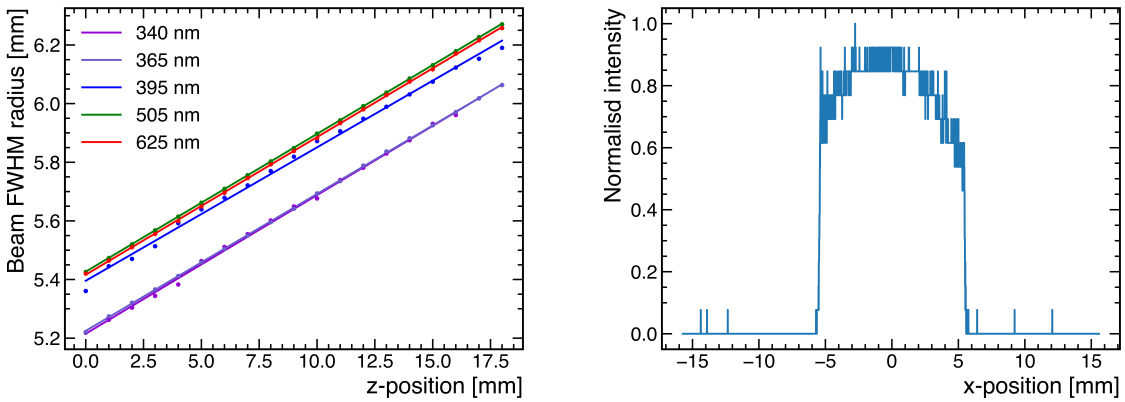

Figure 86. Plots of the beam expansions (left) and horizontal beam profiles (right) for the assembled collimator using different input wavelengths.

The opening half-angle values are listed in table XIII. These are all consistent within the fit uncertainty and are within 1σ of 2.8° in all cases. This demonstrates that the doublet lens sustains wavelength invariance across the visible light spectrum and into the long end of the ultraviolet spectrum which is the most representative of typical Cherenkov photons.

Wavelength	Beam divergence
340 nm	$2.79 \pm 0.22^\circ$
365 nm	$2.78 \pm 0.22^\circ$
395 nm	$2.67 \pm 0.24^\circ$
505 nm	$2.80 \pm 0.22^\circ$
625 nm	$2.80 \pm 0.24^\circ$

Table XIII. A table showing the measured beam divergence values for each wavelength.

The horizontal profiles are also reasonably consistent. The shorter wavelengths are typically noisier as these tend to correspond to dimmer images.

10.5.5 Systematic studies

As part of the internal review process, a number of systematic studies were conducted relating to the collimators. These studies are listed in table XIV. These were typically focused on the expected uncertainties on the beam performance as a result of the assembly procedure. Several other studies were more focused on the test-stand consistency and any variations in the set-up, such as the LED voltage or the angular alignment of the camera with respect to the collimated

beam. In each case, the horizontal profiles and beam divergences were compared with the nominal results.

Study name	Description
Single assembly (i)	Collimating optics tube assembled five times.
Single assembly (ii)	Collimator model fully assembled five times.
Multiple assembly	Five full collimator assembled.
Positional variance	Beam expansion and profile studied with different start positions.
Intensity variance	Beam expansion and profile studied with different voltages.
Angular alignment	Camera rotated on its axis up to 20°.
Long-term consistency	Beam expansion tested after hourly intervals for 48 hr.
Long-term alignment	Beam centre drift tested after hourly intervals for 48 hr.

Table XIV. A table listing all of the systematic studies conducted as part of the internal review process.

10.5.6 Far-field measurements

One of the main recommendations as part of the internal review process was to study the beam profile and divergence using longer distances to assess the beam properties in the far-field. The collimator results so far have typically been within 30 cm of the beam. Far-field measurements have been conducted to perform measurements up to 2 m. Distances longer than this are difficult to test using the current test-stand. Several large mirrors were used and oriented such that the full length of the light enclosure can be used several times over to maximise the camera-collimator distances with the available equipment.

A preliminary set of far-field images is shown in Fig. 87. All images beyond the first z-position required stitching as these exceed the size of the camera aperture. Notably the intensity of the beam image drops off significantly between the first and last z-positions. This makes fitting the last images difficult and the two largest beam images fail; only the first three fits are valid. More work needs to be done to validate findings from this study, but the results give a preliminary indication of the far-field behaviour of the collimator beam. It should also be noted that the background subtraction step was also not yet performed for this study.

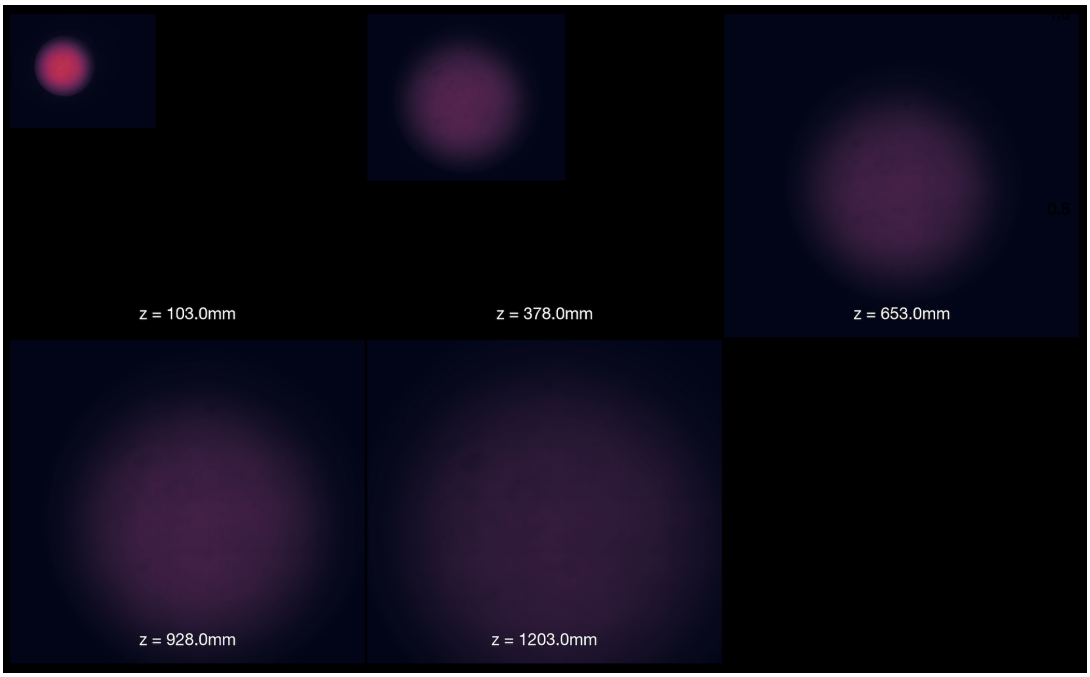

Figure 87. Cross-sectional images of the collimator beam at different z-positions for a preliminary far-field study.

The beam expansion results corresponding to this are shown in Fig. 88. The opening angle is calculated as $2.18 \pm 0.01^\circ$ which is around 20% smaller than the near-field measurements. As already mentioned, the final two fits fail and ideally at least 10 images at different z-positions should be captured to confirm this behaviour.

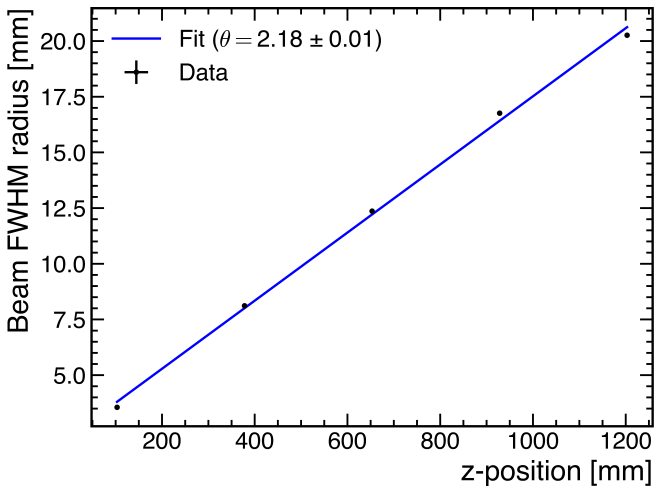

Figure 88. Beam divergence values for the far-field study.

These results suggest that the far-field beam properties are not worryingly different from the near-field measurements. The collimator beam still appears to expand reasonably close to the desired rate and the profiles appear to retain angular uniformity. Further work is required to validate these results.

10.6 Conclusions and next steps

Tests conducted using a doublet lens have yielded promising results for deployment purposes in Hyper-K. There is a degree of flexibility in the design as a result of vastly improved alignment tolerances, and the opening half-angle appears to be tunable between 0-4°. Our collimator design and the documented tests are currently going through an internal review within the Hyper-K collaboration. If similar beam properties are generally seen for far-field studies, it is expected that the design will be approved by our collaborators. The collimator assembly line will then be prepared with the aim to commence construction later this year. The current schedule aims to finish collimator construction by mid-2025. This will be followed by delivery to Japan and attachment to the respective detectors. Hyper-K will then commence data-taking sometime from 2027 and the first results will be obtained within a few years of operation.

Part IV

CONCLUSION

The main focus of this thesis is the completion of the first measurement of the ν_eCCπ^+ cross section on a carbon target. This channel, as measured at the far detector, shows evidence of event rate excesses which may indicate issues with the neutrino-nucleus interaction models used at T2K. As a previously unmeasured cross section, this measurement will help constrain the uncertainties associated with neutrino-nucleus interactions which will become increasingly vital as neutrino oscillation experimentation approaches a precision era.

Although a very challenging measurement to perform, the plentiful and effective particle identification methods at the disposal of ND280 was able to yield a selection with a purity of 60% and efficiency of 20%. Given that fewer than 400 events are expected from the entire operating time of ND280 in comparison to tens of thousands of ν_μ events and the major backgrounds, this is a notable achievement and is a showcase of how much cross section measurements have improved in the last decade.

The total flux-integrated cross sections appear reasonable compared to predictions from neutrino event generators, but reducing the statistical uncertainty is essential to effectively probe neutrino-nucleus cross section models. Improved detector discrimination between electrons and photons should also eventually allow for a full comparison to be made in the low energy phase space of ND280. This would offer insight to ongoing efforts in T2K to address these excesses, particularly whether these are properties of the unique far detector phase spaces.

The secondary focus of this thesis is the development of collimators for light-injection purposes in the next-generation Hyper-Kamiokande detector. The new model based on doublet lenses offers a much more versatile design than the previous collimator model. All tests so far indicate the desired properties are obtained with this design, and further tests should validate the behaviour in the far-field. Deployment of these devices in the far detectors will allow for new measurements of the water scattering and attenuation length to be performed, facilitating identification of any issues associated with the detector calibration. Along with the diffusers, these will play a key role in understanding the detector response and improve the outlook of measurements at Hyper-Kamiokande when data-taking commences in a few years time.

APPENDICES

CHAPTER A

T2K ANALYSIS APPENDICES

A.1 Software and data

The analysis uses a total of 1.16×10^{21} POT in FHC mode, which is all data collected between 2010 and 2013, as well as 2016–2017 in T2K runs 2, 3, 4 and 8. The MC is generated using `NEUT 5.4.0.` [59]. Breakdowns of the total data and MC used for each run period are shown in table XV.

Run	**P0D status**	**MC (10^{21} POT)**	**Data (10^{21} POT)**
Run 2	Air	1.613	0.036
Run 2	Water	1.204	0.043
Run 3	Air	3.076	0.159
Run 4	Air	3.580	0.179
Run 4	Water	3.612	0.170
Run 8	Air	3.846	0.415
Run 8	Water	2.717	0.158
Total	-	19.648	1.161

Table XV. The amounts of data and MC used by this analysis split by ND280 FHC run period and the status of the P0D. The quantification of data and MC is divided by the POT.

Data and MC processing was performed using T2K software production 6T. A POT normalisation factor of 0.059015 is applied to all MC histograms, which corresponds to the ratio of data POT to MC POT.

Information about the cross section extraction tool is which was adapted for this analysis

can be found in Ref. [125].

A.2 Analysis binning

This appendix contains information about the binning schemes for the true kinematics in table XVI and the reconstructed binning by sample in tables XVII, XVIII, XIX and XX. The flux binning is listed in tables XXI, XXII, XXIII and XXIV.

A.2.1 True sample binning

Bin index	p_π	$\cos\theta_{\mathbf{e}}$	p_e
1	0-30000	-1.0-0.70	0-30000
2	0-30000	0.70-1.0	0-350
3	1500-30000	-1.00-1.0	0-30000
4	0-450	0.70-0.94	350-1700
5	0-450	0.70-0.94	1700-30000
6	0-450	0.94-1.00	350-1700
7	0-450	0.94-1.00	1700-30000
8	450-1500	0.70-0.94	350-1700
9	450-1500	0.70-0.94	1700-30000
10	450-1500	0.94-1.00	350-1700
11	450-1500	0.94-1.00	1700-30000

Table XVI. Binning scheme for true electron and pion kinematics. Note the momentum columns have units MeV/c.

A.2.2 Reconstructed sample binning

Bin index	p_π	$\cos\theta_{\mathbf{e}}$	p_e
1	0-30000	-1.0-0.70	0-30000
2	0-30000	0.70-1.0	0-350
3	1500-30000	-1.00-1.0	0-30000
4	0-600	0.70-0.94	350-1200
5	0-600	0.70-0.94	1200-30000
6	0-600	0.94-1.00	350-1200
7	0-600	0.94-1.00	1200-30000
8	600-1500	0.70-0.94	350-1200
9	600-1500	0.70-0.94	1200-30000
10	600-1500	0.94-1.00	350-1200
11	600-1500	0.94-1.00	1200-30000

Table XVII. Binning scheme for true electron and pion kinematics for the TPC sample. Note the momentum columns have units MeV/c.

Bin index	p_π	$\cos\theta_{\mathbf{e}}$	p_e
1	0-30000	-1.0-0.70	0-30000
2	0-30000	0.70-1.0	0-350
3	0-180	0.70-0.95	350-1000
4	0-180	0.70-0.95	1000-30000
5	0-180	0.95-1.00	350-1000
6	0-180	0.95-1.00	1000-30000
7	180-450	0.70-0.95	350-1000
8	180-450	0.70-0.95	1000-30000
9	180-450	0.95-1.00	350-1000
10	180-450	0.95-1.00	1000-30000

Table XVIII. Binning scheme for true electron and pion kinematics for the FGD sample. Note the momentum columns have units MeV$/c$.

Bin index	p_π	$\cos\theta_{\mathbf{e}}$	p_e
1	0-30000	-1.0-0.70	0-30000
2	0-30000	0.70-1.0	0-350
3	1500-30000	-1.00-1.0	0-30000
4	0-600	0.70-0.94	350-800
5	0-600	0.70-0.94	800-30000
6	0-600	0.94-1.00	350-800
7	0-600	0.94-1.00	800-30000
8	600-1500	0.70-0.94	350-800
9	600-1500	0.70-0.94	800-30000
10	600-1500	0.94-1.00	350-800
11	600-1500	0.94-1.00	800-30000

Table XIX. Binning scheme for true electron and pion kinematics for the TPC control sample. Note the momentum columns have units MeV$/c$.

Bin index	p_π	$\cos\theta_{\mathbf{e}}$	p_e
1	0-30000	-1.0-0.70	0-30000
2	0-30000	0.70-1.0	0-350
3	0-180	0.70-0.95	350-1000
4	0-180	0.70-0.95	1000-30000
5	0-180	0.95-1.00	350-1000
6	0-180	0.95-1.00	1000-30000
7	180-1500	0.70-0.95	350-1000
8	180-1500	0.70-0.95	1000-30000
9	180-1500	0.95-1.00	350-1000
10	180-1500	0.95-1.00	1000-30000

Table XX. Binning scheme for true electron and pion kinematics for the FGD control sample. Note the momentum columns have units MeV$/c$.

A.2.3 Flux energy binning

Index	ν_μ energy [GeV]
0	0.0-0.4
1	0.4-0.5
2	0.5-0.6
3	0.6-0.7
4	0.7-1.0
5	1.0-1.5
6	1.5-2.5
7	2.5-3.5
8	3.5-5.0
9	5.0-7.0
10	7.0-30.0

Table XXI. The ν_μ energy binning scheme used for evaluating the flux systematic uncertainties.

Index	ν_e energy [GeV]
0	0.0-0.5
1	0.5-0.7
2	0.7-0.8
3	0.8-1.5
4	1.5-2.5
5	2.5-4.0
6	4.0-30.0

Table XXII. The ν_e energy binning scheme used for evaluating the flux systematic uncertainties.

Index	$\bar{\nu}_\mu$ energy [GeV]
0	0.0-0.7
1	0.7-1.0
2	1.0-1.5
3	1.5-2.5
4	2.5-30.0

Table XXIII. The $\bar{\nu}_\mu$ energy binning scheme used for evaluating the flux systematic uncertainties.

Index	$\bar{\nu}_e$ energy [GeV]
0	0.0-2.5
1	2.5-30.0

Table XXIV. The $\bar{\nu}_e$ energy binning scheme used for evaluating the flux systematic uncertainties.

CHAPTER B

HYPER-K ANALYSIS APPENDICES

B.1 Doublet collimator

Table of the collimator components and vendors:

Component	Vendor	Component ID
Optical alignment tube	ThorLabs	SM1M30
Fiber connector plate	ThorLabs	SM1FC2
Lens	ThorLabs	AC254-030-A-ML
Internal patch fibre	ThorLabs	FG105UCA with FT900Y jacket
Aperture	Custom	-

Table XXV. A table showing the main optical components for the collimating optics, the relevant vendor and component IDs.

BIBLIOGRAPHY

[1] W. Pauli, *Dear Radioactive Ladies and Gentlemen*, *Phys. Today* **31N9** (1978) 27.

[2] M. Witanowski, *Nitrogen n.m.r. spectroscopy*, *Pure Appl. Chem* **37** (1974), 225-233.

[3] E. Fermi, *Sopra lo Spostamento per Pressione delle Righe Elevate delle Serie Spettrali*, *Nuovo cimento* **11** (1934) 157.

[4] F. Perrin, *Structure et Proprietes des Noyaux Atomiques*, *Compt. Rendus* **197** (1933) 327.

[5] F. Reines and C. L. Cowan, *The Reines-Cowan Experiments: Detecting the Poltergeist*, *Los Alamos Sci.* **25** (1997), 4-27.

[6] C. L. Cowan, F. Reines, F. B. Harrison, H. W. Kruse, and A. D. McGuire, *Detection of the Free Neutrino: a Confirmation*, *Science* **124** (1956), 103–104.

[7] S. L. Glashow, *The renormalizability of vector meson interactions*, *Nucl. Phys.* **10** (1959), 107-117.

[8] S. Weinberg, *A Model of Leptons*, *Phys. Rev. Lett.* **19** (1967) 1264.

[9] A. Salam and J. C. Ward, *Weak and electromagnetic interactions*, *Nuovo Cimento* **11** (1959), 568–577.

[10] R. Davis, *Attempt to Detect the Antineutrinos from a Nuclear Reactor by the* $Cl^{37}(\bar{\nu}, e^{-})$ *Reaction* *Phys. Rev.* **97** (1955) 766.

[11] G. Danby, J-M. Gaillard, K. Goulianos, L. M. Lederman, N. Mistry, M. Schwartz, and J. Steinberger, *Observation of High-Energy Neutrino Reactions and the Existence of Two Kinds of Neutrinos* *Phys. Rev. Lett.* **9** (1962) 36.

[12] DONUT collaboration, *Observation of tau neutrino interactions*, *Phys. Lett.* **B504** (2001), 218–224.

[13] The ALEPH, DELPHI, L3, OPAL and SLD Collaborations, the LEP Electroweak Working Group, and The SLD Electroweak and Heavy Flavour Groups, *Precision electroweak measurements on the Z resonance*, *Phys. Rev.* **427** (2006), 257-454.

[14] ALEPH collaboration, *Determination of the Number of Light Neutrino Species*, *Phys. Lett.* **B231** (1989), 519-529.

[15] DELPHI collaboration, *The DELPHI detector at LEP*, *Nucl. Instrum. Methods Phys. Res.* **A303** (1991) 2, 233-276.

[16] L3 collaboration, *The construction of the L3 experiment*, *Nucl. Instrum. Methods Phys. Res.* **A289** (1990) 2, 35-102.

[17] OPAL collaboration, *The OPAL detector at LEP*, *Nucl. Instrum. Methods Phys. Res.* **A305** (1991) 2, 275-319.

[18] A. Blondel, *The number of neutrinos and the Z line shape*, *C. R. Phys.* **3** (2002) 9.

[19] J. N. Bahcall, *Neutrino astrophysics*, *Cambridge University Press* (1989).

[20] L. C. Stonehill, J. A. Formaggio, and R. G. H. Robertson, *Solar neutrinos from CNO electron capture*, *Phys. Rev.* **C69** (2004) 015801.

[21] B. T. Cleveland, T. Daily, R. Davis, J. R. Distel, K. Lande, C. K. Lee, P. S. Wildenhain, and J. Ullman, *Measurement of the solar electron neutrino flux with the Homestake chlorine detector*, *Astrophys. J.* **496** (1998), 505-526.

[22] R. Davis, D. S. Harmer and K. C. Hoffman, *Search for Neutrinos from the Sun*, *Phys. Rev. Lett.* **20** (1968) 1205.

[23] Super-Kamiokande collaboration, *Measurement of the Solar Neutrino Energy Spectrum Using Neutrino-Electron Scattering*, *Phys. Rev. Lett.* **82** (1999) 2430.

[24] J. N. Bahcall, *Solar neutrinos: An overview*, *Curr. Sci.* **77** (1999) 11, 1487-1495.

[25] Kamiokande collaboration, *Atmospheric Neutrino Background and Pion Nuclear Effect for Kamioka Nucleon Decay Experiment*, *J. Phys. Soc. Jap.* **55** (1986) 3786.

[26] T. Kajita, *Experimental study of the atmospheric neutrino flux*, *Phys. Lett.* **B205** (1988), 416-420.

[27] Soudan 2 collaboration, *Atmospheric neutrino results from Soudan 2*, *Prog. Part. Nucl.* **40** (1998), 205-217.

[28] T. Kajita, *Atmospheric neutrinos*, *New J. Phys.* **6** (2004) 194.

[29] Super-K collaboration, *Evidence for Oscillation of Atmospheric Neutrinos*, *Phys. Rev. Lett.* **81** (1998) 1562.

[30] SNO collaboration, *First neutrino observations from the Sudbury Neutrino Observatory*, *Nucl. Phys. B. (Proc. Suppl.)* **91** (2001), 21-28.

[31] SNO collaboration, *Measurement of the rate of* $\nu_e + d \to p + p + e^-$ *interactions produced by* ^8B *solar neutrinos at the Sudbury Neutrino Observatory*, *Phys. Rev. Lett.* **87** (2001) 071301.

[32] SNO collaboration, *The Sudbury Neutrino Observatory*, *Nucl. Phys.* **B908** (2016), 30-51.

[33] B. Pontecorvo, *Neutrino Experiments and the Problem of Conservation of Leptonic Charge*, *Sov. phys. JETP.* **26** (1968) 5.

[34] Z. Maki, M. Nakagawa and S. Sakata, *Remarks on the Unified Model of Elementary Particles*, *Prog. Theor. Phys.* **28** (1962), 870-880.

[35] L. Wolfenstein, *Parametrization of the Kobayashi-Maskawa Matrix*, *Phys. Rev. Lett.* **51** (1983) 1945.

[36] S. P. Rosen and J. M. Gelb, *Mikheyev-Smirnov-Wolfenstein enhancement of oscillations as a possible solution to the solar-neutrino problem*, *Phys. Rev.* **D34** (1986) 969.

[37] KamLAND collaboration, *First Results from KamLAND: Evidence for Reactor Antineutrino Disappearance*, *Phys. Rev. Lett.* **90** (2003) 021802.

[38] KamLAND collaboration, *Precision Measurement of Neutrino Oscillation Parameters with KamLAND*, *Phys. Rev. Lett.* **100** (2008) 221803.

[39] KamLAND collaboration, *Constraints on* θ_{13} *from a three-flavor oscillation analysis of reactor antineutrinos at KamLAND*, *Phys. Rev.* **D83** (2011) 052002.

[40] MINOS collaboration, *Observation of Muon Neutrino Disappearance with the MINOS Detectors in the NuMI Neutrino Beam*, *Phys. Rev. Lett.* **97** (2006) 191801.

[41] Chooz collaboration, *Limits on neutrino oscillations from the CHOOZ experiment*, *Phys. Lett.* **B466** (1999), 415-430.

[42] Chooz collaboration, *Search for neutrino oscillations on a long base-line at the CHOOZ nuclear power station*, *Eur. Phys. J.* **C27** (2003), 331-374.

[43] T2K collaboration, *The T2K experiment*, *Nucl. Instrum. Methods Phys. Res.* **A659** (2011), 106-135.

[44] T2K collaboration, *Measurements of neutrino oscillation parameters from the T2K experiment using* 3.6×10^{21} *protons on target*, *Eur. Phys. J.* **C83** (2023) 782.

[45] T2K collaboration, *Improved constraints on neutrino mixing from the T2K experiment with* 3.13×10^{21} *protons on target*, *Phys. Rev.* **D103** (2021) 112008.

[46] T2K collaboration, *Constraint on the matter–antimatter symmetry-violating phase in neutrino oscillations*, *Nature* **580** (2020), 339–344.

[47] NOvA collaboration, *First measurement of muon-neutrino disappearance in NOvA*, *Phys. Rev.* **D93**, (2016) 051104.

[48] I. Martinez-Soler, *Global Neutrino Data Analyses*, *Proc. Phys.* **292** (2023), 43-49.

[49] Hyper-K collaboration, *Hyper Kamiokande Design Report*, arXiv:1805.04163v2 [physics.ins-det] (2018).

[50] DUNE collaboration, *Long-Baseline Neutrino Facility (LBNF) and Deep Underground Neutrino Experiment (DUNE) Conceptual Design Report Volume 1: The LBNF and DUNE Projects*, arXiv:1601.05471 [physics.ins-det] (2016).

[51] JUNO collaboration, *JUNO Conceptual Design Report*, arXiv:1508.07166 [physics.ins-det] (2015).

[52] KamLAND-Zen collaboration, *Search for the Majorana Nature of Neutrinos in the Inverted Mass Ordering Region with KamLAND-Zen*, *Phys. Rev. Lett.* **130** (2023) 051801.

[53] J. Schechter and J. W. F. Valle, *Neutrino masses in $SU(2) \otimes SU(1)$ theories*, *Phys. Rev.* **D22** (1980) 2227.

[54] Hyper-Kamiokande collaboration, *Supernova Model Discrimination with Hyper-Kamiokande*, *Ap. J.* **916** (2021) 15.

[55] PDG, *Review of Particle Physics: Dark Matter*, *Chin. Phys.* **C38** (2014) 09001.

[56] LSND collaboration, *Evidence for neutrino oscillations from the observation of $\bar{\nu}_e$ appearance in a $\bar{\nu}_\mu$ beam*, *Phys. Rev.* **D64** (2001) 112007.

[57] MiniBooNE collaboration, *Significant Excess of Electronlike Events in the MiniBooNE Short-Baseline Neutrino Experiment*, *Phys. Rev. Lett.* **121** (2018) 221801.

[58] C. Burgard, *Example: Standard model of physics*, available online at: `https://texample.net/tikz/examples/model-physics/`.

[59] Y. Hayato, *A neutrino interaction simulation program library NEUT*, *Acta Phys. Polon.* **B40** (2009) 2477.

[60] Y. Hayato and L. Pickering, *The NEUT neutrino interaction simulation program library*, *EPJ ST* **230** (2021), 4469–4481.

[61] C. Andreopoulos, C. Barry, S, Dytman, H. Gallagher, T. Golan, R. Hatcher, G. Perdue and J. Yarba, *GENIE Neutrino Monte Carlo Generator: Physics and User Manual*, arXiv:1510.05494 [hep-ph] (2015).

[62] M. Sajjad Athar and S. K. Singh, *The Physics of Neutrino Interactions*, *Cambridge University Press*, Cambridge, England (2020).

[63] J. A. Formaggio and G. P. Zeller, *From eV to EeV: Neutrino cross sections across energy scales*, *Rev. Mod. Phys.* **84** (2012) 1307.

[64] O. Benhar, N. Farina, H. Nakamura, M. Sakuda, and R. Seki, *Electron- and neutrino-nucleus scattering in the impulse approximation regime*, *Phys. Rev.* **D72** (2005) 053005.

[65] R.A. Smith and E.J. Moniz, *Neutrino reactions on nuclear targets*, *Nucl. Phys.* **B43** (1972), 605-622.

[66] L. Alvarez-Ruso, Y. Hayato and J. Nieves, *Progress and open questions in the physics of neutrino cross sections at intermediate energies*, *New J. Phys.* **16** (2014) 075015.

[67] O. Benhar and A. Fabrocini, *Two-nucleon spectral function in infinite nuclear matter*, *Phys. Rev.* **C62** (2000) 034304.

[68] O. Benhar and D. Meloni, *Total neutrino and antineutrino nuclear cross sections around 1 GeV*, *Nucl. Phys.* **A789** (2007), 379-402.

[69] T. Golan, C. Juszczak, and J. T. Sobczyk, *Effects of final-state interactions in neutrino-nucleus interactions*, *Phys. Rev.* **C86** (2012), 015505.

[70] J. Isaacson, W. I. Jay, A. Lovato, P. A. N. Machado, and N. Rocco, *New approach to intranuclear cascades with quantum Monte Carlo configurations*, *Phys. Rev.* **C103** (2021), 015502.

[71] L.L. Salcedo, E. Oset, M.J. Vicente-Vacas and C. Garcia-Recio, *Computer simulation of inclusive pion nuclear reactions*, *Nucl. Phys.* **A484** (1988) 3-4, 557-592.

[72] R. D. Woods and D. S. Saxon, *Diffuse Surface Optical Model for Nucleon-Nuclei Scattering*, *Phys. Rev.* **95** (1954), 557.

[73] C.H. Llewellyn Smith, *Neutrino reactions at accelerator energies*, *Phys. Rep.* **3** (1972) 5, 261-379.

[74] B. Bhattacharya, R. J. Hill, and G. Paz, *Model-independent determination of the axial mass parameter in quasielastic neutrino-nucleon scattering*, *Phys. Rev.* **D84** (2011) 073006.

[75] D. Rein and L. M. Sehgal, *Neutrino-excitation of baryon resonances and single pion production*, *Ann. Phys.* **133** (1981) 1, 79-153.

[76] P. Martins, *Berger-Sehgal coherent pion production model implementation in NEUT*, *T2K-TN-262 [T2K internal document]* (2017).

[77] S. Dolan, U. Mosel, K. Gallmeister, L. Pickering and S. Bolognesi, *Sensitivity of neutrino-nucleus interaction measurements to 2p2h excitations*, *Phys. Rev.* **C98** (2018) 045502.

[78] MINERvA collaboration, *Design, calibration, and performance of the MINERvA detector*, *Nucl. Instrum. Methods Phys. Res.* **A743** (2014), 130-159.

[79] PDG, *Review of Particle Physics: Neutrino Cross Sections*, *Chin. Phys.* **C38** (2014) 09001.

[80] T2K collaboration, *Simultaneous measurement of the muon neutrino charged-current cross section on oxygen and carbon without pions in the final state at T2K*, *Phys. Rev.* **D101** (2020) 112004.

[81] T2K collaboration, *Measurements of $\bar{\nu}_\mu$ and $\bar{\nu}_\mu$ + ν_μ charged-current cross-sections without detected pions or protons on water and hydrocarbon at a mean anti-neutrino energy of 0.86 GeV*, *Prog. Theor. Exp. Phys.* **2021** (2021) 4.

[82] T2K collaboration, *First measurement of the muon neutrino charged current single pion production cross section on water with the T2K near detector*, *Phys. Rev.* **D95** (2017) 012010.

[83] MINERvA collaboration, *Simultaneous Measurement of ν_μ Quasielasticlike Cross Sections on CH, C, H_2O, Fe, and Pb as a Function of Muon Kinematics at MINERvA*, *Phys. Rev. Lett.* **130** (2023) 161801.

[84] MicroBooNE collaboration, *First Measurement of Energy-Dependent Inclusive Muon Neutrino Charged-Current Cross Sections on Argon with the MicroBooNE Detector*, *Phys. Rev. Lett.* **128** (2022) 151801.

[85] T2K collaboration, *Measurement of the charged-current electron (anti-)neutrino inclusive cross-sections at the T2K off-axis near detector ND280*, *JHEP* **10** (2020) 114.

[86] T2K collaboration, *Measurement of the Inclusive Electron Neutrino Charged Current Cross Section on Carbon with the T2K Near Detector*, *Phys. Rev. Lett.* **113** (2014) 241803.

[87] T. Golan, J. Sobczyk, and J. Zmuda, *NuWro: the Wrocław Monte Carlo Generator of Neutrino Interactions*, *Nucl. Phys. B, Proc. Suppl.* **229–232** (2012), 499.

[88] T2K collaboration, *First T2K measurement of transverse kinematic imbalance in the muon-neutrino charged-current single-π^+ production channel containing at least one proton*, *Phys. Rev.* **D103** (2021) 112009.

[89] T2K collaboration, *First measurement of muon neutrino charged-current interactions on hydrocarbon without pions in the final state using multiple detectors with correlated energy spectra at T2K*, *Phys. Rev.* **D108** (2023) 112009.

[90] T2K Collaboration, *Measurements of the ν_μ and $\bar{\nu}_\mu$-induced Coherent Charged Pion Production Cross Sections on ^{12}C by the T2K experiment*, *Phys. Rev.* **D108** (2023) 092009.

[91] C. Jesus-Valls, *First Cross Section Measurement of the Neutrino Single Positive Pion Production at the T2K experiment*, *T2K-TN-412 [T2K internal document]* (2024).

[92] K. Yasutome, *The meaurement of neutrino cross section on H_2O and CH targets at 1 GeV region by T2K-WAGASCI detectors*, *T2K-TN-455 [T2K internal document]* (2024).

[93] T2K collaboration, *T2K Experiment Public Website*, accessible online at `https://t2k-experiment.org/t2k/`.

[94] T2K collaboration, *Design concept of the magnetic horn system for the T2K neutrino beam*, *Nucl. Instrum. Meth.* **A690** (2012), 27-33.

[95] T2K collaboration, *Development and operational experience of magnetic horn system for T2K experiment*, *Nucl. Instrum. Meth.* **A789** (2015), 57-80.

[96] T2K collaboration, *The T2K ND280 off-axis pi–zero detector*, *Nucl. Instrum. Meth.* **A686** (2012), 48-63.

[97] T2K collaboration, *The T2K fine-grained detectors*, *Nucl. Instrum. Meth.* **A696** (2012), 1-31.

[98] T2K collaboration, *Time projection chambers for the T2K near detectors*, *Nucl. Instrum. Meth.* **A637** (2011), 25-46.

[99] T2K collaboration, *The electromagnetic calorimeter for the T2K near detector ND280*, *JINST* **8** (2013) 10019.

[100] T2K collaboration, *Measurements of the T2K neutrino beam properties using the INGRID on-axis near detector*, *Nucl. Instrum. Meth.* **A694** (2012), 211-223.

[101] T2K collaboration, *T2K ND280 Upgrade – Technical Design Report*, arXiv:1901.03750 [physics.ins-det].

[102] Y. Itow *et al.*, *The JHF-Kamioka neutrino project*, arXiv:0106019 [hep-ex].

[103] D. Barrow, L. Berns, C. Bronner, M. Friend, C. Wret and J. Xia, *Flux and interaction models for the initial T2K-SK atmospheric joint fit studies*, *T2K-TN-422 [T2K internal document]* (2022).

[104] S. Jenkins, *Measurement of the muon neutrino charged current single positive pion production cross section on water in the ND280 near detector*, University of Sheffield (2020), available online at: `https://etheses.whiterose.ac.uk/30518/`.

[105] T2K collaboration, *Measurement of the intrinsic electron neutrino component in the T2K neutrino beam with the ND280 detector*, *Phys. Rev.* **D89** (2014) 099902.

[106] J. Kim, C. Nielsen and M. Wilking, *Michel Electron Tagging in the FGDs*, *T2K TN-104 [T2K internal document]* (2015).

[107] C. Bojechko, A. Cervera, L. Escudero, A. Gaudin, M. Ieva, D. Karlen, F. Sanchez and P. Stamoulis, *Measurement and Correction of Magnetic Field Distortions in the Time Projection Chambers*, *T2K TN-104 [T2K internal document]* (2013).

[108] A. Cervera and L. Escudero, *Study of momentum resolution and scale using tracks that cross multiple TPCs*, *T2K TN-222 [T2K internal document]* (2014).

[109] S. Bordoni, C. Giganti, A. Hillairet and F. Sanchez, *TPC-PID status and performances with Production 6*, *T2K TN-221 [T2K internal document]* (2015).

[110] D. Brailsford, A. Chappell, P. Denner, D. R. Hadley, P. Martins, G. Christodoulou, S. King and I. Lamont, *Study of the Tracker ECal systematics*, *T2K TN-279 [T2K internal document]* (2017).

[111] A. Fiorentini, *ND280 TPC cluster efficiency*, *T2K TN-234 [T2K internal document]* (2015).

[112] Y. Petrov and A. Hillairet, *ND280 TPC track-finding efficiency*, *T2K TN-163 [T2K internal document]* (2016).

[113] F. Sanchez and J. Medina, *ND280 global charge identification systematic error*, *T2K TN-229 [T2K internal document]* (2016).

[114] A. Hillairet, L. Haegel, T. Lindner, J. Myslik and P. Stamoulis, *ND280 tracker tracking efficiency in the 2011 analysis*, *T2K TN-075 [T2K internal document]* (2015).

[115] F. Dufour, L. Haegel, T. Lindner and S. Oser, *Systematics on Out-of-FGD-Fiducial Volume Backgrounds in the ND280 Tracker Muon Neutrino Analysis*, *T2K TN-098 [T2K internal document]* (2015).

[116] S. Agostinelli *et al.*, *Geant4—a simulation toolkit,* Nucl. Instrum. Methods Phys. Res. ***506*** *(2003) 3, 250-303*.

[117] K. Kowalik and J. Lagoda, *The simulations of the beam neutrinos interactions outside the ND280 detector*, *T2K TN-077 [T2K internal document]* (2012).

[118] R. Brun and F. Rademakers, *ROOT Data Analysis Framework* (2019), accessible online at: `https://root.cern.ch/`.

[119] T. Honjoa, *21bv2 flux release with SK up to run 11, ND up to run 9*, *T2K 21b flux release [T2K internal document]* (2022).

[120] J. Nieves, I. Ruiz Simo, and M. J. Vicente Vacas, *Inclusive charged-current neutrino-nucleus reactions*, *Phys. Rev.* **C83** (2011) 045501.

[121] T. Sjöstrand, *High-energy-physics event generation with PYTHIA 5.7 and JETSET 7.4*, *Comput. Phys. Commun.* **82** (1994) 1, 74-89.

[122] H.W. Bertini, *Intranuclear-Cascade Calculation of the Secondary Nucleon Spectra from Nucleon-Nucleus Interactions in the Energy Range 340 to 2900 MeV and Comparisons with Experiment*, *Phys. Rev.* **188** (1969) 1711.

[123] A. Cudd, *Measurement of the Charged Current Muon Neutrino Differential Cross Section on Scintillator with Zero Pions in the Final State with the T2K On/Off-axis Near Detectors*, Michigan State University (2020), available online at: `https://d.lib.msu.edu/etd/48404`.

[124] R. Barlow and C. Beeston, *Fitting using finite monte carlo samples*, *Computer Physics Communications*, **77** (1993) 2, 219-228.

[125] A. Cudd, *Super-xsllhFitter* (2019), accessible online at: `https://gitlab.com/cuddandr/xsLLhFitter/`.

[126] F. James and M. Winkler, *Minuit 2* (2018), accessible online at: `https://root.cern.ch/root/htmldoc/guides/minuit2/Minuit2.html`.

[127] MINOS Collaboration, *Study of quasielastic scattering using charged-current ν_μ-iron interactions in the MINOS near detector*, *Phys. Rev.* **D91** (2015) 012005.

[128] MINERvA Collaboration, *Cross sections for ν_μ and $\bar{\nu}_\mu$ induced pion production on hydrocarbon in the few-GeV region using MINERvA*, *Phys. Rev.* **D94** (2016) 052005.

[129] M. Martini, M. Ericson, G. Chanfray and J. Marteau, *A Unified approach for nucleon knock-out, coherent and incoherent pion production in neutrino interactions with nuclei*, *Phys. Rev.* **C80**, (2009) 065501.

[130] S. Boyd, S. Jenkins, K. Jewkes, K. Lachner, N. Latham, A. Mitra and M. Spangenberg, *Hyper-Kamiokande Light Injector Collimator Technical Note*, *[Hyper-K internal document]* (2023).

[131] J. Canny, *A Computational Approach to Edge Detection*, *IEEE Trans. Pattern Anal. Mach. Intell.* **8** (1986), 679–698.